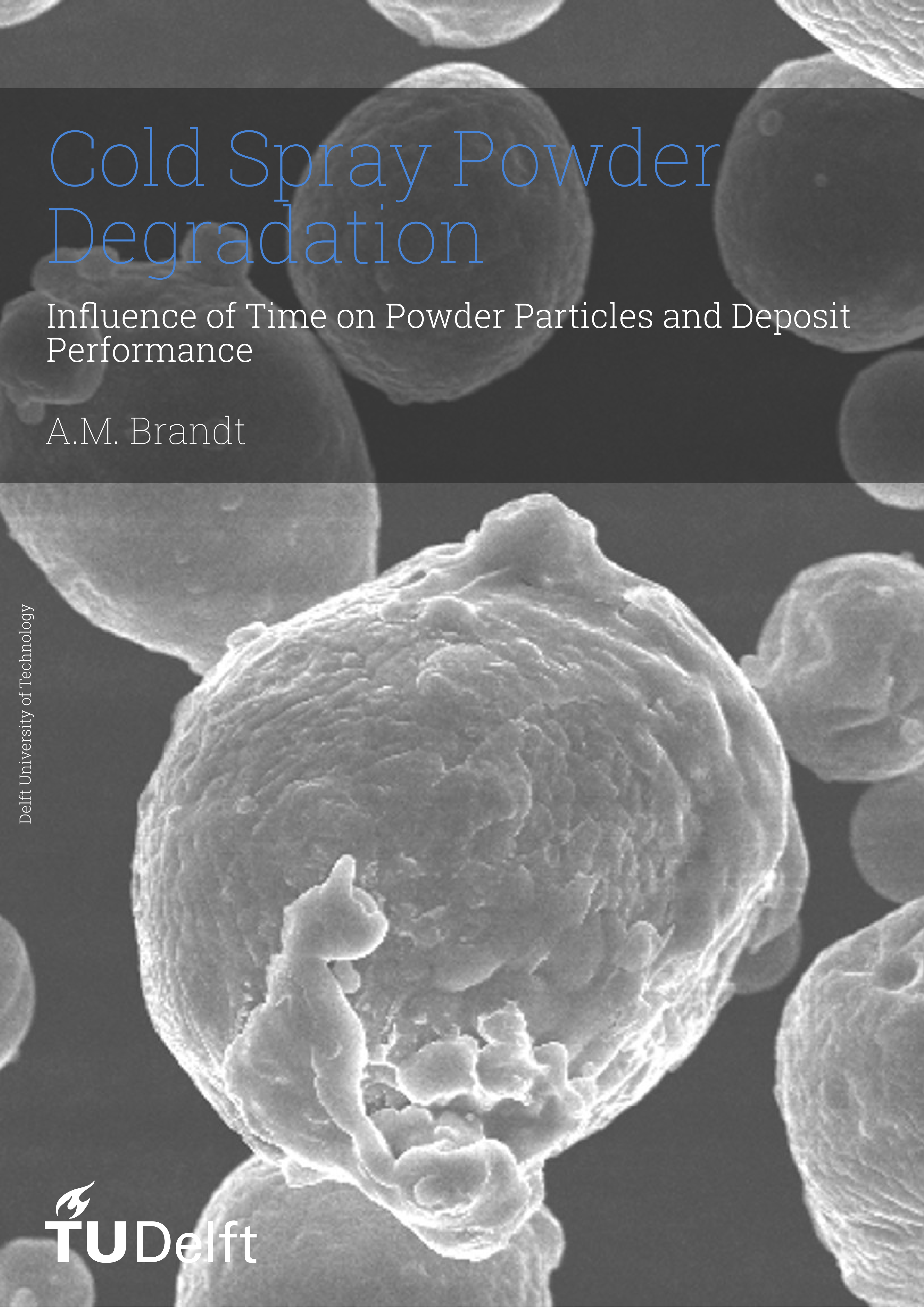

Cold Spray Powder Degradation

Influence of Time on Powder Particles and Deposit Performance

A.M. Brandt

Delft University of Technology

TU Delft

Cold Spray Powder Degradation

Influence of Time on Powder Particles and Deposit Performance

by

A.M. Brandt

To be defended publicly on Wednesday 28 January 2026 at 14:00

Responsible Supervisor:	Dr. Ir. John-Alan Pascoe
Supervisor:	Ir. Mary Patrick
Examination Committee Chairperson:	Dr. Santiago Garcia
Examination Committee Independent Examiner:	Dr. Yinglu Tang
Project Duration:	April, 2025 - January, 2026
Faculty:	Faculty of Aerospace Engineering, Delft

Cover: SEM image of Al2024 particles (by author)

TUDelft

Acknowledgments

I would like to thank my supervisors Dr. Ir. John-Alan Pascoe and Ir. Mary Patrick for their support and thoughtful contributions of feedback throughout the thesis process. I would like to thank Ir. Stratos Koufis for his advice in the beginning stages of specimen design, even though ultimately I could not continue with that testing. I would like to thank Dr. Patrizio Lomonaco for his advice on the topic and assistance in facilitating the LASHPOL testing. I would like to thank Dr. Francesco Delloro, for arranging the time and equipment for the LASHPOL testing, assisting me with the design of these tests, and operating the setup, as well as his PhD candidate Inass for her contributions in preparing and executing the tests.

This work received support from the Dutch Research Council (NWO) Open Technology Programme 'CSAR' (grant no: 20434).

Alison Brandt
Delft, January 2026

Abstract

Cold spray is a material deposition process where a high-pressure gas stream accelerates small particles through a supersonic nozzle and deposits them in a coating on the substrate material. The powder is typically shipped and stored before use, so degradation could occur. This research investigates the influence of time-dependent degradation of cold spray powder materials and how this affects the sprayed coatings. Conditions of four different samples of AA6061 and AA2024 powders were evaluated with Raman spectroscopy, X-Ray diffraction, and SEM-EDS over several time intervals to monitor the development of oxides and alterations in powder surfaces. Single particle launches using a laser system were performed at Mines Paris-PSL to observe the particle-scale behavior during replicated spraying experiments. A spraying test comparing three batches of AA6061 powders using two different nozzle traverse speeds provided more information for the coating behavior of the powders.

The powder condition was shown to be altering with time, though the underlying causes other than oxidation and possible phase transformation could not be identified. There were few particles adhering during the single particle experiments, and some rebounding particles left behind pieces of oxides on the substrates. The powder degradation is expected to result in higher compressive stress in the coating caused by shot-peening effect from successive rebounds and a chance of higher oxide content.

Contents

List of Figures

List of Tables

Nomenclature

Abbreviations

Abbreviation	Definition
COMPO	Compositional view using backscatter electrons in SEM
EDS	Energy Discpersive X-Ray Spectroscopy
GCR	Galactic Cosmic Rays
LASHPOL	LAser Shock POwder Launcher
LEI	Low-energy Electron Imaging for SEM
LM	Low Magnification mode for SEM
PI	Polyimide
PSD	Particle Size Distribution
RBEI	Retractable Backscatter Electron Imaging detector for SEM
RH	Relative Humidity
SEI	Secondary Electron Imaging for SEM
SEM	Scanning Electron Microscope
TEM	Transmission Electron Microscope
XRD	X-Ray Diffraction

1

Introduction

Cold spray is a material deposition method related to additive manufacturing and thermal spray applications. Using a high pressure and high temperature gas stream and a converging-diverging nozzle, powder particles are accelerated to supersonic speeds to provide sufficient energy to adhere to a surface. It is an emergent topic in repair and maintenance circles for the ability to add material to non-weldable alloys because melting of the entire product does not occur during the process. The quality of any coating can be influenced by a number of factors including the gas type, pressure, and temperature during spraying, as well as the chosen powder and substrate combination. Generally, powder alloys and particle sizes are chosen by the manufacturers to allow flexibility between different systems and application methods.

For the aerospace industry in particular, high performance aluminum alloys are popular materials for structural parts, and the cold spray process is being investigated for repairing these parts. For this work, the scope was narrowed to focus on aluminum alloys. To produce high-quality parts and repairs, both the powder material and the substrate must be controlled. While there has been extensive research done on bulk metal treatment and degradation, the effect on cold spray powders and resulting influence on a deposited coating has not been extensively studied.

Most powders for cold spray are produced using gas atomization, though the ability of this process to be tuned allows different manufacturers to have varying powder specifications. Variability in the properties between batches should be controlled by the manufacturer tuning the process, but factors such as oxidation and storage conditions can affect the powder after being received by the user. In a material-reliant process like cold spray, these variations could have negative effects on the final product. Understanding the time-dependent variation in powder condition and how exactly the process is affected is relevant to the continued evolution of cold spray as an industry. The effect that the variation or degradation has on the powder and on any coatings produced was investigated in this thesis.

In the following sections, a review of the current literature in the fields of cold spray, powder production, powder condition, and particle testing is presented in Chapter 2. The research questions that were identified to fill the research gap are also presented in Section 2.6. The methodology followed and the materials and test methods used are presented in Chapter 3. The results of the testing and some analysis of the collected data are presented in Chapter 4. A discussion encompassing all the results and their impact on cold spray is included in Chapter 5. The conclusions of the report and answers to the research questions are presented in Chapter 6. Finally, some recommendations for future work by researchers, industry, and powder suppliers are presented in Chapter 7.

Some extra information is included in the Appendices, including a section removed from the literature review and extra figures and explanations not necessary in the body of the report.

2

Literature Review

Cold spray is a powder deposition technology that allows for repair of existing metallic structures and surfaces. This process uses accelerated micro-particles of material that impact a surface and gradually build up material [1]. A schematic of the process is shown in Figure 2.1 below.

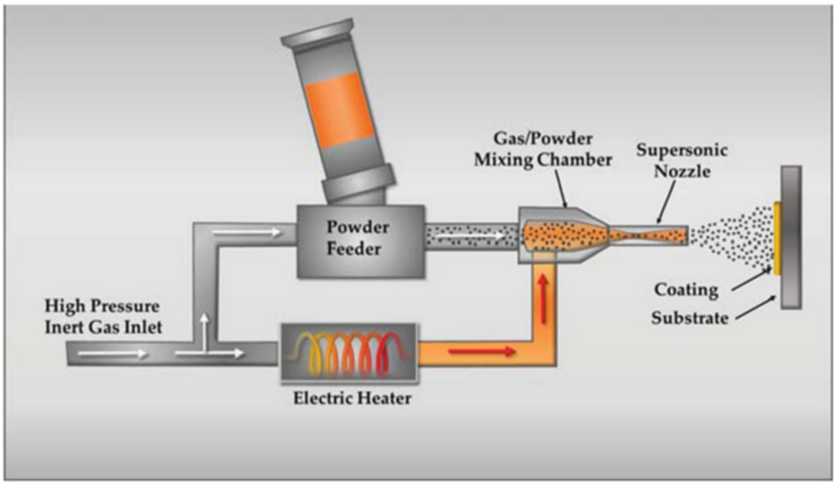

Figure 2.1: Schematic of the cold spray process, from Champagne et al. 'Practical Cold Spray' [1]

For aluminum cold spray, the powder typically has a size range of 20 to 50 μm and is accelerated in a converging-diverging De Laval type nozzle to speeds of 300-1000 m/s. The carrier and process gas is typically nitrogen or helium [1–3]. There are several factors that influence the behavior of the resulting coating and its overall quality. These include the cold spray machine settings for temperature of the heating coil for the carrier gas and the pressure of the carrier gas. Also the parameters controlling the nozzle travel (speed, distance offset, path) for the deposition along the specimen can have an effect. Plus, there is potential for clogging or fouling of the nozzle affecting the deposition. Outside of the machinery considerations, many other aspects influence the final result. These include but are not limited to: the gas used, the powder size distribution, the powder shape, oxides on the powder surface, morphology and microstructure of the powder particles, roughness of the substrate, hardness or material differences between powder and substrate, and any heat treatment of the powder or of the final product.

The main goal of the thesis is to investigate if and why the quality of a deposit decreases over time after a powder package was opened. The literature presented here supports the research process. How powders are produced is outlined in Section 2.1, then the different characterization methods in literature are presented in Section 2.2. The particle impact behavior during cold spray and the process parameters that influence the critical velocity for adhesion, along with the effect of oxides are presented in Sections 2.3, 2.3.1 and 2.3.2. The different expectations for the composition of these oxides are discussed in Section 2.4. Lastly, the influence of storage conditions of powder containers on the powder itself is highlighted in Section 2.5. This leads to the main research questions in Section 2.6 which were the focus for this work.

2.1. Cold spray powder production

Powders for cold spray, or any powder-based manufacturing process, can be made in a variety of ways, depending on the necessary particle sizes, shapes, volume of the produced batch, and material-specific behaviors [4]. Some examples for these production methods include water atomization, gas atomization, and mechanical grinding of feedstock material. For producing aluminum cold spray powders, generally the process of gas atomization is used. This is a tuneable process and can relatively quickly form high quality powders of the requisite size [4, 5]. Gas atomization involves melted feedstock falling out of a small nozzle and being impinged with high pressure gas streams to break up the molten metal into small particles [6]. An example is shown in Figure 2.2. The size of the particles produced depends on the amount of gas used versus the amount of metal, and the sizes can vary from around 10 to 300 μm [4].

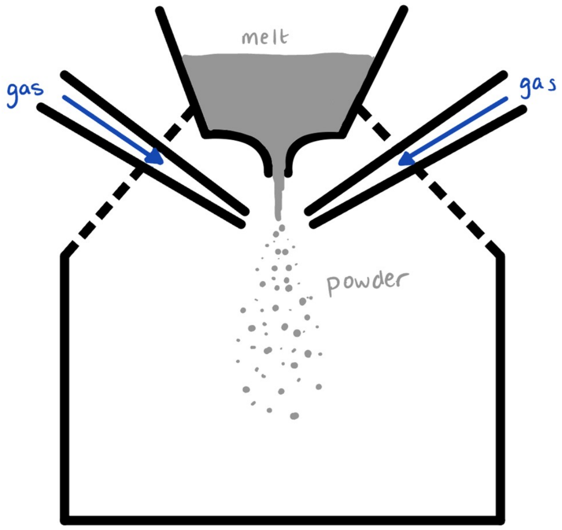

Figure 2.2: Schematic illustration of gas atomization process for metal powder production

Because the molten metal is rapidly cooled by the high pressure gas streams, the powder particles are formed quickly, which contributes to both their shape and microstructure. Rapid cooling contributes a finer microstructure, which is on a more consistent scale for micro-particles than bulk casted alloys. This can give a different behavior for individual particles compared to their base alloy, despite no alterations in alloy composition[4, 5, 7]. This can also influence the powder shape. The time it takes for the molten particle to solidify could be shorter than the time for surface tension to dominate, yielding irregularly shaped particles that did not have time to become spheres before fully solidifying. Generally for gas-atomized aluminum powders, this is less of a concern. Powders formed with the similar process of water atomization can be affected due to the differences in the cooling rates [4].

As mentioned previously, the rapid cooling of the powder particles influences their underlying microstructure, where grains, grain boundaries, and dendritic structures can be found along with precipitates, depending on the alloy [4] [8]. The microstructures formed during atomization of powder particles have been investigated using Scanning Electron Microscopy (SEM), Transmission Electron Microscopy (TEM) and Energy Dispersive X-Ray Spectroscopy (EDX/EDS) [5, 8, 9].

Related to both the shape and size of the produced powders, there is a tendency for particles to impact each other within the atomization chamber during production. This is due to the continued gas flow, the shape of the collection area, and the light weight of the smallest particles potentially returning to the path of the atomization stream despite being atomized already [4, 6]. These impacts can result in agglomeration of previously smaller particles into larger, more irregularly shaped particles, and more specifically in the production of so-called ”satellites” [4, 10]. These are larger particles with a very small ”fine” particle stuck to their surface much like a satellite that orbits a planetary body. Even with a spherical larger particle and spherical satellite, the resulting particle formed could behave differently in flight during spraying due to the presence of the satellite.

While oxidation is generally a faster process at elevated temperatures due to higher diffusion rates of oxygen into the bulk material [11], oxidation of the powder particles is possible even during the atomization process for alloys with reactive elements [4]. The formation, chemistry, and behavior of the oxides will be described further in later sections, but they can have an influence from as early as the powder production stage. Aluminum is a material that spontaneously forms oxides, and refractory oxides can form during the atomization process that may prevent the particle from attaining a spherical shape [4].

Some powders, but not those considered in this thesis, are not alloyed via their feedstock but rather once atomized. This is typically done with mechanical mixing to disperse alloy elements (mostly) homogeneously throughout the final powder mixture. There are difficulties with achieving this which are generally overcome by extending mixing times or using more energetic means, which come with their own drawbacks. These include agglomeration of finer powders or contamination depending on the method [6]. A similarity can be drawn to powder mixing for re-use from thermal additive manufacturing processes like powder bed fusion. In these processes, the powder surrounding but not contributing to the final part can become partially melted and form larger particles that are unable to be immediately re-used. These can be directly recycled to break larger particles down into appropriate sizes again, though without a high temperature melting stage oxides will remain after mechanical recycling [12]. With this in mind, it is unlikely that any mechanical mixing or alloying after atomization is capable of breaking up the oxides that can form during atomization, and that powders have a certain inherent oxide content as delivered by the manufacturer. While not immediately relevant to the research in this thesis, this informs on the possibility for recycling powders in cold spray, and the likelihood of further processing being required before powders are re-usable.

The packaging and storage of the manufactured powders varies depending on the manufacturer and any treatments or stabilizers used. Several options are outlined in powder standards created by the United States Department of Defense. The manufacturing process standard document for ”Materials Deposition, Cold Spray” (MIL-STD-3021) and the detail specification for ”Powders for Cold Spray Deposition” (MIL-DTL-32495) have certain recommendations to maintain environmental stability during storage [13] [14]. The differences between the outlined options has not been studied extensively, and is a possible research gap for future investigation. This will be expanded upon in a section below.

2.2. Powder characterization

Since cold spray is a relatively new technology, there are a variety of methods and techniques being investigated and used to determine what makes a good powder, machine, and final product. Some have carried over from other powder based methods with greater maturity, particularly thermal or plasma spray technologies, though no standards have been normalized or harmonized in the industry. Additionally, each powder manufacturer may use a different production method and and limits for quality control. This introduces further potential variability in the quality of a sprayed powder as a direct result of its production. Using characterization techniques to determine the size, shape, flowability, alloy, hardness, and oxidation state of the powders can inform the user of these differences.

In terms of powder quality, aside from ensuring the correct alloy is used, the size distribution of the particles, along with their shape and surface condition are the most important variables to keep track of. These aspects have the most immediate effect on the process and the spraying parameters needed to produce a high-quality coating because they influence the critical velocity: the particle speed required to adhere to the substrate (this concept is expanded upon in further sections). Precipitate strengthened alloys like AA6061 can also be heat treated to alter the powder or resulting part behavior, based on the growth and ageing of precipitates within the main phase [5, 15]. There are also bulk behaviors of powders that can be measured that have an influence on the quality of the resulting product. These include things like flowability and spreadability, and are related to the particle specific conditions of the powder [6].

Starting with the powder size, there are several ways to measure the distribution. These mainly include sorting the powder particles into different size brackets, but the means through which sorting is achieved differs. Physical sieving of powders through successively smaller meshes can separate a powder batch into sections which collectively make up the size distribution. Powder that is too large to fall through the gaps in the mesh remains on each layer of the sieve until only the finest particles fall through the densest mesh and are collected [1, 6]. The number or volume of particles on each section can be compared to the total powder amount and indicate the particle size distribution (PSD) for the batch.

This process is shown schematically with two sieve stages in Figure 2.3. This is a simplification of the process, as more stages are typically used to categorize the sizes of the powder particles with smaller differences between the stages to give precise information.

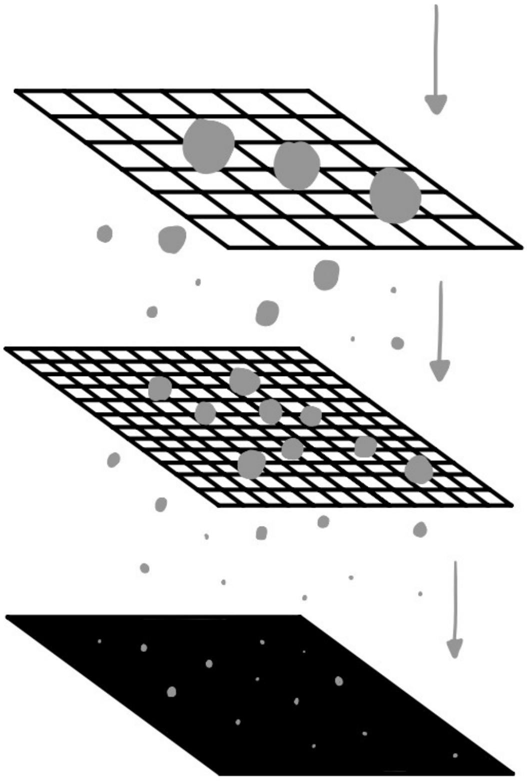

Figure 2.3: Two stage sieving of powder and collection of fines

The powder that remains in each section of the sieve tower is thus smaller than the previous mesh and larger than the next mesh. A popular sorting mesh size for cold spray powders is the -325 mesh, through which particles of less than 44 μm diameter will fall [1]. Using this mesh size for the first stage prevents larger particles from being included. While overly large particles should not be included in a powder batch, the same holds for very small particles. Very small particles, ”fines”, of around 5 μm diameter or less, can have a detrimental effect on spraying as they tend to stick to any imperfections in the nozzle or powder feeder [16]. If the powder shifts during storage or handling and these fines are present, they may encourage agglomeration of the powder into larger masses and restrict the flowability [6].

While sieving is effective, it does not allow for in-situ measurement of the sprayed powder as it is measured at a single point in time for a very specific portion of the powder batch. Also, the full range of particle sizes measured are limited to the sieve mesh densities and number of stages. Thus, measuring the PSD during spraying or with a larger number of stages is valuable information for tracking the behavior of the resulting deposit back to the powder size. This is frequently optically assessed, with a camera or laser tracking and imaging the particles as they are carried through the gas stream [17] [3].

For more detailed measurements without using a cold spray machine and camera setup, there are standalone machines called particle size analyzers. These machines are designed to categorize a powder sample size distribution, and typically use laser diffraction as the means of measurement [6, 18]. Measurements can be made with dry powder or with a certain amount of water mixed in. Just as with sieving, this cannot be done in-situ, and care must be taken when sampling the powder to ensure it is representative of the total batch [19]. The results of the analysis indicate the volume percent of each particle size range, over the total size range the machine is capable of measuring. This method does assume that the particles are perfect spheres, so for more irregularly shaped particles there can be a higher uncertainty and the distribution may need to be confirmed.

The PSD that results from any measurement is a volume percentage of the different particle sizes that the tested batch contains. These distributions are noted with a D10, D50 and D90 value, which indicate the diameters that 10%, 50%, and 90% of the particles fall below, respectively. The D50 is the mean diameter of a sampled powder [1, 18].

Powder size and shape can also be identified or confirmed with examination in SEM or optical microscope, but the amount of powder analyzed is small. The amount of powder is restricted to what sticks on a carbon tape on the specimen stage of the SEM, and size measurements of particles rely on the operator and chosen calculation method [6]. This is considered to be less time consuming than sieving for determining particle sizes, and with very low error compared to laser diffraction methods.

Flowability describes the ease with which the powder moves over itself and flows as a material, where particle shapes and sizes have primary influence [6]. Flowability can be assessed in several different ways. Some, like the Hall flow meter, use the time it takes for powder to flow through a specifically shaped channel as a measure of the capability of the powder to flow [6, 20]. This is a widely used process because of its simplicity, but can be influenced by things like aeration of the powders and so is regarded more as a qualitative test for comparison rather than quantitative. Another method to determine the flowability of a powder is a powder rheometer, which can measure the energy required to move the powder in a contained volume [20]. This more controlled test provides easier comparison between different powders than the Hall flow meter. Flowability can be negatively impacted by oxidation of the particle surfaces of the powder, and has been shown to increase with larger particle sizes [6]. Attributed to higher surface energies on smaller particles, flowability of finer particles was significantly lower than for larger particles [6]

Spreadability deals more with the ability to distribute the powder in layers for powder bed processes [6, 20]. As this involves the powder being pushed and forced over other particles, it can be related to powder feeding for cold spray. For powder feeding, usually a rotating disk with a channel milled in the surface is used to feed the powder at a consistent rate from a container into the spray [1]. When the powder agglomerates or does not flow well, the feeder can become jammed, interrupting the flow of powder into the spray and significantly decreasing the deposit quality as a result of this lack of powder. While not within the scope for this research, this behavior is something to keep in mind for spraying, as it can be an indication during the process that the powder condition has changed.

2.3. Particle impacts

Single particle impact studies have been conducted to experimentally examine the factors that influence bonding during cold spray [15, 17, 21–24]. These involve using a very small amount of powder and, instead of a traditional cold spray nozzle and gas setup, the powder is spread out on a multi-material launch stage, usually based on a glass microscope slide. A single particle is selected and imaged on top of the launcher. Rather than use high-pressure gas like with cold spray, a laser is used in these experiments, which super-heats and ablates portions of the launcher assembly, propelling the particle towards the substrate [22]. The particle flights and impacts are monitored with high-speed cameras to determine the flight velocity and behavior as it relates to the specific particles. The impact sites are primarily examined with SEM, TEM, or an optical microscope which shows the level of deformation and bonding for each particle impact and, for those below a threshold velocity, the complete lack of bonding and resultant rebound of the particle [22, 25]. This threshold velocity is called the critical velocity, and it varies depending on the material. The particle's size and shape have an influence as well due to drag effects in the gas stream and in the nozzle [10, 21]. An oxide present on the surface of the particle can require more energy to break down during impact, and so may require a higher critical velocity [9, 21]. The exact influence of oxides on the adhesion of cold spray powders and their behavior is expanded on in Section 2.3.2.

Solid bonding during impact is often attributed to shear instability at the interface of the particles and substrate that results in particle deformation and mechanical interlocking [9, 10, 16, 22, 23]. This contact has been investigated with finite element modeling as well as in-situ observation of the exact impact behavior [16, 22]. If particles do not have sufficient energy to embed in the substrate, they will rebound, turning the impact into much more of a peening or tamping effect on the substrate or previous deposit layers [16, 22, 25]. This rebounding is nicely illustrated in Figure 2.4, where the smaller of the two aluminum particles does not have sufficient energy to embed, despite having a higher velocity. The factors affecting this are discussed in the following sections.

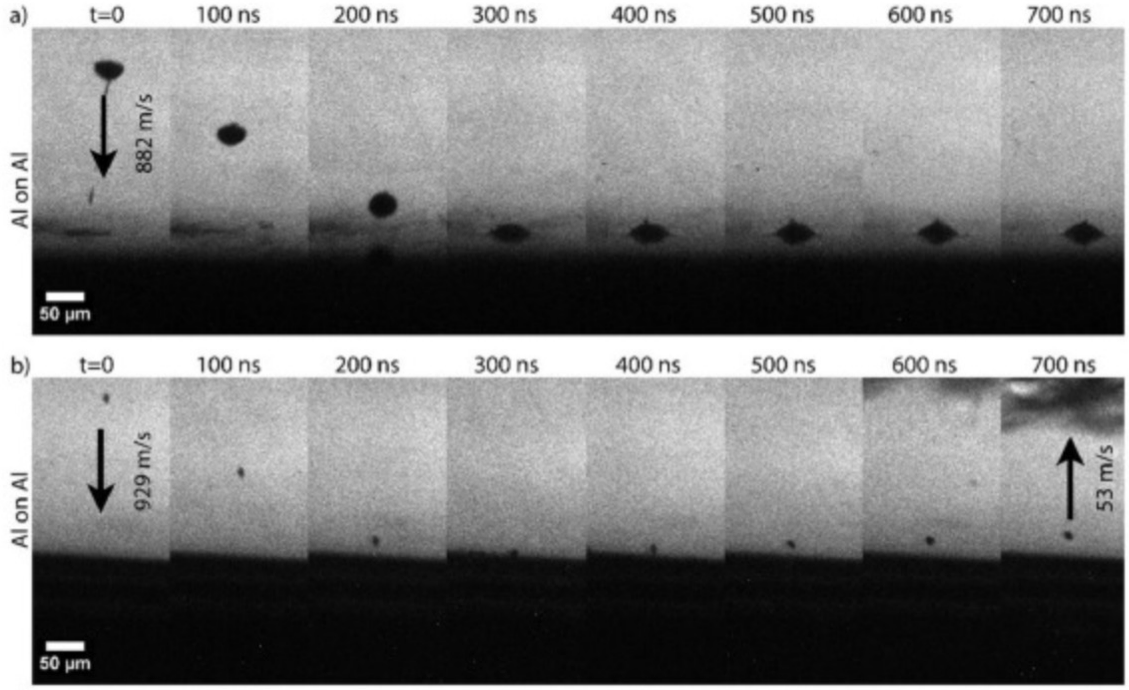

Figure 2.4: a) Impact of 32.6 μm Al particle on Al substrate, b) rebound of 9.4 μm Al particle from Al substrate, from Dowding et al. [22]

As with the general consensus related to shear instability, a phenomenon known as ”jetting” is commonly accepted to be present during particle impacts [15, 17, 21, 22]. This is where the very high shear loads force material out from the assumed-spherical particle in a wave. Due to the spreading material, droplets can form, knocking away oxides present on the substrate or surrounding particles. Modeling as well as observation of the impact sites of single particles has been done by various researchers to understand the phenomenon and its effects on the deposit [10, 21].

Lienhard et al. [21] investigated the impact of single particles of aluminum with varying oxide layer thicknesses. They determined that despite the relatively thin oxide layer, there was an effect on the jetting of material around the particle impact sites. Particles with thicker oxides had both smaller jets and smaller deformation regions on the substrate around the particle.

Due to the high velocities and heated spray gas, one might expect that the particles may undergo melting at impact, and that this is what causes adhesion to the substrate. However, rather than fully melting, the high kinetic energy of the sprayed particles is converted to plastic deformation and heat during impact, and this combination is responsible for such excessive deformation. Research suggests that the temperature of the particles at impact is around half the gas temperature in the spray plume before considering any adiabatic heat generation due to the impact [26]. Dowding et al [22] found that the temperature at the leading edge of the jet, which experiences the most severe deformation and displacement, remained below the melting temperature of the respective materials (aluminum and titanium). Through finite element modeling, they also analyzed this behavior as a function of particle size. Even for larger particles that generate more heat during impact, the jetted material remained below the melting temperature, though to a lesser degree (nearly 200 °C increase from 5 μm to 50 μm) [22].

The previously studied impact behavior is for generally spherical particles. While not likely to occur from gas atomization for aluminum, irregularly shaped particles behave differently on impact than spherical particles. Examining the impact behavior of dendritic copper compared to spherical copper, Winnicki et al. [10] modeled both particle types with finite element methods alongside an experimental assessment of the flight velocities. They found that the dendritic particles deformed less quickly compared to spherical particles during impact. These dendritic particles were highly irregularly shaped, and were modeled like Figure 2.5. This shape was taken to be an extreme in terms of irregularly shaped particles that still had a net shape that was roughly spherical.

Figure 2.5: Representation of a dendritic particle similar to one modeled by Winnicki et al. [10]

While gas atomized aluminum is expected to be generally spherical in shape, there is potential for satellites or agglomeration. These can alter the shape and could influence the impact behavior, though likely not to the same degree as the oxides would.

2.3.1. Critical velocity of cold spray powders

Cold spray differs from other powder metallurgy-based manufacturing methods since the metal powders are not totally melted and primarily kinetic energy is added to the system by the gas stream. While Zhang et al. [26] found the gas temperature imparted some heat to the particles in the gas stream, the only regions of melting or near-melting temperatures on the particles during impact were located at the very edges of the jetting material, and not the total volume of any particle [22]. The velocity of the particles exiting the nozzle depends mainly on their size and shape, along with the type of gas used and its temperature and pressure [3, 8, 10, 22, 26]. For aluminum powders, the gas used is either helium or nitrogen, as they are non-reactive and do not encourage oxide formation or growth. Helium is preferred for higher-quality coatings with higher density and better mechanical performance, but comes at a significant monetary cost [3, 16]. Because of its lower molecular weight compared to nitrogen, helium can accelerate the powder particles to higher velocities within the nozzle without melting them, resulting in higher deformation of the particles on impact and improved bonding [3].

Nitrogen is used more frequently than helium as it is renewable and can produce good coatings and solid bonding, as long as the conditions are correct [16]. The cost of nitrogen is significantly lower and allows for more spraying opportunities given a certain budget [1, 16].

Regardless of the gas used, the critical velocity of any given powder is heavily influenced by the size of the particles, as this dictates the surface area and mass that will be accelerated by the spray gas through the nozzle. The dimensions of the length and the throat of the nozzle determine the amount of time that any particle has to be accelerated by the stream before exiting the nozzle towards the substrate. Thus, larger particles, which have more mass, would require more time to reach the same speeds as smaller particles. As such, the typical exit velocities for larger particles are lower than those for smaller particles [16, 26]. However, because of their higher mass, these larger particles also have a lower critical velocity necessary to create good bonding with the substrate. The result of this is illustrated in Figure 2.6, where at a given gas temperature, only the larger particles in the size range have an impact velocity above the critical velocity and can adhere to the substrate.

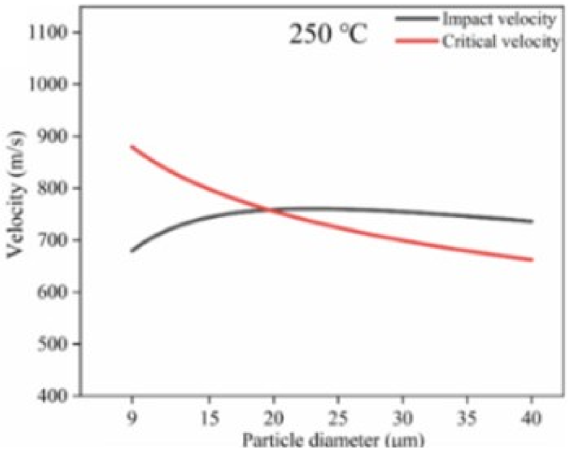

Figure 2.6: Velocity versus particle diameter for aluminum powder, from Zhang et al. [26]

Smaller particles, while capable of reaching higher speeds in the spray due to their lower mass, require a higher critical velocity for impact. This is because of two primary factors. Firstly, the lower mass has an effect on the kinetic energy and to reach the same level of energy the velocity of a smaller particle needs to be higher. The second is that there is a bow-shock effect from the high pressure gas stream meeting the substrate and forming a region of turbulent gas rebounding off the surface in every direction just on top of the substrate [16, 26]. This is represented in Figure 2.7. Every powder particle needs to overcome this, and the smaller, lighter particles without sufficient velocity contributions to their kinetic energy can be pushed aside and away from the surface instead of making contact and contributing to the deposit [16]. The bow shock effect is increased with increasing pressure of the spray gas, while temperature does not have an effect [26].

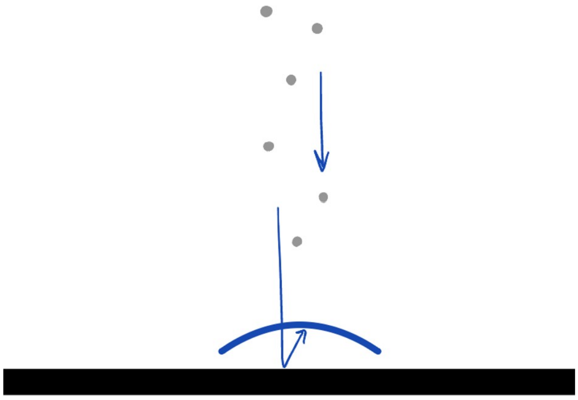

Figure 2.7: Bow-shock effect caused by pressure buildup of the spray gas rebounding off of the substrate

Related to the difference between larger and smaller particles is the effect that shape has on the critical velocity. Spherical particles have a very smooth surface that does not catch the spray gas flow but rather allows large portions to flow around them with little resistance. Irregularly shaped particles, which generally are not a concern with gas atomized powders (aside from satellites) have surfaces that cause more drag, accelerating the particles to higher velocities as a result [10]. Thus, an irregularly shaped large particle will travel at a faster speed than a regularly shaped equivalently large particle. Whether this kind of behavior carries over to gas atomized powders with satellites, and the magnitude of this effect given the likely proportion of powder particles that are satellites, is a potential knowledge gap.

Investigation into the critical velocity of individual particles has been done in several ways, along with monitoring the effects of various conditions. Dowding et al. [22] investigated unspecified aluminum alloy powders on aluminum substrates, as well as titanium powders on titanium substrates with single particle impacts and tracking with a high speed camera whether particles impacted or rebounded. Based on the number of particles of given sizes that either impacted or rebounded, they experimentally determined the critical velocity as that at which 50% of particles would adhere. This value varied with the particle size as well as being different between the aluminum and titanium materials. This is a well acknowledged method for defining the critical velocity [15]. The critical velocity has also been described by a power-law relation to particle diameter [22, 26].

During spraying, the critical velocity itself is not measured. Rather, a spray velocity or an approximation of the impact velocity of the powder particles can be measured using a camera to monitor the spray plume. The critical velocity can be determined before or after spraying is complete based on the powder characteristics and the spray settings of pressure, temperature, and working gas. Operators can compare this to the measured spray velocity as a way to monitor the deposition of powder. Those researchers that evaluate or measure both the spray velocity and the critical velocity note that the spray velocity should be from 1.3 to 1.5 times the critical velocity to achieve solid bonding [1, 27].

Once the type of process gas has been selected, the main process alterations that can influence the velocity of the spray are the temperature and the pressure that the gas is set to reach for spraying. Interestingly, while researchers have studied the effect of these variables on the resulting velocity, the steps by which they adjust either temperature or pressure by are inconsistent, and makes it difficult to see the full influence of one over the other. The critical velocity has a significant effect on the deposition efficiency: the amount of particles actually adhering to the substrate compared to the amount of feedstock. Zhang et al. [26] tested their reduced order model for deposition efficiency that results in process maps of temperature, pressure, and associated exit, critical, and impact velocities taking into account particle size effects. With this, they noted that the temperature increase of the gas had a more significant impact on deposition efficiency than pressure increase.

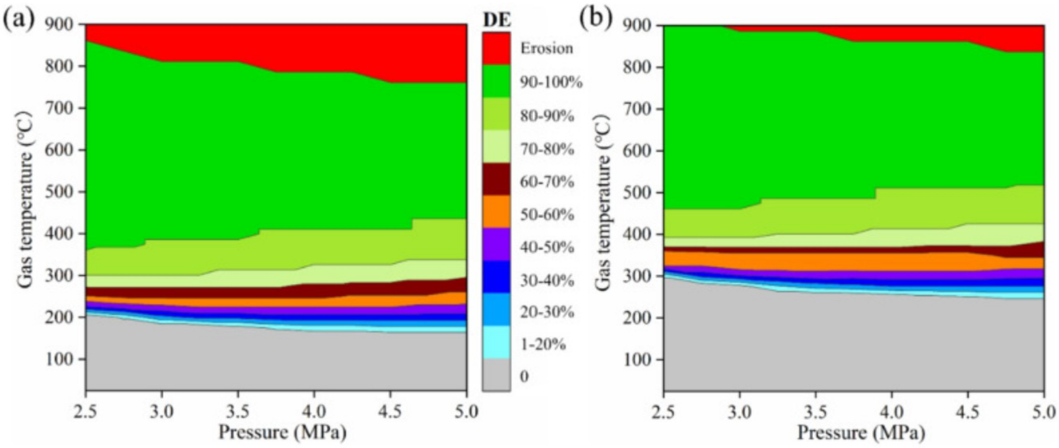

Figure 2.8: Process map of sprayability of aluminum powder in two system validation tests, from Zhang et al. [26]

The authors acknowledge that the variation in the temperature between various tested settings was up to a factor of 4 while the variation in pressure was only to a factor of 1.7 [26]. Figure 2.8 shows the process map generated by their model and validated in two cold spray systems. It shows that the most efficient method to increase the deposit efficiency is to increase the temperature to have an impact velocity sufficiently higher than the critical velocity. This is also supported by Huang and Fukanuma [3], who compared variations of temperature and pressure along with process gas to the critical velocity of copper powder.

Very interestingly, another study done by Winnicki et al. [10] found that pressure was more significant in altering the velocity of the sprayed particles than temperature. They found that changing the temperature from 673K to 873K only increased the particle velocity by 7 m/s. Maintaining a constant temperature and altering the pressure from 0.7 to 0.9 MPa increased the particle velocity by 24 m/s. This study was for copper instead of aluminum, and the spray gas was air rather than nitrogen or helium. This means that the velocities (particle and critical) are lower and the differences between them are likewise smaller than for aluminum. However, the disagreement is indicative of a potential area for further investigation, especially given the likelihood of a decrease in velocity using the same process settings. It would be valuable to determine how altering the temperature and pressure can adjust the spray velocity, and what effects the (expected) increase in temperature or pressure may have on the deposit as a whole.

Additionally, Na et al. [15] found that heat treatment of the aluminum powder did not significantly affect the critical velocity. However, they found that de-gassing the powder in a vacuum chamber reduced the oxygen content sufficiently to lower the critical velocity and increase the deposition efficiency compared to the untreated as-received powders. They traced the lack of influence of heat treatment to the combined effects of coarsening of the internal structure of the particles and oxide thickness increases. These factors combined to offset each other and had minimal effect on the critical velocity. This implies that without similar micro-structural adaptations over time, if the oxide is becoming thicker, there can be a more significant influence on the critical velocity and the bonding capability. Cycling the powder through a vacuum chamber, and observing a drop in the critical velocity due to lower oxygen content, indicates a clear relationship between oxidation levels and critical velocity, as reinforced by other authors (Kang et al. [17], Razavipour et al. [28]) investigating the various effects.

With a similar result to this, Lienhard et al. [21] examined the critical velocity of powders conditioned in different humidity environments, testing as-received powder along with those conditioned at 50% and 95% relative humidity (RH) for 4 days each. They found that there was little difference between the critical velocity for as-received and 50% RH powders. There was a significant increase (125 m/s) for the 95% RH condition, along with observed differences in the surface oxide film. The original behavior and a lower critical velocity was then somewhat recovered from the 95% RH powder after cycling it through a vacuum desiccator for 4 days to remove excess hydration without continuing growth of the oxide. This suggests that some portion of the humidity influence (related to oxidation) can be returned but that there are other factors at play that do not allow for complete recovery of behavior with the removal of humidity.

2.3.2. Oxide layer effects

The presence of oxides influences bonding through the critical velocity and their relative strength or thickness, as has been observed in literature quite thoroughly. The oxides can interrupt adhesion of particles on the substrate if they are not broken up during the impact or with the movement of material jets around a deformed particle [15, 21, 22]. However, they also more directly affect the impact and bonding between particles and substrate during the several nanoseconds of contact and impact. Even with a high enough critical velocity for a particle to adhere, there is no guarantee of a good bond with oxides present. Some researchers, referenced by Ko et al. [25], posited that any oxides present on the particles break away during spraying by impacting each other, which the authors disputed during the course of their own research. It is clear from analyses of copper, titanium, and aluminum powders that oxides are present at the interface between the substrate and impacted particle, despite high energy impacts forcing large deformations [9, 15, 17, 21, 23].

The native, spontaneously formed oxide layer on aluminum can be altered depending on the conditions of its environment. Naturally, this is related to the storage of powders for cold spray which is discussed in a later section, as well as the possibility of heat treatment depending on the alloy. For AA6061, which is designed for heat treatment, the oxides form thicker layers with further treatment, increasing the critical velocity to fracture these oxides and achieve solid bonding [15]. During the heat treatment, the underlying structure within the particles becomes coarser, leading to a relative softening of the material that happens at a similar rate to the oxide becoming thicker with exposure to heat over the time of the treatment.

Lienhard et al. [21], in investigating the critical velocity differences between various oxide conditions on aluminum powder particles, related the oxide thickness to the impact behavior and jetting of material during impact. The oxide layer present at the interface between particle and substrate fractures in several locations as the jet is formed by excessive pressure. These fractured oxides remain within the jet and the material that deformed around it, as illustrated in Figure 2.9, and the thickness of the oxide is a determining factor in the size of the jet. More considerable oxide layers were found to decrease the size of the jet, which implies less material movement and potentially decreased bonding as a result.

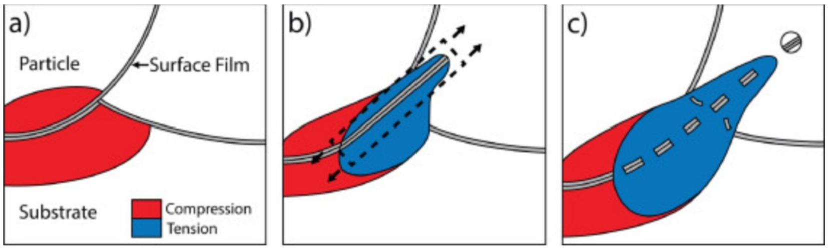

Figure 2.9: Progression of jetting: a) shock wave created on impact, b) localized tension created when shock wave detaches from the leading edge of the interface, c) jet formation when tension exceeds local strength and fractures the trapped oxides from Lienhard et al. [21]

As mentioned in the section above related to critical velocity, these researchers tested several powders subjected to different RH environments for 4 days. The oxide layer of the 95% RH powder was found not only to be thicker than the other two conditions, but also had irregular thicknesses on the individual particles examined [21]. The thickness of the oxide and its regularity (or otherwise) thus affects the quality of the bonding between particle and substrate.

This outcome is supported by similar works from Navabi et al. [9] and Chen et al. [23], which also found that the oxide that remains unbroken on the impacting particle is located at the very bottom, the ”south pole”. This was investigated by Navabi et al. with SEM-EDS at the boundary between the substrate and an impacted particle, shown in Figure 2.10.

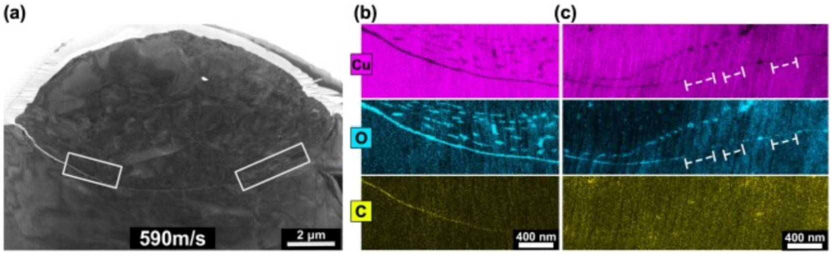

Figure 2.10: SEM-EDS investigation of impacted copper particle interface with substrate showing a) SEM image of impact (white boxes examined with EDS in (b) and (c)), b) EDS analysis of left boxed portion from (a) based on copper, oxygen, and carbon signals, c) EDS analysis of right boxed portion from (a) based on copper, oxygen, and carbon signals showing metallic bonding with dashed lines and high concentration of oxygen and carbon signals which make up the oxide and contamination on the particle surface from Navabi et al. [9]

The radius of the residual oxide in this region was found by Navabi et al. to decrease with increasing oxide thickness. It is also reliant on the velocity at impact and the size of the particle. A higher velocity results in a smaller unbroken oxide and as a result, better bonding is expected. Smaller particles also have smaller regions of unbroken oxides compared to larger particles.

Clearly the oxide layer is known to influence the impact and the critical velocity of the particles. The intensity of its effects can depend on the oxide thickness, the spray velocity, and the size of the particle. The flight velocity of particles in the spray plume, however, seems to be independent of the oxide presence or alteration. As observed by Razavipour et al. [28], albeit with copper particles, the growth of the oxide over time, and even the continued oxidation reaction changing the type of oxide [25] had no effect on the velocity of the particles in flight.

2.4. Oxide measurement and composition

Whether formed during gas atomization or any other portion of the powder preparation process, oxides begin to grow on aluminum in the presence of even trace amounts of oxygen [15]. The thickness of this oxide layer has been found by researchers in two ways. The first involves energy dispersive X-ray spectroscopy (EDS) [5, 15] and X-ray photoelectron spectroscopy (XPS) [5, 9, 21, 28] mapping of the oxygen content in the powder sample through a number of scans. These are analyzed by the machine software to provide a spectrum where the peak indicates the location of the oxide, and fitting of the curve to determine the full width half maximum of the indicative peak specifies the oxide’s thickness [5, 15]. With this method, especially using cross-sectioned particles and examining through the thickness of the oxide, any layered behavior of the oxide becomes apparent from changes in the expected signals within the depth of the oxide [5].

Interestingly, while XPS was used to examine a large number of particles in an area scan by Lienhard et al. in Ref. [21], they also used TEM to investigate single particle oxide thicknesses. They found reasonable agreement to their XPS results, though the higher variation resulting from using individual particles and the smaller examination area for TEM led to them using the XPS results for comparison and analysis.

There appears to be some disagreement between researchers regarding the thickness of the oxides formed on gas atomized AA6061 powders. Overall, most are in agreement with an oxide thickness on AA6061 powder of around 5 nm after gas atomization [5, 9, 21, 29].

However, Na et al. in [15] found oxide layer thicknesses in their as-received powder of 16.8 nm, and also tested the effect of several heat treatments on the oxide thickness. These all resulted in even thicker oxide films of 17 nm, 18.9 nm, 24 nm, and 24.7 nm with increases in the temperature and time of the associated heat treatments. And, while measuring at the interface of a deposit instead of a single particle surface, Kang et al. [17] investigated with TEM and found a resulting oxide thickness of 150 nm between the substrate and the deposited coating, yielding very poor bonding. It is not clear from the study whether this was more related to the particles or the substrate or as a result of both together. This indicates a strong effect of oxides on the bonding between the substrate and impacting particles, with such a distinct intermediate layer discernible.

As for the composition of the oxide, this depends somewhat on the alloy composition along with the oxidation conditions [5, 9]. Investigation with XPS and STEM-EDX by Navabi et al. [9] found a layered structure to the oxide film for AA6061 powders. This included an aluminum oxide layer on the inner layer with a magnesium-rich portion as the outer layer. The aluminum oxide thickness was, in line with the general consensus mentioned above, found to be 5.2 nm, and those regions with the magnesium oxide present had thicknesses up to about 2 nm.

In terms of the structure of the oxide, it can be crystalline with ordered planes or amorphous with less structural order. A crystalline structure to the oxide means that more energy is necessary to dissolve the bonds and break down the oxide than an amorphous structure. This is generally more of a concern when using thermal processes since the melting temperature of these oxides are very high (above 1000 $^\circ$C) [30]. For cold spraying, the oxides are broken up only mechanically during impact so the structure is less important than the presence and thickness of the oxides.

The structure of the aluminum oxides was determined by Navabi et al. to be crystalline, on top of the crystalline AA6061 particle. The additional magnesium layer was posited to be amorphous due to a lack of crystalline fringes matching known crystalline oxides or spinel [9]. The structure of the oxide seems to be a point of contention, especially depending on the conditions that the powder is exposed to.

Similarly, Ernst et al. [5] found a separation in the apparent oxide layer. This was seen with higher concentrations of magnesium in the outer layer and a scarcity of magnesium in the inner layer. The thickness was found to vary depending on heat treatment condition. However, for gas atomized powder, they identified both oxide layers to be amorphous, rather than having a crystalline outer layer as Navabi et al. suggested. Both found identical thicknesses of oxide to be 5.2 nm on the gas atomized powder.

Ernst et al. [5] also found that with various heat treatments, the oxide grew to be thicker as well as developing a crystalline outer layer and maintaining the amorphous inner layer. The outer crystalline layer generated at 230° C was identified as a $MgAl_2O_4$ spinel. A higher temperature homogenization treatment of the powders resulted in a further layer of $Al(Mg, Al)_2O_4$ spinel below the remaining $MgAl_2O_4$ spinel outermost layer.

This behavior and layering was traced back to the gas atomization process of manufacturing the powder, where magnesium can become segregated towards the outer surface and thus available for oxidation reaction [5]. They also posited that, in addition to a higher humidity or heat treated condition, potentially the high temperatures during cold spraying could encourage further oxide growth. This was not evaluated during the study, as they examined the powders before spraying. This is a potential area for investigation with respect to the coating quality and development of the oxides over time.

Na et al. observed the expected increase in thickness of the oxide with time and temperature during heat treatment, and presumed that the structure was semi-crystalline in comparing to other authors' works [15]. They also refer to the prior work by Lienhard et al. [21], where the initial oxide was determined to be likely amorphous but can become semi-crystalline with water absorption or thickening over time. This particular behavior was explained in a work referenced by Lienhard et al. which describes the nucleation of crystalline forms of $\gamma - Al_2O_3$ at the interface between the bulk aluminum and its amorphous oxide layer as oxidation continues [31].

The study from Lienhard et al. [21] also investigated the oxidation and hydroxidation behavior of AA6061 powders. They found that the native oxide would further develop in high humidity environments, and for powders stored in 95% RH for 4 days, both the thickness and the apparent composition of the oxide layer changed. The time-dependent behavior of oxides on aluminum powders in typical storage conditions, rather than high humidity environments, has not been a focus of research, and is a research gap that can be filled with this thesis.

2.5. Storage conditions and time

As mentioned related to the powder production, several packaging options are available for manufacturers to ship their powders. As outlined in the Department of Defense document about powders for cold spray, the shelf life is dependent on the storage container and conditions of the powder [13]. They outline three scenarios in order of suitability with regards to shelf storage containers for cold spray powders. The reason for declining suitability is the potential for permeation of fouling agents like oxygen into the packaging over time. They also recommend that powders that have been stored for one year or more are evaluated for quality before use. The packaging scenarios are as follows [13]:

1. Sealed in electrically conductive containers in an inert environment. Individual containers packaged within metal container to prevent transport damage. Containers of sufficient quality to maintain inert atmosphere and prevent oxygen or moisture until opened for use
2. Sealed in electrically conductive containers. Individual containers packaged within metal container that includes desiccant packets to absorb permeating moisture
3. Sealed in electrically conductive bags. Individual bags packaged within plastic container to prevent transport damage

The main concern with the packaging of the powder is the permeation and infiltration of water or oxygen that will react with the powder and reduce the flowability and other characteristic behaviors. With a better seal, the shelf life of unopened powders is improved. While it was acknowledged that powders over one year from production should be evaluated for use, the ways in which the powder would degrade in this time were not expanded on.

Once a package is opened, the material enters the service life, where the environment and conditions around the package can have significant influence on developing oxides [15, 21, 25, 28]. For this purpose, desiccant packs are included with the powder to reduce the amount of hydration possible within the package. While the influence of high humidity environments has been evaluated [21], the effect of any airborne hydration becoming trapped in the packaging between uses has not been evaluated.

2.6. Research questions

The research gaps in existing literature surrounding the topic of powder degradation and the relation to the coating performance highlighted several areas for investigation in this thesis. The oxidation process can begin as soon as powders are produced, and the discourse surrounding the baseline oxidation condition of the powder provides an opportunity to identify how this may vary between manufacturers and different powder batches. Similarly, few studies into the evolvement of oxides over time in typical storage conditions leaves the gap to study incremental changes in the powder that users could experience. These research gaps led to the primary research question in this work:

1. How does time elapsed between delivery and use of powder affect the quality of cold spray deposits?

And, in support of the primary question, two sub-questions were created. These were designed to inform users how these changes in the powder would affect cold spraying of products, with the ultimate aim of improving coating performance:

1. What is or are the cause(s) for this behavior?
2. How does this affect the mechanical performance of the coating?

3

Methodology

The methodology followed in the thesis included two primary phases: powder characterization at progressive time intervals, and particle launches and spraying to determine any influence on the adhesion of particles and coatings. This allowed for focusing on the powders themselves over time, and then using the particle launches and spray tests as a measure of the cumulative effect of time on the powder during the thesis. Powder characterization methods included Raman spectroscopy, X-Ray Diffraction (XRD), and examination with a Scanning Electron Microscope and Energy-Dispersive X-ray Spectroscopy (SEM-EDS). Particle launches were facilitated at the Innovation Campus of Mines Paris-PSL, and coating application was achieved with the cold spray system installed at SAM XL in Delft.

3.1. Materials

This research was based on the influence of time on particle behavior during spraying. To accomplish this, several different powders were studied and evaluated against each other. The main focus was on the aluminum AA6061 alloy, and there were two different suppliers for this alloy. To maintain confidentiality of the suppliers, these have been anonymized simply as Supplier A and Supplier B. The nominal composition of AA6061 for use in cold spray, as specified in the detail specification ”Powders for Cold Spray Deposition” (MIL-DTL-32495) [13] is shown in Table 3.1.

Table 3.1: Composition of AA6061 alloy [13]

Element	Cr	Cu	Fe	Mg	Mn	Zn	Si	Ti	Al
Composition (Wt%)	0.04-0.35	0.15-0.40	< 0.70	0.8-1.2	< 0.15	< 0.25	0.40-0.80	< 0.15	Balance

Most of the spraying with AA6061 powder at TU Delft and SAM XL used a batch of powder from Supplier A produced in June 2024. This powder was used in the research as an ”old” powder, since it was approximately one year old, meeting the recommended re-evaluation timeline suggested in detail specification MIL-DTL-32495 [13]. A fresh batch, produced in June 2025, was used as a ”new” powder from the same supplier. The AA6061 powder produced by Supplier B was opened in February 2025, and so had a total time exposure somewhere between the other two batches.

While not the same alloy, a very old batch of AA2024 powder was also included in the study, to determine if the influence of much longer time exposure could be identified on the powder. This powder had been in storage for over a year before being delivered and opened in December 2024, and was previously found to be near-impossible to spray using the available cold spray machine. The nominal composition of AA2024, also from the MIL-DTL-32495 detail specification, is shown in Table 3.2.

Table 3.2: Composition of AA2024 alloy [13]

Element	Cr	Cu	Fe	Mg	Mn	Zn	Si	Ti	Al
Composition (Wt%)	< 0.1	3.8-4.9	< 0.5	1.2-1.8	0.3-0.9	< 0.25	< 0.5	< 0.15	Balance

The powder samples used in this research were stored in small containers with screw-on lids. The lids were also kept in place with tape to ensure a secure fit during any transport. The containers were kept at room temperature and approximately 50 % relative humidity. The information relating to the production and batch details for the powders is summarized in Table 3.3

Table 3.3: Powders used in the research

Powder	Alloy	Produced	Opened
Supplier A Old batch	AA6061	June 2024	November 2024
Supplier A New batch	AA6061	June 2025	September 2025
Supplier B	AA6061	Unknown	February 2025
AA2024	AA2024	Unknown	December 2024

For the single particle impact testing, the launchers and receivers were provided by Mines Paris-PSL. The launchers were based on glass microscope slides, and the receiver substrates were thin sheet 1xxx series aluminum. Two different thicknesses of this sheet were used between the four testing iterations of single particle launch experiments. In three iterations, a thinner sheet of 0.25 mm was used, and in the fourth and final iteration the thicker sheet material of 0.5 mm was used.

For the spray test, an AA6061 aluminum plate was used as the substrate material. It was prepared for spraying with Scotch-Brite abrasion and wiped with ethanol to remove any dust. The bar was 6.5 mm thick, 24.5 mm wide, and 415 mm long. For the spray testing, the powder materials used were only the three AA6061 powders, since the AA2024 powder was not able to be sprayed with the existing machinery setup.

3.2. Powder Characterization

The powders were characterized at approximately two-week intervals. In total, three methods were used to characterize the powder at each time interval. In this way, the size, shape, surface behavior, and overall composition of the powders were monitored throughout the research. The techniques for powder characterization were Raman spectroscopy, X-ray diffraction, and scanning electron microscope with energy dispersive X-ray spectroscopy (SEM-EDS).

Raman spectroscopy relies on inelastic scattering of laser light through the material to determine the chemical state, constituents, and internal strain of a given sample [32]. It requires no preparation of the sample, and can be used for point or area analysis; providing a spectrum of frequencies in response to the laser excitation. Characteristic frequencies of certain materials, indicated with a series of peaks at specific locations in the spectrum, are used to identify what materials are present. Depending on the height, width, and location of these peaks, information about the crystallinity, structure, and internal strain within the material can be determined by comparison to reference spectra [32, 33]. Alterations in these features between different spectra indicate changes in the associated material behavior. With this, the development and alteration of the powder itself over time could be assessed in combination with the other two techniques. Raman spectroscopy functions well as a supplementary data source and can be further supported.

X-ray diffraction allows for identification of the crystal lattice planes and arrangement, with the indicative peaks denoting the presence and quantity of such features in the bulk material. Depending on the diffraction angle of the x-ray source, each crystal arrangement can be identified in the scan result. Rietveld refinement is the method by which the crystallographic peaks in the resulting spectra can be decomposed into the respective materials or phases that comprise them. Each crystal arrangement, like the (111), (200), and (222) planes are detected at different diffraction angles θ during the measurement. The matching of peak locations can be done by hand, though it is often inaccurate and time consuming, or a program can derive the locations of the various peaks by means of the crystal lattice arrangement of the compounds and phases. The program used in this thesis was Profex [34], which is free to use and has a material library already installed. Some compounds and phases not included in the system were downloaded from the Materials Project [35], an online database with structural and chemical information for thousands of compounds, as identified by researchers and literature.

The premise of a scanning electron microscope is to send electrons at the surface of a specimen and measure the energy of rebounding and ejected electrons. From this, the features of the specimen become visible on a very small scale and high magnification. Depending on the specimen position within the observation chamber, different electron detectors are better placed to get clear images, due to the path they can take from the surface of the specimen to reach the detector. For the JEOL JSM-7500F used in this research, some of the clearest images with information about the composition of the specimen were obtained with the retractable backscatter electron detector (RBEI) inserted immediately above the specimen. This additional detector permits observation of the composition with a compositional view of a specimen using compositional (COMPO) mode.

Also included in the SEM system is a EDS system produced by Oxford Instruments. This goes one step further than the COMPO view and allows identification of materials based on the specific energy of the measured electrons. Elements with lower atomic numbers, like hydrogen and helium, cannot be detected by this system. It measures x-ray photons that are released by electrons moving between different bands within the atoms (caused by the electron beam displacing atomic electrons). Elements without additional electron bands do not produce these signals or have minimal responses [36]. Even boron, carbon, and oxygen can be difficult to detect due to their low atomic number. This is a limitation of the method of EDS that can affect measurements.

3.2.1. Raman Spectroscopy

This research was conducted with a Renishaw inVia Confocal Raman Microscope. Spectra were collected using a 50x magnification lens, a 532 nm laser operating at 5% power, with an exposure time of 10 seconds per accumulation - of which 20 were taken to reduce noise - for each sampling point. Given this is a non-destructive test method, the powder was placed into the observation chamber with no preparation needed, and was returned to the container after each test.

After each scan was complete, the original file was saved. Due to the duration of measurement, some features can appear in the spectrum that are not indicative of the sample at all. These are interference from galactic cosmic ray radiation (GCR) which are random events that are picked up during the Raman spectrum measurement [37]. With the in-built software, WiRE (version 4.4), these artifacts were removed, so any peaks on the spectrum were resulting from the sample rather than the environment.

Also present was a background spectrum, which shifted the measured spectrum upwards, though not linearly. This was also accounted for in the software, by subtracting the baseline. This resulted in a flatter spectrum from which peak fitting was used to identify the feature locations and properties. The fitted curve data was saved in a spreadsheet to facilitate comparison between different samples and iterations' peak behavior.

3.2.2. X-Ray Diffraction

This research was conducted with a Rigaku Miniflex 600 XRD device. The surface of the sample holder (Figure 3.1) was prepared with carbon tape to ensure sufficient coverage of the powder. A sample of the loose powder was scooped from its container and dropped onto the surface of the carbon tapes. Sufficient powder was used to fill the basin until the top, which was then pressed flat with a glass slide.

Figure 3.1: Empty powder sample holders for the XRD

The prepared sample was placed into the machine. The sample holders fit and magnetically lock into a rotating sample stage within the machine, shown in Figure 3.2. This permits observation of the various crystal arrangements within the full sample.

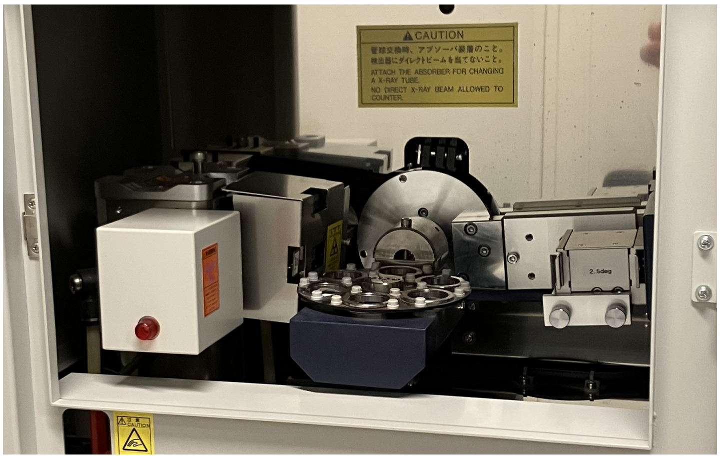

Figure 3.2: Inside the RIgaku Miniflex 600 at DASML. Rotating sample stage has space for 6 specimens at once

The measurement parameters for each of the powders were: scan range of 20-80°, scan speed of 1° per minute, and scan step of 0.005°. All other general and measurement settings were kept as normal for the existing setup.

Following the measurement, the saved files were viewed with Profex, a software designed for Rietveld refinement of peak locations and heights to determine composition. Along with a chosen list of elements and phases, the software matches peak locations to the known database values and calculated locations based on lattice information to find a best fit to the measured spectrum.

The elements and phases chosen to be included in the refinement are listed below in Table 3.4. The phases differed between those included for the AA6061 powders and those for the AA2024 powder, since these two alloys have different compositions. A trial and error approach based on likely compound formulations in literature was used to identify the phases that best matched the alloy contents and manufacturer-tested composition [38] [39] [40].

Table 3.4: Phases included in the Rietveld refinement of the XRD measurements for the two alloys

Alloy	Phases
AA6061	Al, Al_2Cu, Al_2CuO_4, $AlCuO_2$, Cu, Cr, Fe, Mg_2Si, $MgAl_2O_4$, Mn, Si, Ti, Zn, $\alpha - Al_2O_3$, $\delta - m - Al_2O_3$, $\delta - o - Al_2O_3$, $\gamma - Al_2O_3$, $\gamma' - Al_2O_3$, $\kappa - Al_2O_3$, $\theta - Al_2O_3$
AA2024	Al, Al_2Cu, Al_2CuO_4, Al_4Cu_9, $AlCu$, $AlCu_3$, $AlCuO_2$, Cu, Cr, Fe, Mg_2Cu, $MgCu_2$, Mn, Si, Ti, $TiAlCu_2$, Zn, $\alpha - Al_2O_3$, $\delta - m - Al_2O_3$, $\delta - o - Al_2O_3$, $\gamma - Al_2O_3$, $\gamma' - Al_2O_3$, $\kappa - Al_2O_3$, $\theta - Al_2O_3$

After the refinement, the chemical composition was analyzed to determine the changes in oxygen content and oxides that took place between iterations.

3.2.3. Scanning Electron Microscope and Energy Dispersive X-Ray Spectroscopy

This research was conducted with a Jeol JSM-7500F Scanning Electron Microscope. Because a small portion of powder was used, a 12.5 mm sample holder was used. For the powder samples, a carbon tape on top of a cylindrical sample holder insert was necessary so that the vacuum did not displace the powder during degassing or observation. Once the carbon tape was placed on the insert, a small amount of powder (from whichever supplier was being measured that day) was scooped from the container onto the tape.

Any excess was knocked off back into the sample powder container, which was then closed again. Compressed air at a small standoff distance was used to remove any remaining loose particles and to make sure the particles were forced into contact with the tape. The insert was placed into the sample holder and the screws on the side were tightened. An example of a prepared sample and sample holder is shown in Figure 3.3.

Figure 3.3: Powder from the New batch of AA6061 from Supplier A prepared in the sample holder for measurement from October 6 2025

Once the sample was in the observation chamber of the SEM, imaging began at 15kV and 10μA. Focus was found at the edge of a particle at the highest magnification possible (14,000x for low magnification (LM) and 40,000x for SEM). Starting with LM LEI mode, various sections of the sample were imaged at increasing levels of magnification. Regions of interest were noted to be examined with EDS. Higher magnification images were taken with SEM mode, in LEI, SEI, and COMPO detectors for different perspectives of the particle features.

From the SEM-COMPO images, EDS analysis was performed. This utilized an Oxford Instruments Ultimax EDS detector installed with the SEM. Regions of interest were first mapped for aluminum, silicon, oxygen, zinc, copper, iron, manganese, chromium, titanium, and magnesium. These are all listed components from the powder detail specification, with the exception of the oxygen, in both AA6061 and AA2024 (whether in high amounts or with lower maximal values)[13].

Following the mapping, point identification at various locations on the particle surfaces was carried out. This permitted specific features to be identified as having particular compositions. The results from the mapping and point identification were saved in reports for later analysis.

3.3. Single Particle Impact Testing

In collaboration with the materials research center at Ecole des Mines, PSL, single particle impact experiments were carried out. The name for this technique varies amongst researchers: LIPIT (Laser Induced Particle Impact Testing) from Ref. [22] and others, or LASHPOL (LAser SHock POwder Launcher) from ref. [24] and others. The premise of this technique is to launch single particles at a model substrate, and image the flight with a high frame-rate camera (up to 300,000 fps was used) to determine on a particle-by-particle basis what the conditions for adhesion or rebound are for a powder-substrate system.

LASHPOL testing required construction of launchers and substrates. The launchers were based on glass microscope slides, with a piece of polyimide (PI) tape on one surface, then a small piece of ultra-thin aluminum foil with colored ink covering both sides, and another piece of PI tape to keep it in place. A prepared launcher is shown in Figure 3.4.

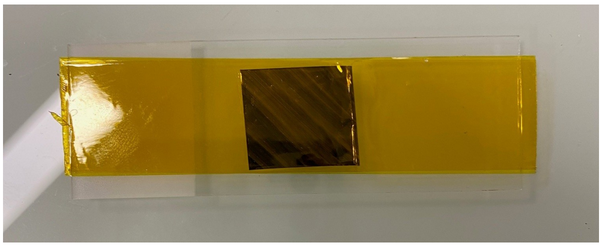

Figure 3.4: A prepared launcher

A small sample of powder was dispersed in ethanol to facilitate placement on the launcher. Using a microscope for viewing (Figure 3.5), a single particle could be placed on the taped side of each launcher, within the region of the foil.

Figure 3.5: Microscope for single particle placement and alignment on particle launchers

To control the number of particles and their position, a combination of paper towel (rolled to give a point), wooden toothpicks, and cotton swabs were used. The paper towel was dipped into the ethanol-powder dispersion, taking up some ethanol and leaving particles on the surface. This was gently placed on the top surface of the launcher, depositing between 1 and 20 particles, depending on the dispersion. When only a single particle was placed, this was manipulated with the toothpick to ensure it was not an agglomerate of several particles. When multiple particles were placed, several were moved aside and subsequently removed from the launcher with the cotton swab, and the single particle remaining was adjusted to ensure it was not an agglomerate. This process is illustrated in Figure 3.6.

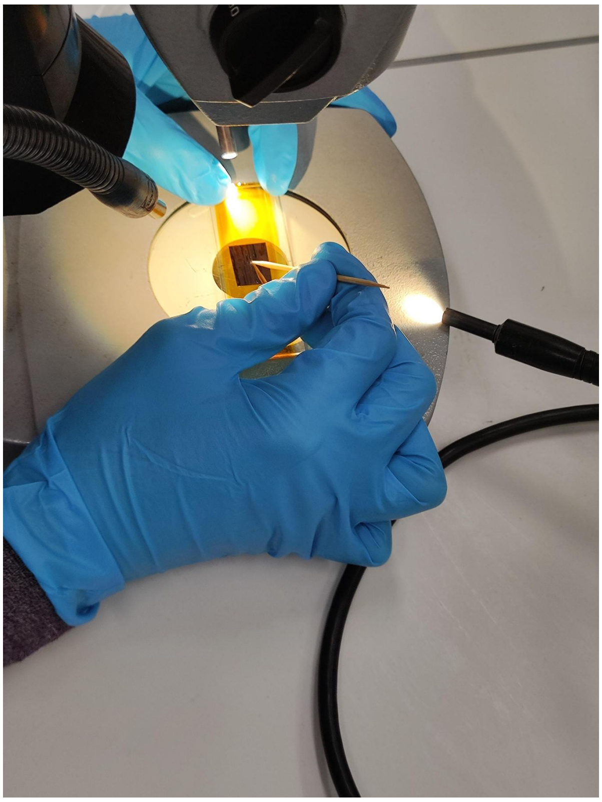

Figure 3.6: Moving particles on the launcher with wooden toothpick under microscope

When a single particle was located correctly and any others were removed, the position was marked with a pen. Lines were drawn outwards from each side of the particle, and the launcher was labeled with an identifier. An example is shown in Figure 3.7.

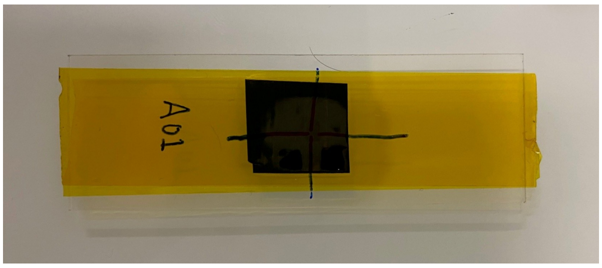

Figure 3.7: Marked launcher A01

Each prepared launcher was then taken to a Keyence VHX-1000 optical microscope to measure the placed particles. Each launcher was imaged and measurements of equivalent ellipses were taken, since few particles were spherical. An example is shown in Figure 3.8.

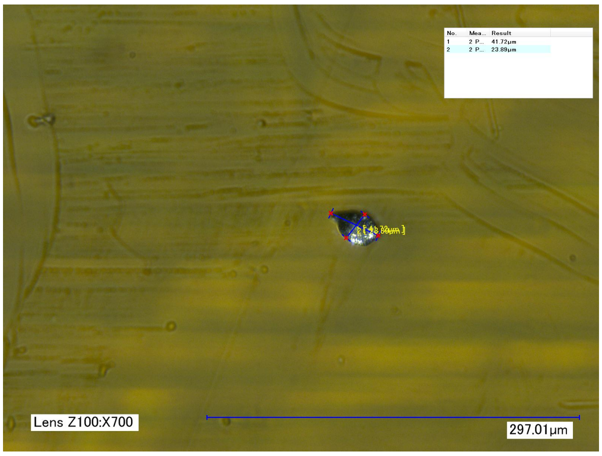

No.	Mea...	Result
1	2 P...	41.72μm
2	2 P...	23.89μm

Figure 3.8: Particle A03 at 700x in VHX-1000 microscope, with measurements of major and minor axes for size determination

The other half of the preparation materials for LASHPOL were the receivers. These model substrates were prepared on capped posts which (at that facility) are also designed for SEM sample holding. A section of double sided tape was placed on the flat cap portion, and an approximately 1 cm square piece of aluminum sheet was placed on top. Several examples are shown in Figure 3.9.

Figure 3.9: Receivers prepared with thin sheet 1xxx aluminum

Once prepared, the substrate was placed into the holder, which is shown in Figure 3.10a and fixed in place. This holder was slotted into holes on the alignment carriage that maintain a fixed distance between the launcher and the substrate. These holes are visible in Figure 3.10b near the middle of the image, circled in red.

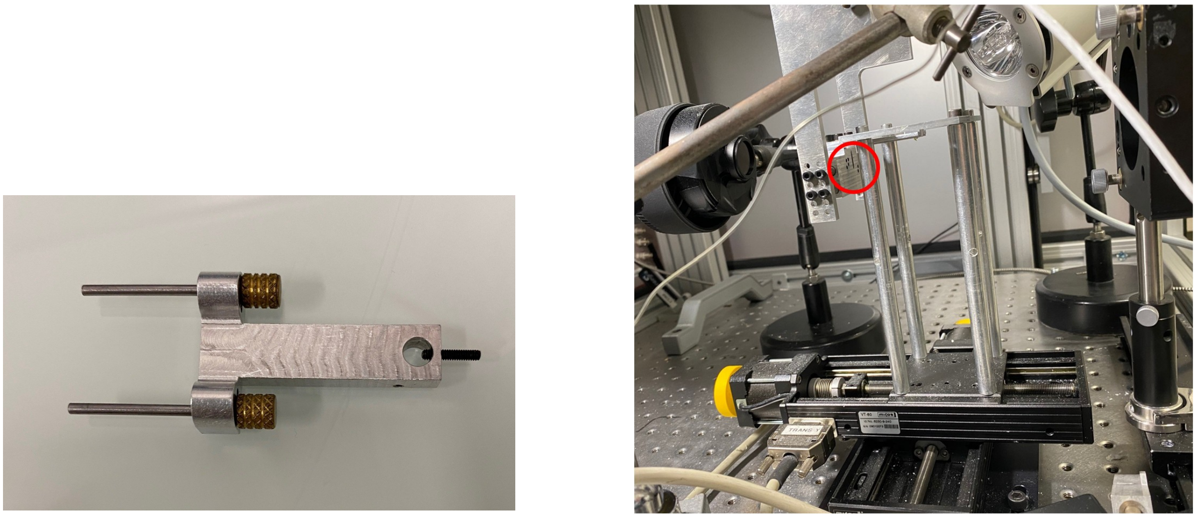

(a) Removable receiver holder, with a clamp controlled by the threaded rod to keep a receiver in place

(b) The carriage for the launcher-receiver system, with holes (highlighted by the red circle) located for the receiver holder to slot into to keep fixed distance between launcher and receiver

Figure 3.10: Receiver holder and full carriage setup for sample holding in LASHPOL

The launchers were placed on their own section of the mobile carriage, shown in detail in Figure 3.11. The edges of the two-piece launcher holder (indicated with yellow arrows in the figure) have a ledge machined in so that the launchers remained flat and supported on all sides.

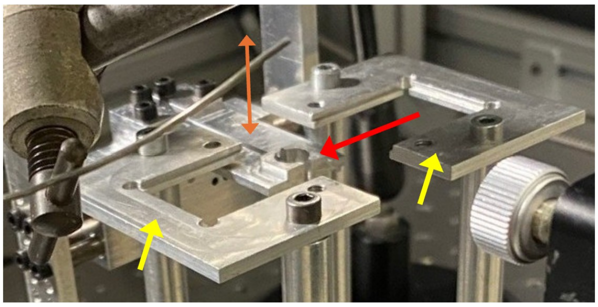

Figure 3.11: Launcher holder and ”guidance path” for the LASHPOL. The launcher holder (in two parts, indicated with yellow arrows) is static in the vertical direction, though moves in X or Y to align the laser, and the guidance path (indicated with the red arrow) can then have the vertical position adjusted (as illustrated with the orange arrows)

The middle section (where the red arrow is pointing in Figure 3.11), which is part of the assembly for holding the receivers, can move up or down. This will be referred to as the guidance path, as the particle traverses through the milled hole towards the receiver when launched. Once the launcher was placed with the particle facing downwards, the position of the eventual laser shock was adjusted. The entire carriage had motorized control operated by a joystick inside the cabinet. This is shown in Figure 3.12.

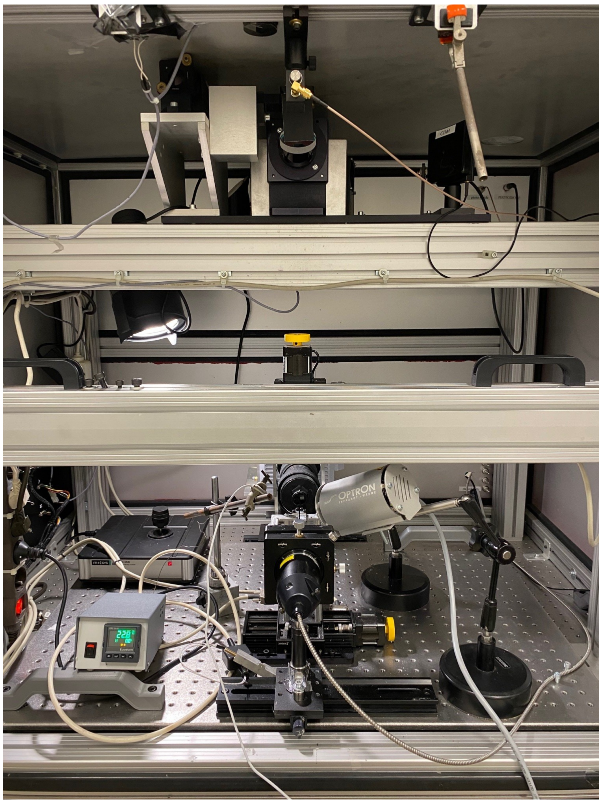

Figure 3.12: Full setup in LASHPOL cabinet with motorized stage control for alignment of the laser pulse

Also controlled here was the vertical position of the guidance path. As mentioned above, this portion of the setup is set at a fixed distance from the receiver. To ensure focus of the receiver surface in any images taken, this needed to be moved upwards to remain in frame of the recording camera. The second reason to move this section upwards is to restrict the total deformation in the immediate area of the laser shock, so the energy can translate into particle motion rather than moving the launcher. After each launcher was placed and aligned, the position of the guidance path was moved until it just touched the launcher. This ensured the flight path was in view of the camera and the deformation of the launcher was minimized.

The experiments began with using the New powder from Supplier A and the thin aluminum substrate material (0.25mm). A total of 18 particle launchers were prepared and used for this iteration. Based on the preliminary results from this iteration, the decision was made to add particle and substrate heating for following iterations.

To facilitate testing where both the particle and substrate were heated, two heating elements were used. The first was used to heat the particle. This was an infrared heat source and accompanying sensor, which were both directed at the top surface (that will be struck with the laser shock) of the launcher plate. The second heating element was encapsulated in a housing that fit onto the end of the substrate holder, along with a thermocouple that threaded into a hole on the side to monitor the temperature of the substrate. The heating setup is shown in Figure 3.13

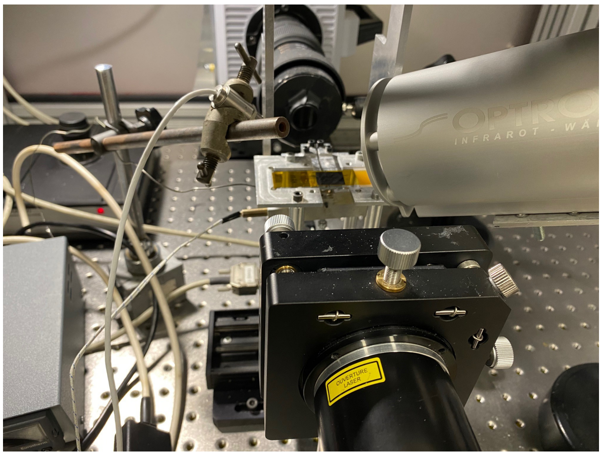

Figure 3.13: LASHPOL setup with heating elements installed for particle and substrate

In order to fit the thermocouple wire, the substrate holder was inverted compared to Figure 3.10a. This shortened the total distance between the launcher and the receiver as a result, due to the shape of the holder. As is seen in Figure 3.14, the top surface of the holder in this arrangement is not milled down from the level of the placement pins, which resulted in a shorter path for the particle to travel. The frequency of the imaging camera and that of the accompanying illumination laser were adjusted to accommodate this shorter distance: from 200kHz to 300kHz. This ensured that each launch could be observed even with the shorter flight time.

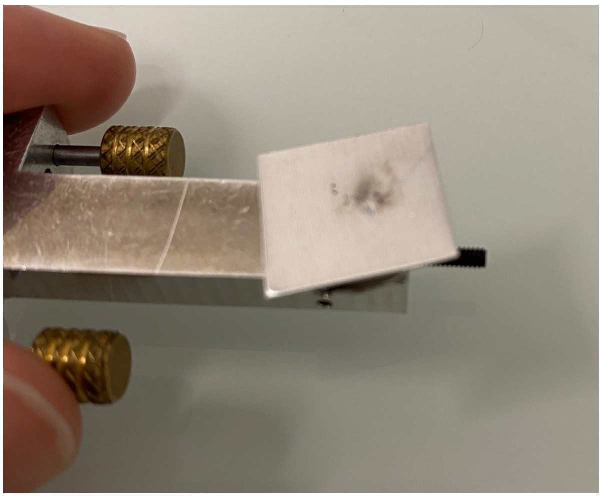

Figure 3.14: Receiver holder for the heated arrangement, with a tested receiver still in place. The hole for the thermocouple wire is visible below the receiver

The laser source used for the launch was a Thales Saga 330 laser, a 532 nm wavelength source with maximum energy of 1.8J for a pulse of 5.2 ns. The illumination laser was Cavilux HF, and the imaging was done with a Phootron SA 1.1 camera [24]. The camera operated at either 200kHz (room temperature experiments) or 300kHz (heated experiments) depending on the test requirements.

When a pulse was triggered, both the shock and illumination lasers were fired, to send the particle and to capture the launch images, respectively. The laser power used varied between 1.348 J and 1.672 J by altering the position of the polarizer. These values were last calibrated in 2021, so some differences to the true number were possible, though it was expected to be consistent across each testing iteration.

After each test, the saved images were examined to determine if the particle rebounded or adhered to the receiver as a splat. For those image sequences that were obscured or missing entirely (due to known issues with the illumination laser), the receivers themselves were examined by eye and with magnification to determine if they were worth keeping for future examination. Normal practice would be to discard receivers without a splat and prepare them for re-use.

Because of the imaging issues, more receivers were retained than normally would be. Some receivers were examined with a SEM (Zeiss Gemini) at Mines Paris-PSL, and each receiver that was kept was examined again with the equipment at DASML.

Each receiver that was saved was examined with the Keyence VHX-2000 optical microscope at the DASML for evidence of rebound or splat. Rebounds are particles that failed to adhere to the substrate, and splats are single particles that had sufficient energy to stick to the substrate and deform. Regions of interest were imaged and height profiled to determine if they were concave or convex from the substrate surface. Comparisons were also made to the previous microscope images of the particles on their launchers. This helped to determine whether the size of features was representative of the particle or of debris resulting from the launch. Locations of splats or rebounds were marked on the edges of the receivers with marker, to facilitate further examination of relevant regions.

Some receivers were also observed in the Jeol SEM at DASML, to perform EDS analysis on both splats and rebounds. These were held in place in the 12.5mm sample holder with two semicircular inserts, as shown in Figure 3.15.

Figure 3.15: LASHPOL specimen A03 fixed in the SEM sample holder

The Z height of the sample was carefully controlled in the SEM to ensure no collision with the RBEI detector, which was necessary for taking COMPO images. The location of each splat or rebound to be examined was found by using the marks on the edges of the receiver, and focus was found on the surface. EDS mapping of the surface included the substrate material and any relevant feature. As with for the particles themselves, the selected elements were aluminum, silicon, oxygen, zinc, copper, iron, manganese, chromium, titanium, and magnesium.

After mapping, specific regions of interest were analyzed with point identification, to establish what occurred during the rebound or splatting to the material and its oxides. As with the powder analysis, the results were saved in reports for further analysis.

An overview of the LASHPOL testing iterations and their associated details is given in Table 3.5. All LASHPOL testing preparation and launches were completed within 4 days.

Table 3.5: LASHPOL experimental iterations

Iteration	Supplier	Batch	Heated	Identifier	Number of specimens	Substrate thickness [mm]
1	A	New	No	A	18	0.25
2	A	New	Yes	HA	13	0.25
3	A	Old	Yes	HB	13	0.25
4	A	New	Yes	HAT	10	0.5

3.4. Spray Testing

A sample spray test was conducted using the three AA6061 powders in this study to evaluate differences between them and any influence on the sprayability of the powders. The Titomic D623 medium pressure cold spray system is located at SAM XL, where the nozzle is affixed to a XYZ robotic controlled gantry inside the sealed spray booth. The system is capable of a maximum pressure of 20 bar and maximum temperature (with a water-cooled nozzle) of 800 °C.

Using the three AA6061 powders, New Supplier A, Old Supplier A, and Supplier B, two deposits were made for each powder. The first, using a typical coating-building nozzle traverse speed of 20 mm/s, deposited a thin coating of material in two strips across the substrate plate. The second, using a very high traverse speed, was intended to somewhat mimic the individual particle impact behaviors seen in the LASHPOL experiments, but with a larger number of particles. Similar high traverse speeds have been used to isolate particles for interface analysis [17]. For this, the maximum speed of the nozzle was used, which is 500 mm/s. The sprayed specimen is shown in the cold spray cabinet in Figure 3.16.

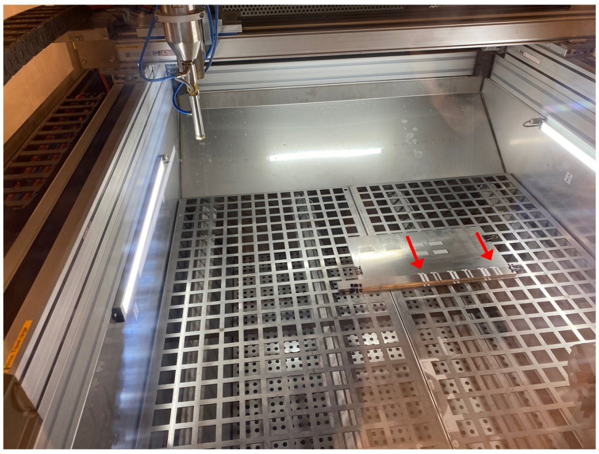

Figure 3.16: Spray test specimen clamped in the cold spray cabinet. From left to right: New Supplier A 20 mm/s, 500 mm/s; Old Supplier A 20 mm/s, 500 mm/s; Supplier B 20 mm/s, 500 mm/s. Beginning and ending of the sprayed sections indicated with red arrows

Just before spraying with each powder, the nozzle was moved into position at the HiWatch CS2 camera. This allowed for a velocity, particle size distribution, and particle density measurement to be made. Then, the nozzle was moved to the spray path over the substrate.

The surfaces of the sprayed sections were imaged and height profiled with the Keyence VHX-2000 at the DASML, with representative images taken from one region on each deposit. One representative image and height map was taken for each spray path. Thus, for each powder, there were two sets of images for each traverse speed.

The thicknesses of the coatings were measured, since time did not permit cross section examinations, as a first comparison between the different powder's coating behavior. This was measured with a caliper by taking the height of the deposit and substrate minus that of the substrate alone.

4

Results & Analysis

The results of the research are presented here. As in the methodology, the results of the powder characterization which took place over several intervals of approximately two weeks is presented first. Then, the results of the LASHPOL single particle experiments performed at the Innovation Campus of Mines Paris PSL are presented. Finally, the results of a spray test at SAM XL are presented, which produced a sample specimen and facilitated comparisons between the powders could be drawn.

4.1. Powder Characterization Results

In this section, the results and analysis following the powder characterization testing of Raman spectroscopy, XRD, and SEM-EDS are presented. They are divided by characterization method. Some initial comparison between results of different methods is included, with further elaboration to follow in the discussion.

4.1.1. Raman Spectroscopy Results

For each iteration, several spectra were collected from each powder. This included some spectra taken from different points on the same particles. Most of the data was collected from approximately similarly sized particles throughout a powder sample. It was found during this work that, even examining the same particle with the same parameters, the resulting spectrum could vary depending on position on the particle.

Generally, the spectra for the AA6061 powders looked similar, due to their composition and structure. Depending on the measured location on the particle or the particle size, the relative intensity of the features on the spectra varied. This was likely due to encountering different homogeneously distributed mixtures of the elements, influencing the surface measurement. A collection of representative spectra is shown in Figure 4.1, also showing the difference between different points measured on the same particle and variation between particles.

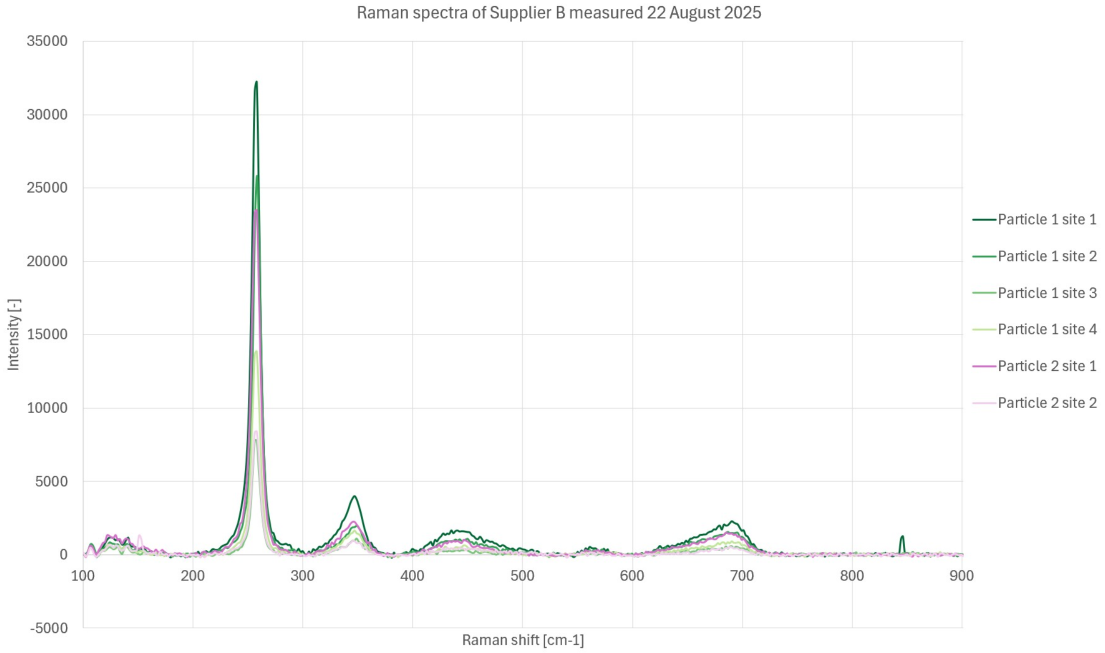

Figure 4.1: Raman spectra of AA6061 powder from Supplier B measured on 22 August 2025, showing typical features and variation in particle and site measurement locations

As is clear from the plot, the primary feature is the high peak at around 256 cm^{-1}. Several other small peaks are located at higher wavenumbers, and the portion with very low wavenumbers has the most overlap between the different measurements. The response of the material shown in the lower wavenumber regime (10-200 cm^{-1}) is related to lattice vibrations and the atomic arrangement [32].

The primary peak, being at a higher wavenumber than such lattice vibrations, also communicates more information. Because of the higher intensity, changes in the material response could be identified more easily. For the analysis, focus was given to ranges near this location for each of the collected spectra. Typically, the bonding between a metal and oxygen has strong (high intensity) characteristic peaks between 150-450 cm^{-1} [32]. Thus, for following the development or alteration of whatever form of oxide existed on the surface, using the peaks located around 256 cm^{-1} was a reasonable prioritization in the data analysis.

While some researchers used Raman spectroscopy to measure aluminum oxides, none had a similar spectrum result [41, 42]. Several utilized a larger range or found features in higher wavenumber domains. Despite using the full range of the available machine (up to 3200 cm^{-1}), none of the same features were visible in any of the collected spectra for this work. Only one source from literature had a high peak located near 256 cm^{-1} [43]. This plot highlighted the intensity of several peaks between 250-750 cm^{-1}, which were attributed to pure crystalline $\gamma - Al_2O_3$. For reference, this is shown in Figure 4.2.

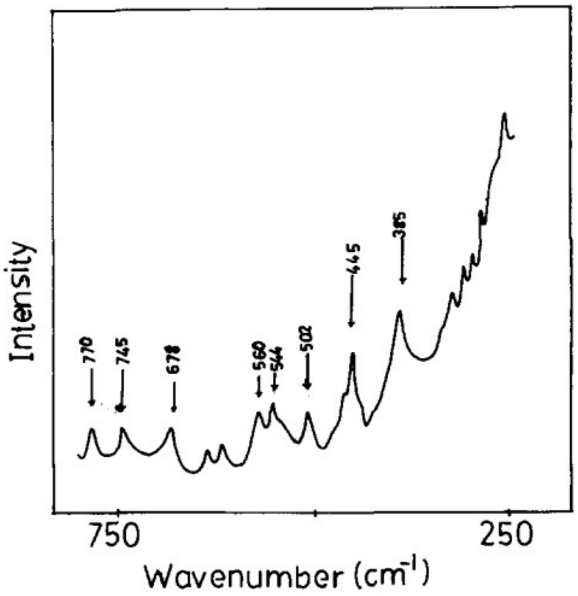

Figure 4.2: Raman spectrum of pure crystalline $\gamma - Al_2O_3$ from [43]

There are several phases of Al_2O_3 that can form. The most stable phase is the α phase, as this is the last evolution of the oxide and is most prevalent in nature. Energetically, this phase requires the least energy to maintain, and the other phases will gradually become $\alpha - Al_2O_3$ when conditions are correct. Returning to a previous phase or back to the original state requires more energy input [30]. These other phases are each metastable on their own, meaning that while they can be found, they are not as likely as α to be found. The metastable phases include $\gamma - Al_2O_3$, $\delta - Al_2O_3$, $\theta - Al_2O_3$, $\eta - Al_2O_3$, and $\kappa - Al_2O_3$ [30, 42, 44].

Historically, some of the phases were referred to by different names, or used symbols which were then allocated to other forms of Al_2O_3 [30]. Some phases have signals that overlap with those of other phases, and depending on the intensity of the signal, the presence of a phase could be attributed to a different one. Such an effect was noted by Boullosa-Eiras et al [42] in the Raman spectra of alumina phases. The peaks for the θ phase covered the features for the δ phase in some of their Raman data, making it more difficult to determine which phase was present and to what degree. Taking this into account meant that the primary peak observed in this data may or may not truly be related to $\gamma - Al_2O_3$ or a similar phase. Because of the relative intensity and legibility of this feature in the collected data, it was carried forward as the focus for the analysis and comparison. However, while the primary 256 cm^{-1} peak was very distinct for the AA6061 powders, it was not the same for the AA2024 powder. The AA2024 powder had much higher intensities in the lower wavenumber ranges. The features that were present around 250 cm^{-1} were much wider and appeared to be composed of two small peaks side-by side. An example is shown of the total measured spectrum in Figure 4.3.

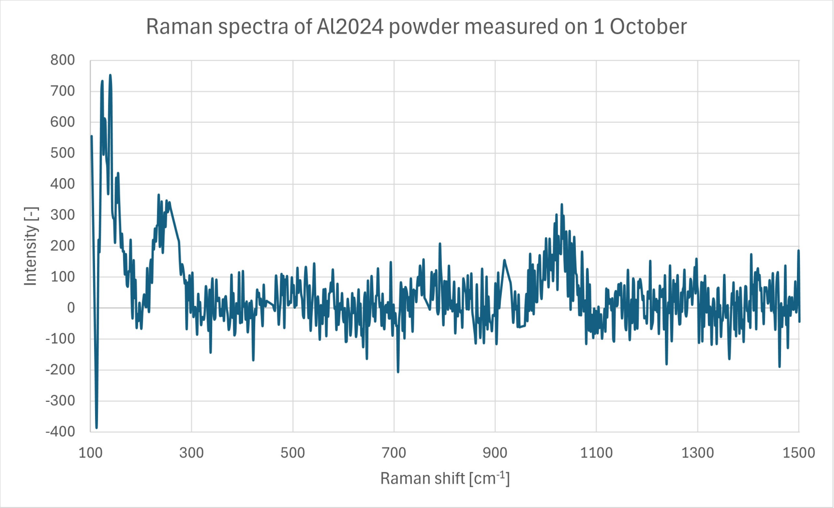

Figure 4.3: Raman spectra of an AA2024 particle measured on 1 October 2025, in the wavenumber range 100-1500 cm^{-1}

The above plot shows a somewhat post-processed spectrum. As such, it illustrates a ”negative” intensity in the lower wavenumbers, which was not truly the case. What was reported as a negative intensity on several of the plots was actually based on the difference between the true measured spectra and the applied baseline correction during preliminary data refinement. The baseline was filtered out by a best appearing fit to the reliquary curve that is always present during Raman spectroscopy. However, this did result in some points on the net spectrum being interpreted as negative once the baseline was established as the new Y=0 line. This is something that was present in each spectrum, though more visibly on some than others.

Also present in each spectrum for this powder was a small peak at around 1050 cm^{-1}. Despite some literature including higher wavenumbers such as this, there were no identified peaks in this location, so the likely cause was not determined [41, 42]. This range was also tested for exclusion purposes on the three AA6061 powders and there was no such peak or other small feature at 1050 cm^{-1}. So, selecting this range for comparison between the condition of the alloys was not prioritized.

For consistency in comparison, a similar frequency range (around the main feature at 256 cm^{-1}) was chosen for analysis of the AA2024 powder. This was due partially to the uncertainty regarding the exact material phases identified in the 200-300 cm^{-1} range. The other factor was the existence of a feature, though smaller in intensity, present in that section of the AA2024 spectra. To encompass the whole width of this feature, the wavenumber range of 200-400 cm^{-1} was the final selection for analysis and comparison with the other powders.

As far as consistency of the results, one feature set some powder measurements apart from others of the same alloy. This feature was seen in the spectra for the New batch from Supplier A. Along with the main peak being located around 256 cm^{-1}, some measured points included small shoulders to the right or left on this primary peak. These were not present in every spectrum on a given measurement date, and neither was the intensity consistent, as was seen with all the other powders and remarked upon above. This first became apparent with the measurement on 30 September 2025, the results for which are presented in Figure 4.4.

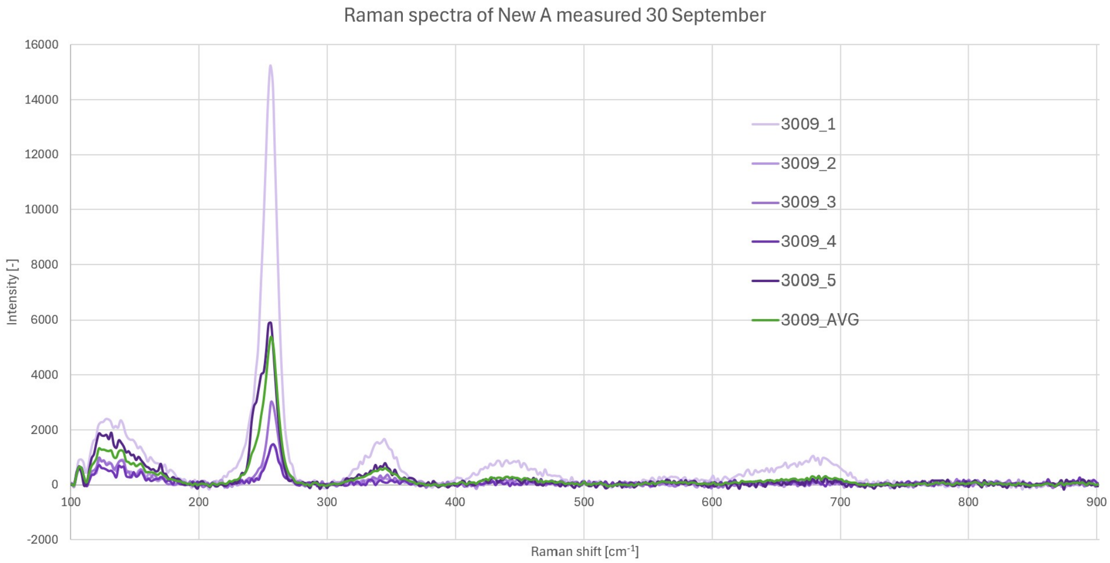

Figure 4.4: Raman spectra collected from the surface of 5 different particles from the New batch of Supplier A powder on September 30 2025, and their collective average

Given that the altered features were located at the primary peak, to ease the analysis an adjustment to the plotted data was made. Rather than plotting the overall intensities for the collected spectra, each measurement point was normalized to its maximum value, that of the primary peak. Thus, the vertical axis could shrink and examination of the differences between the primary peaks was simplified. This adjustment is presented in Figure 4.5.

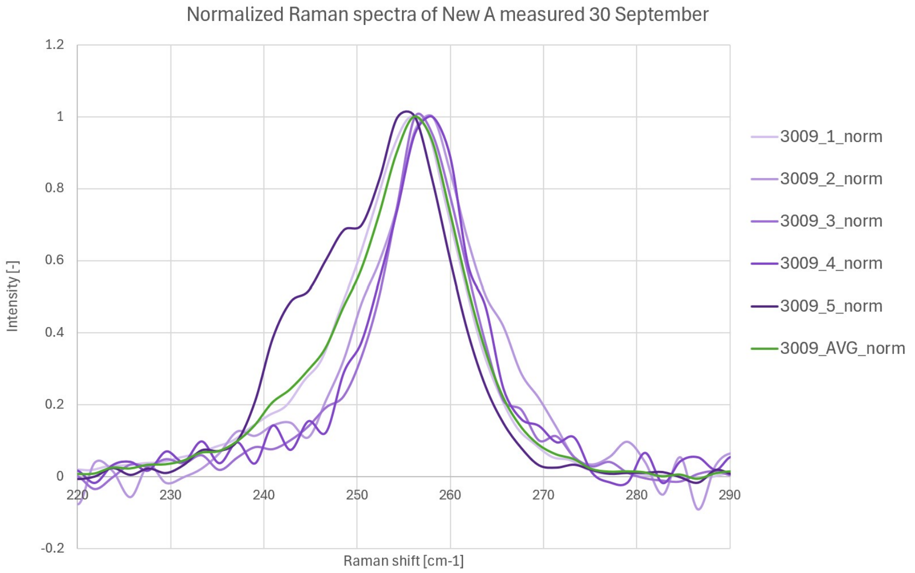

Figure 4.5: Normalized Raman spectra collected from the surface of 5 different particles from the New batch of Supplier A powder on September 30 2025 and their collective average, plotted in the range 220-290 cm^{-1}

Here several things are apparent. First, despite the exposure time (10s) and number of accumulations (20) being fairly high to reduce noise, the regions outside the higher intensity peaks had many fluctuations. While low level, such fluctuations could be interpreted as peaks themselves and so interpretation of the results was done with care. Second, the apparent location (in terms of Raman shift) of the primary peak appears to move depending on the specific particle being measured. This was assumed to be random variation due to sampling of the powder particles. Further testing on a variety of particle sizes and locations on single particles showed no clear pattern to explain this.

Third, the width of the peaks, with the exception of the fifth measurement, were similar to each other. This meant the crystallinity was similar between the measured particles, since the width of a peak indicates the degree of crystallinity and the relative size of the crystals of the compound it represents [33, 41–43]. The exact compound that these primary peaks represent was not clear. The expectation was that differences in behavior between the powders at different measurement dates would be reflected in the peak properties of the collected data, which was the case here.

Lastly, the shoulders that were present on the primary peaks of measurements 1, 2, 4, and 5, were not consistent in location or intensity. The most apparent was that of measurement 5, including two additional shoulders to the left of the primary peak. While peak-fitting this spectrum, a curve centered at 245 cm^{-1} was identified to fit alongside the primary located at 256 cm^{-1}. While this did not fit both of the shoulder features, it illustrated the degree of the spread outwards that their presence created. As with the width of a peak indicating crystallinity, also small changes in width can be traced to internal strain in the crystal. What is most indicative of strain in the crystal is a shift of any given feature to higher or lower wavenumbers [33, 45]. A shift leftwards, towards lower wavenumbers, indicates an internal tensile stress, while moving to the right towards higher wavenumbers indicates internal compressive stress. Since the baseline stress state was not known for certain, whether any shift left or right was simply a reduction in internal stress could not be concretely established.

To monitor any shifting of the peaks, average values for each measurement date were calculated. These were then compared (by batch) to the other measurement averages to have an indication of movement or patterns evolving from the primary peak over time. Figures 4.6, 4.7, 4.8, and 4.9 show the average spectrum results for each measurement date compared to others from the same alloy and batch. The spectrum from each measurement date is identified in the legend with the day and month (DDMM). They are each averages over the several collected spectral measurements per measurement date.

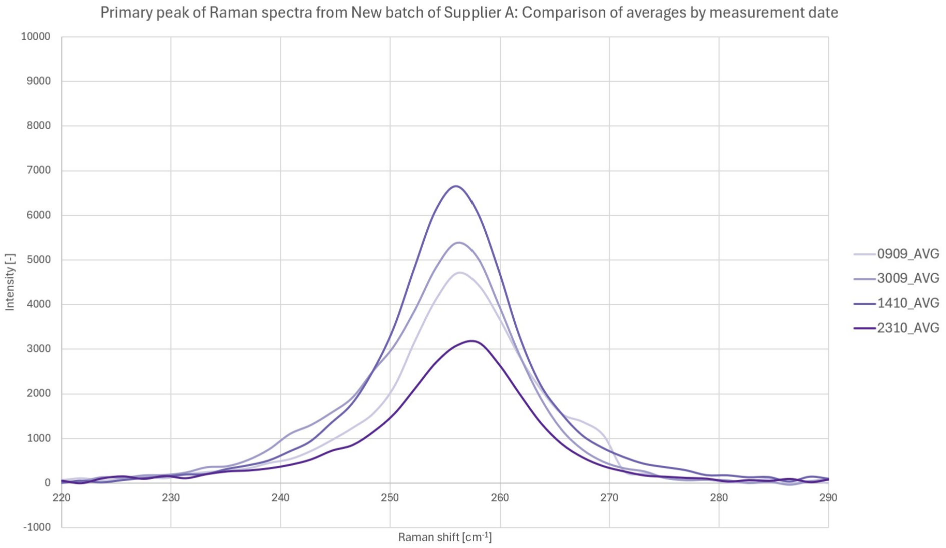

Figure 4.6: Comparison of primary peaks from measurement-date averaged Raman spectra for New batch of AA6061 powder from Supplier A, in the range 220 - 290 cm^{-1}

In the New powder from Supplier A, the influence of the shoulders being present in some spectra was also seen in the averages. The averages from 30 September and 14 October both show shoulders, though on opposing sides of the primary peak. There was no discernible pattern in terms of the intensity of the peaks. The intensity increased for the measurements on 30 September and 14 October of 2025, then dropped below the initial value with the measurement from 23 October 2025.

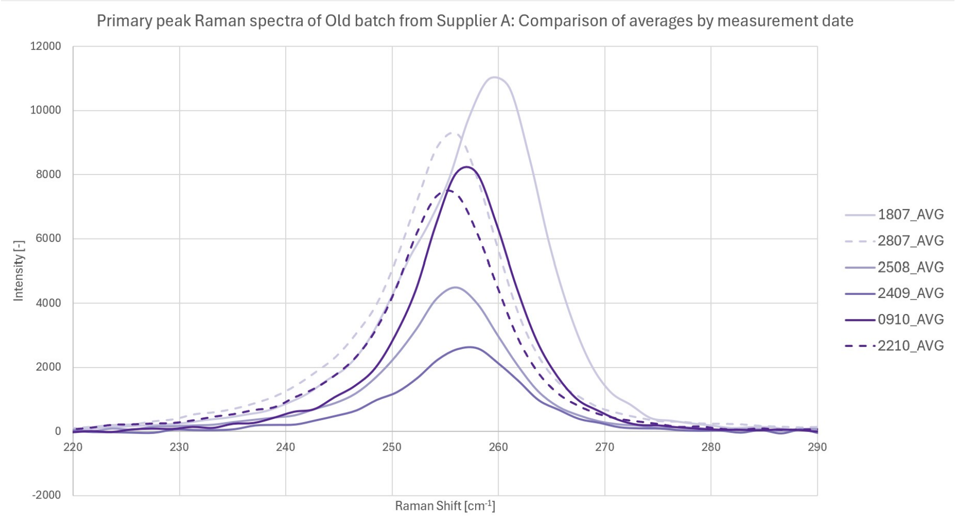

Figure 4.7: Comparison of primary peaks from measurement-date averaged Raman spectra for Old batch of AA6061 powder from Supplier A, in the range 220 - 290 cm^{-1}

There was significantly more variation in the general peak properties for the Old batch of powder from Supplier A. While there were no definitive shoulders present, the lateral shifting of the curves for the different measurement dates also implied internal changes in stress and strain, likely caused by phases shifting. No clear pattern was identified for the location of the peaks with time, since both leftwards (internal tensile stress) and rightwards (internal compressive stress) shifts occurred between measurement steps. However, the first and last measurements had the greatest variation, with a shift to the left by 5 cm^{-1}. This cannot be ascribed to any measurement error of the machine, as a typical Raman spectrometer is accurate to within 1-2 cm^{-1} [46]. Similarly, no clear pattern was found in terms of the intensities of the peaks with time, aside from a general reduction in overall intensity between the first and last measurement. Some of the measurements were collected while the Raman spectrometer had a minor calibration issue, which would arbitrarily lower measured intensities. The machine was re-calibrated and several more measurements that were made with the appropriate calibration also recorded lower intensities. This reduction in the peak height could have been related to increasing structural disorder (multi-crystallinity), reduction in concentration of the contributing material phase, or measuring a different crystal orientation. The most likely cause identified for this case was structural disorder or phase concentration, though the exact phase information could not be identified, as mentioned above.

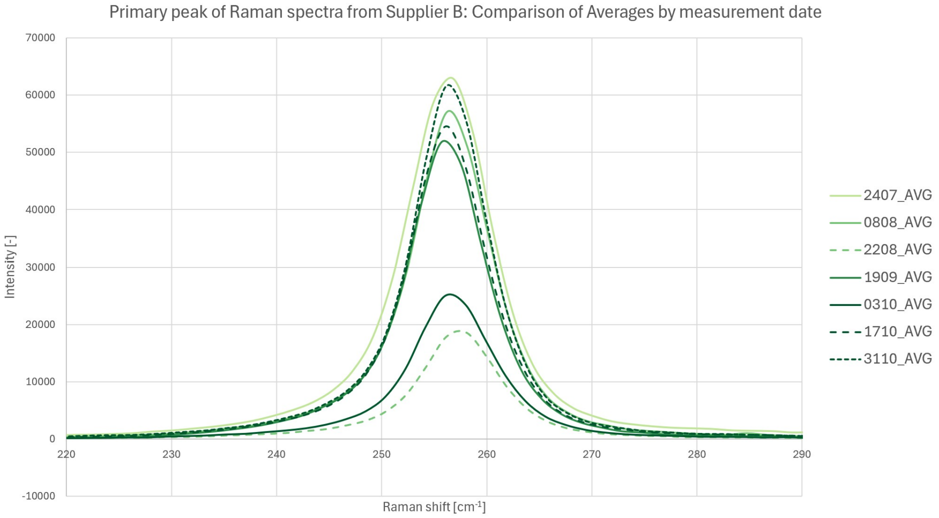

Figure 4.8: Comparison of primary peaks from measurement-date averaged Raman spectra for AA6061 powder from Supplier B, in the range 220 - 290 cm^{-1}

In the powder from Supplier B, the fairly high consistency in the peak locations made determining a pattern difficult. Despite having more collected measurements than the two powders from Supplier A, each of the peaks was located within the range of 255-257 cm^{-1} for Supplier B. This, compared to that of the Old powder peak locations being in a larger range, meant there was more stability from Supplier B. In the end, no pattern was clear in terms of the peak locations for this powder. While generally the height of the peaks was consistently high, the two lower intensity peaks from 22 August and 3 October 2025 made determining a pattern more complex. Unfortunately, as with the location of the peaks, no pattern was found for their heights from this data.

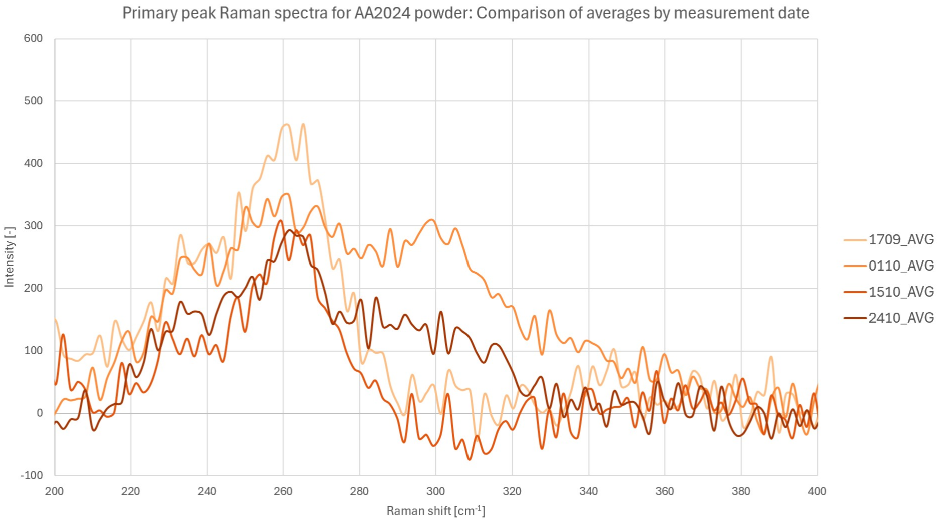

Figure 4.9: Comparison of primary peaks from measurement-date averaged Raman spectra for the AA2024 powder, in the range 200 - 400 cm^{-1}

The AA2024 powder spectra looked much different to those of the AA6061, especially in the chosen analysis range. There was one significant difference in the measurements included in Figure 4.9's spectra. On two of the measurement dates, 17 September and 15 October 2025, the lowest wavenumber selected for the measurement was 50 cm^{-1}. For the other two measurement dates, the lowest wavenumber selected for the measurement was 100 cm^{-1}. This caused an effective offset upwards in intensity for the spectra including 50 cm^{-1}. This upwards shift resulted from influence of some of the lower lattice vibration modes, which were not present in the spectra collected with 100 cm^{-1} as the lower bound.

The general pattern, while taking this upward shift into account and thus splitting the behavior into two different groups depending on the lower bound, was a decrease in intensity over time. While there were only two measurement points per state (these were still the averages of several measurements combined per date), the fact that the pattern held for each state made it more likely to be consistent regardless of state.

There was an additional broad feature to the right of the highest peak in the interest region of this plot (at approximately 300 cm^{-1}). Due to the lower bound differences, it was only really apparent on two of the spectra. This feature, because of its width, was most likely the presence of another similar phase or of bond stretching, where the structure remains but has altered dimensions due to stresses in the material. However, the disappearance and reappearance of this feature with different measurement dates seemed unlikely. Given the time available and the number of sampling points, a fuller analysis of this phenomenon was not pursued, as the primary focus of the rest of the thesis was on the AA6061 powders.

While the patterns from each individual pattern were analyzed, a comparison between the different features and the implications for the powder behavior were needed. The grouping in the lateral position of the peaks for the New powder from Supplier A was similar to the grouping of peaks from Supplier B. However, a significant difference between these powders became clear by examining the intensity: Supplier A had much lower intensities than Supplier B, across both batches. Because of the uncertainty in identifying the phase that made up this peak, whether a higher intensity or lower intensity would result in better overall behavior of the powders was unknown. If we assumed that the height difference was caused by concentrations of the relevant alumina phase(s), then the expectation would be that the total oxide content was higher for Supplier B's powder compared to either batch from Supplier A. This could be verified by comparing the intensity to the XRD or EDS results from each powder and the influence that the Raman spectra shows in terms of the oxides.

While the relative differences in the intensity and position could be found with the normal spectra data, in order to determine if there were changes in width over time a different approach was needed. As with the illustration of the shoulders on the first measurement of the New batch from Supplier A, this required normalizing each spectra with respect to the primary peak. Then, while the intensities were all equal to 1, a clearer reference for any shifting in the curves as well as their width at half their maximum were compared.

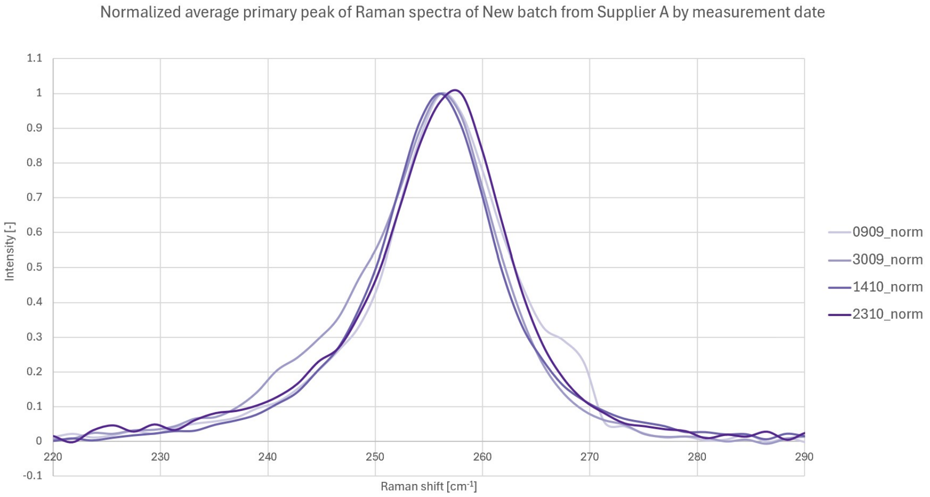

Figure 4.10: Comparison of normalized primary peaks from measurement-date averaged Raman spectra for the New batch of AA6061 powder from Supplier A, in the range 220 - 290 cm^{-1}

With the normalized peaks for the New batch from Supplier A, the influence of the shoulders widening the curves is clear, though not as significant at the half-maximum. The very small differences in the peak location again set no clear pattern with respect to the measurement dates.

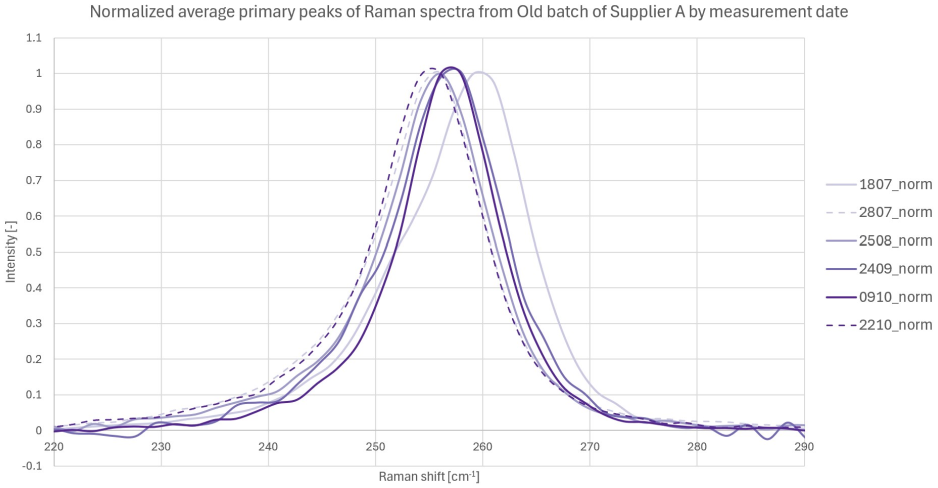

Figure 4.11: Comparison of normalized primary peaks from measurement-date averaged Raman spectra for the Old batch of AA6061 powder from Supplier A, in the range 220 - 290 cm^{-1}

With the normalized peaks for the Old batch from Supplier A, the general shift towards lower frequencies as time goes on is clearer. As mentioned previously, the difference between the first and last measurement's peak heights was 5 cm^{-1} towards the left, though the intermediate measurements varied between these two extremes in terms of the locations and how they appeared to move between measurements.

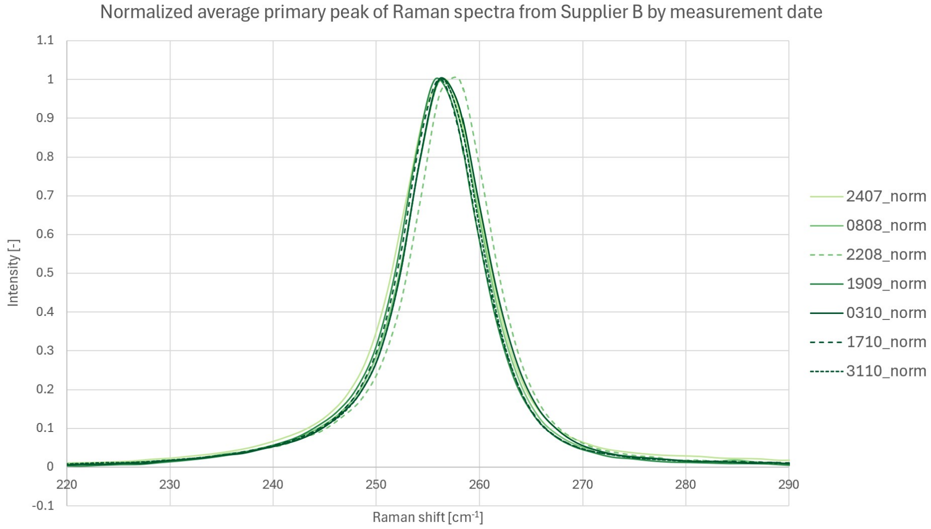

Figure 4.12: Comparison of normalized primary peaks from measurement-date averaged Raman spectra for AA6061 powder from Supplier B, in the range 220 - 290 cm^{-1}

With the normalized peaks for the powder from Supplier B, the sheer consistency in the peak locations must be emphasized. For measurements that seemed to vary wildly depending on the particular location being examined on any specific particle of any given particle batch, the peak locations for this powder varied by less than 2 cm^{-1}, which is the expected accuracy of a typical Raman spectrometer.

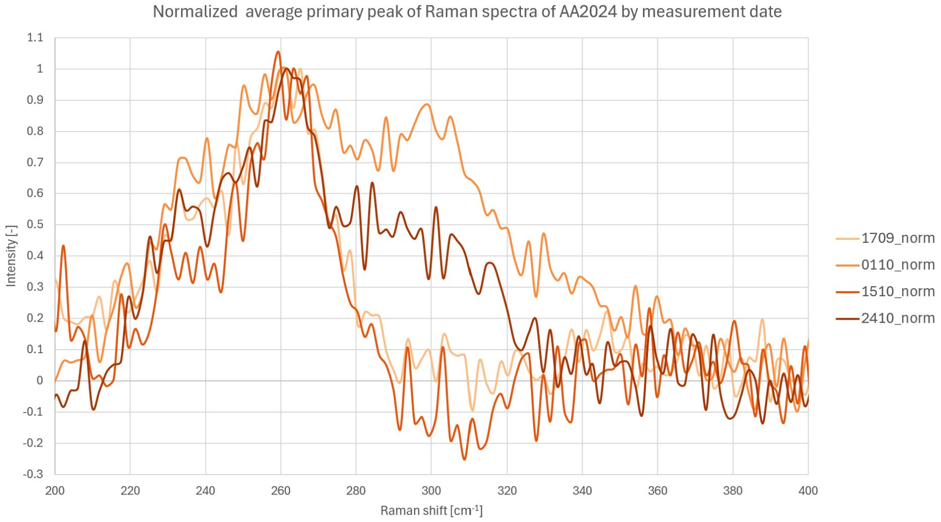

Figure 4.13: Comparison of normalized primary peaks from measurement-date averaged Raman spectra for the AA2024 powder, in the range 200 - 400 cm^{-1}

With the normalized peaks for the AA2024 powder, the same pattern occurs with two sets of two similar plots. While the maximum values of the peaks at around 261 cm^{-1} were normalized for this powder, it is rather the features around this that were observed. The first is the small plateau-looking feature around 230-240 cm^{-1}. While most apparent for the measurement on 15 October 2025, each of the spectra had this feature, which was interpreted as somewhat of a shoulder to the main peak at 261 cm^{-1}. The height of this shoulder relative to the main peaks, which were normalized, varied with passing time. For the set of measurements with 50 cm^{-1} as the lower bound, the height of the shoulder got lower after time passed. This was the same behavior exhibited by the set of measurements with 100 cm^{-1} as the lower bound.

As mentioned before, the exact phase of material oxide present in this range of frequencies was not known. The general expectation was not that any oxide concentration decreased over time, which is what the decrease in height seems to indicate for the AA2024 powder. The small sample size was likely a contributing factor in identifying this pattern and should not be considered truly representative of the powder condition.

4.1.2. XRD Results

Following the collection of data, a Rietveld refinement for each measurement was carried out. Using the in-built material library in Profex [34] and supplemented with structure information from the Materials Project [35], the composition of the powder samples was evaluated over time.

The phases and compounds included in the refinement influenced the composition results, so identifying those most likely to be present was important for the rest of the analysis. This was done with a combination of literature search and trial and error to highlight the constituents that most closely replicated the manufacturer-tested composition [38–40]. This was used as a verification that the correct phases were being associated with the measured spectra.

The diffraction peaks of each phase and compound were matched to the recorded peaks in the measurement. The recorded test data was presented in a plot like in Figure 4.14.

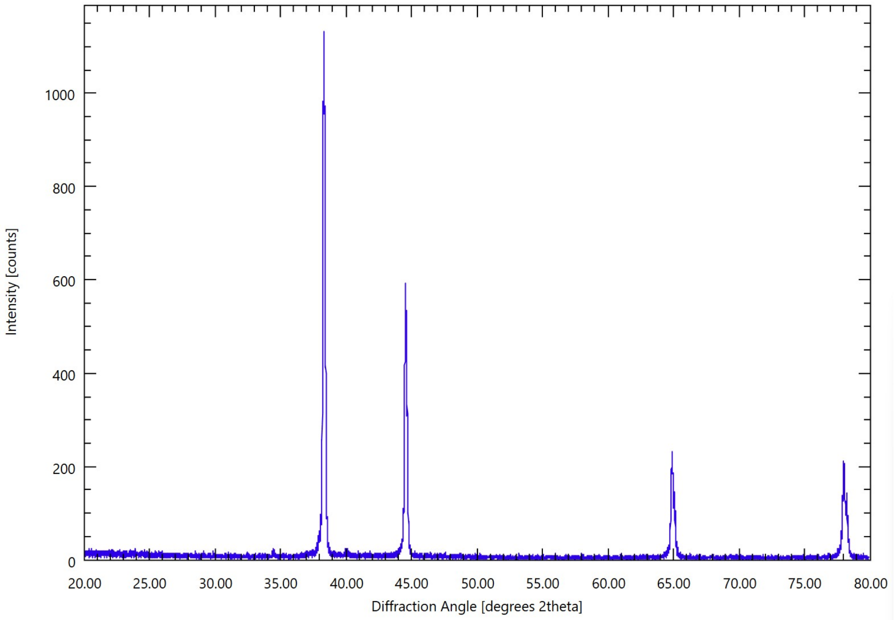

Figure 4.14: Diffraction peaks of the New batch of AA6061 from Supplier A measured on 3 October 2025

The main peaks were dominated by the aluminum contributions, and were consistent in location between the AA6061 and AA2024 results. Curiously, because of the overlap of two peaks between the iron and aluminum diffraction spectra, some of the refinements ascribed a much higher portion of the composition to iron than was logical. However, because this is an overlap of iron with the aluminum peaks, and not of any of the alumina's or other phases, this was considered to be a quirk but not negatively impacting the results or analysis thereof. The over-reporting of iron and associated under-reporting of aluminum is shown in the results from the New and Old powders from Supplier A (Tables 4.1 and 4.2), as well as that for the AA2024 powder (Table 4.4). The collected data was measured over a region of the powder sample, and relates more of the bulk material details compared to Raman spectroscopy, which is more surface-sensitive.

Table 4.1: XRD composition of New batch of AA6061 powder from Supplier A, in weight %, for each measurement date compared to the nominal composition tested by the manufacturer

Element	5 September 2025	3 October 2025	17 October 2025	31 October 2025	Nominal
O	1.40	1.25	1.31	1.45	-
Mg	0.91	0.58	0.62	0.84	0.85
Al	88.49	85.49	97.00	96.37	Balance
Si	0.53	0.44	0.42	0.55	0.59
Ti	0.04	0.07	0.03	0.04	0.10
Cr	0.13	0.10	0.15	0.14	-
Mn	0.10	0.26	0.23	0.13	-
Fe	8.09	11.61	0.00	0.18	0.15
Cu	0.15	0.21	0.25	0.29	0.28
Zn	0.08	0.00	0.00	0.00	0.09

The first two measurements of the New batch from Supplier A and their refinements had the over-reporting of iron and under-reporting of aluminum compositions. No apparent pattern in the oxygen composition was found, other than relatively small variations in the detected oxygen between measurement dates. Also, despite having fluctuating values for the compositions of the other elements (especially Mg, a majority alloying element), it was not that some elements were disappearing or reappearing in different concentrations. Because some oxides containing elements other than aluminum were included in the refinement, some of the variation could be related to that. The other possible explanation was altering crystallinity resulting in lower or higher crystalline compositions without truly changing the actual elemental composition. Because XRD is only sensitive to crystal structures, if some of these were to disappear in favor of disordered amorphous structures, the detected concentration could reduce.

Table 4.2: XRD composition of Old batch of AA6061 powder from Supplier A, in weight %, for each measurement date compared to the nominal composition tested by the manufacturer

Element	19 August 2025	16 September 2025	1 October 2025	14 October 2025	23 October 2025	Nominal
O	1.75	1.08	1.35	1.52	1.40	-
Mg	0.80	0.86	0.69	0.76	0.83	0.90
Al	84.43	96.52	96.65	95.98	96.32	Balance
Si	0.57	0.50	0.40	0.61	0.60	0.55
Ti	0.00	0.09	0.00	0.08	0.00	0.11
Cr	0.13	0.13	0.07	0.20	0.11	-
Mn	0.27	0.28	0.08	0.17	0.22	-
Fe	11.79	0.43	0.38	0.27	0.32	0.12
Cu	0.22	0.12	0.38	0.20	0.19	0.24
Zn	0.04	0.00	0.00	0.00	0.03	0.06

The first measurement of the Old batch from Supplier A showed the influence of the iron-aluminum mis-identification. The oxygen content varied more significantly between measurements than it did for the New batch, however because of this variation no clear pattern was visible. In opposition to that of the New batch, the magnesium content varied less between measurements, and remained closer to the expected values. However, as mentioned previously, this was likely not due to any changes in the amount of each element present but rather its crystallinity or crystalline oxide concentrations.

Table 4.3: XRD composition of AA6061 powder from Supplier B, in weight %, for each measurement date compared to the nominal composition in literature

Element	17 September 2025	1 October 2025	15 October 2025	24 October 2025	Nominal
O	1.75	1.33	1.5	1.48	-
Mg	0.79	0.92	0.84	0.98	0.80-1.20
Al	95.73	96.36	96.51	96.00	Balance
Si	0.49	0.58	0.54	0.64	0.40-0.80
Ti	0.13	0.03	0.12	0.00	<0.15
Cr	0.12	0.13	0.05	0.10	0.04-0.35
Mn	0.25	0.10	0.25	0.18	<0.15
Fe	0.41	0.30	0.00	0.29	<0.70
Cu	0.30	0.25	0.18	0.31	0.15-0.40
Zn	0.00	0.00	0.01	0.02	<0.25

The powder from Supplier B was the only one for which the software did not ascribe aluminum signals to iron, so the iron composition was much more in line with the expected values. As with that of the New batch from Supplier A, the oxygen composition varied significantly between measurements. The magnesium composition fell entirely within the expected range, with the exception of the first measurement, which was only 0.01 % below the specification for the alloy. Other than for the oxygen concentration, the calculated composition appeared more consistent for this powder compared to the others. This was with the exception of the iron composition. There was no iron found in the spectrum on October 15 when the aluminum reported was the highest of any of the measurements. It is possible that the overlap in the peak locations contributed in the opposite manner as seen in the other powders, and over-reported aluminum to the detriment of iron.

Table 4.4: XRD composition of AA2024 powder, in weight %, for each measurement date compared to the nominal composition in literature

Element	16 September 2025	1 October 2025	14 October 2025	23 October 2025	Nominal
O	3.21	2.85	2.70	2.30	-
Mg	0.78	0.82	0.69	0.51	1.20-1.80
Al	91.17	91.48	81.03	93.17	Balance
Si	0.24	0.16	0.35	0.12	<0.50
Ti	0.29	0.25	0.23	0.36	<0.15
Cr	0.09	0.00	0.22	0.12	<0.10
Mn	0.43	0.55	0.19	0.32	0.30-0.90
Fe	0.00	0.00	11.25	0.12	<0.50
Cu	3.77	3.84	3.35	2.91	3.80-4.90
Zn	0.01	0.06	0.00	0.00	<.25

A very visible difference between the AA6061 and AA2024 powders became clear based on the composition of the AA2024 powder. The overall oxygen content was much higher, and in fact nearly double the oxygen composition compared to the AA6061 powders. Also, a definitive pattern in the oxygen content was identified: a decrease over time. The expectation would not be for oxygen to decrease, but rather to increase as time passed or with prolonged exposure to oxidizing conditions. Since XRD is sensitive to crystalline arrangements, and does not detect amorphous, less ordered structures, the likely cause for the decrease in crystalline oxides was their conversion to amorphous structures.

Combining the results from the measurements, the oxygen concentrations were compared between the different powders. The results of this, plotted against the measurement date, are shown in Figure 4.15.

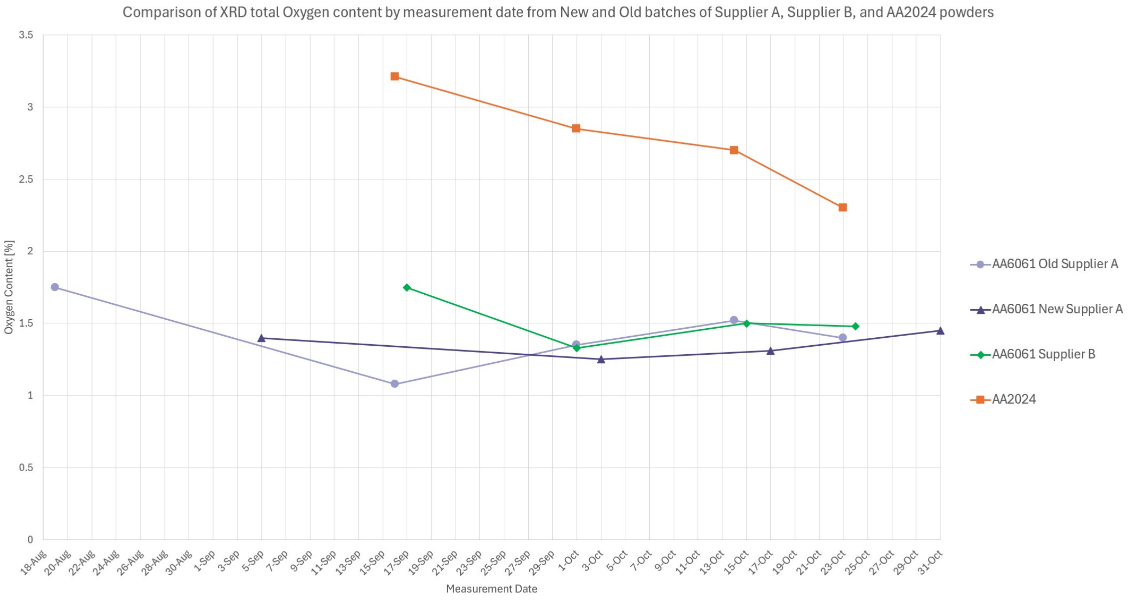

Figure 4.15: Comparison of XRD-measured oxygen content between the three AA6061 and AA2024 powders by measurement date

As was mentioned above in regards to the overall compositions, the only powder with any consistent pattern in the oxygen content was the AA2024 powder. The oxygen contents were also plotted against the number of days since the powder container had been opened. This allowed for a fuller examination of the age-related influence on any patterns in the measurements. This is shown in Figure 4.16.

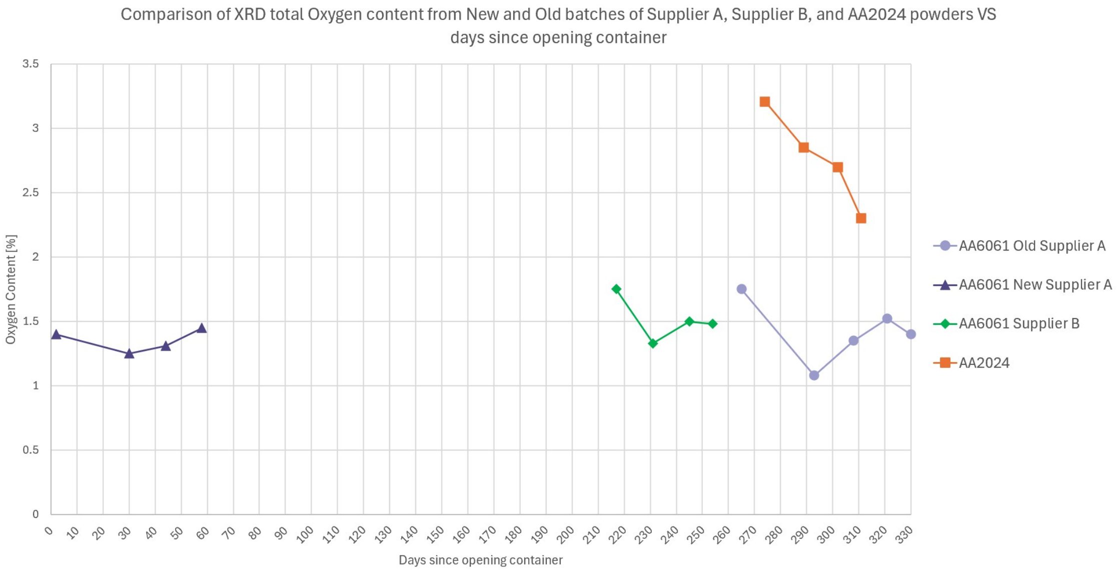

Figure 4.16: Comparison of XRD-measured oxygen content between the three AA6061 and AA2024 powders by days since opening the container

While the container for the AA2024 was opened at a similar time as that for the Old batch from Supplier A, the reality in terms of the overall powder age is different. The AA2024 powder was in storage for over a year before being shipped and then opened in December 2024. So, whatever influence the production process, packaging conditions, and storage conditions had on this powder, while not measured, would be impacting the results. This was likely the cause for two things: the first being the inability to spray this powder after a certain time had passed and the second being the much higher oxygen content measured in the XRD testing. Since the production date for this powder was not known, the total time between production and use could not be calculated to include the influence of much longer stretches of time and potential exposure to oxidation in the analysis. The priority for the analysis, as with the Raman spectroscopy, then fell to the three AA6061 powders since more was known about their condition.

In addition to the overall oxygen content calculated, an analysis of the various aluminum oxides and their concentration between measurements was performed. In total there were seven forms of aluminum oxide included in the refinement: $\alpha - Al_2O_3$, $\delta - m - Al_2O_3$, $\delta - o - Al_2O_3$, $\gamma - Al_2O_3$, $\gamma' - Al_2O_3$, $\kappa - Al_2O_3$, and $\theta - Al_2O_3$. With the exception of $\alpha - Al_2O_3$, which is a stable phase, all the other phases are meta-stable. Plots of the concentrations of these aluminum oxides are shown in Figures 4.17, 4.18, 4.19, and 4.20.

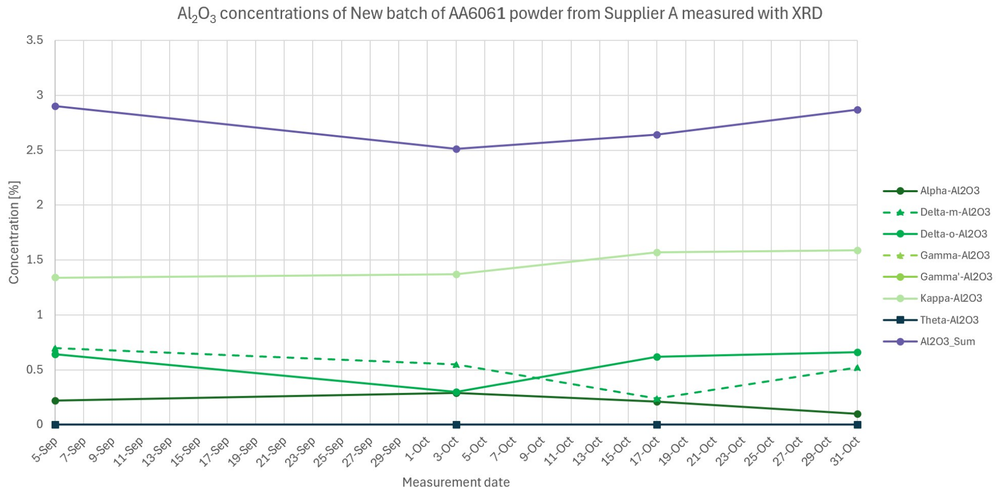

Figure 4.17: Concentration of Al_2O_3 forms present in XRD refinement of the New batch of AA6061 powder from Supplier A by measurement date, with the sum of all contributions also plotted

The summed contribution of the different forms of Al_2O_3 of the New batch from Supplier A mimicked the shape of the overall detected oxygen shown by this powder in Figure 4.15. However, the values resulting from the summed contributions of the forms of Al_2O_3 are almost exactly twice the reported oxygen content for each point. This was also the case for the other powders. Of course, the calculated oxygen content did not only include contributions from the aluminum oxides, but it is the factor of 2 between these results that was interesting. An expectation for the concentration of any aluminum oxide to be translated into pure oxygen content would include the contribution of the 3 subscript in the compound's formula Al_2O_3. While this was an oddity, because it was consistent between the powders, no need for further analysis was found.

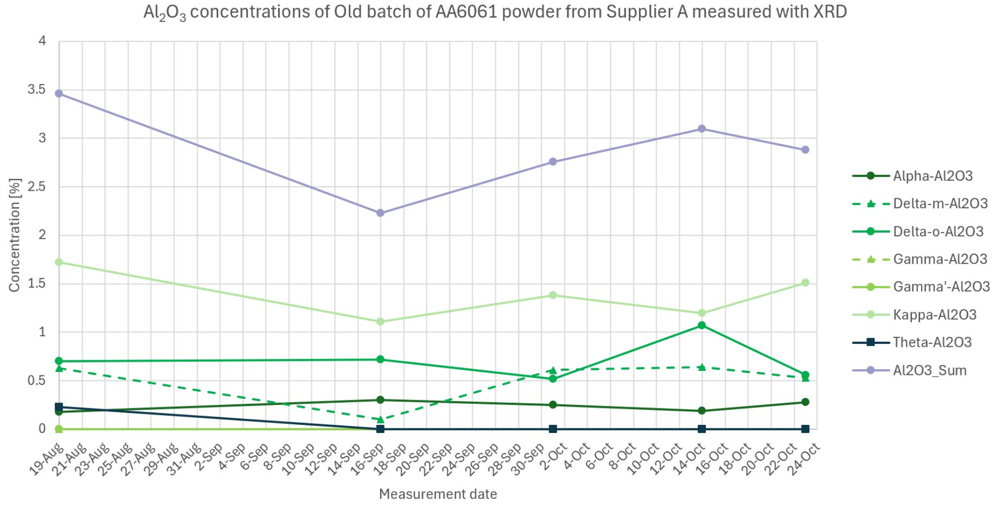

Figure 4.18: Concentration of Al_2O_3 forms present in XRD refinement of the Old batch of AA6061 powder from Supplier A by measurement date, with the sum of all contributions also plotted

As with the New batch, the Old batch from Supplier A had a summed concentration of aluminum oxide that mimicked the overall oxygen contents detected for this powder. Again, the factor of 2 offset between the values was interesting, but not pressing for the analysis.

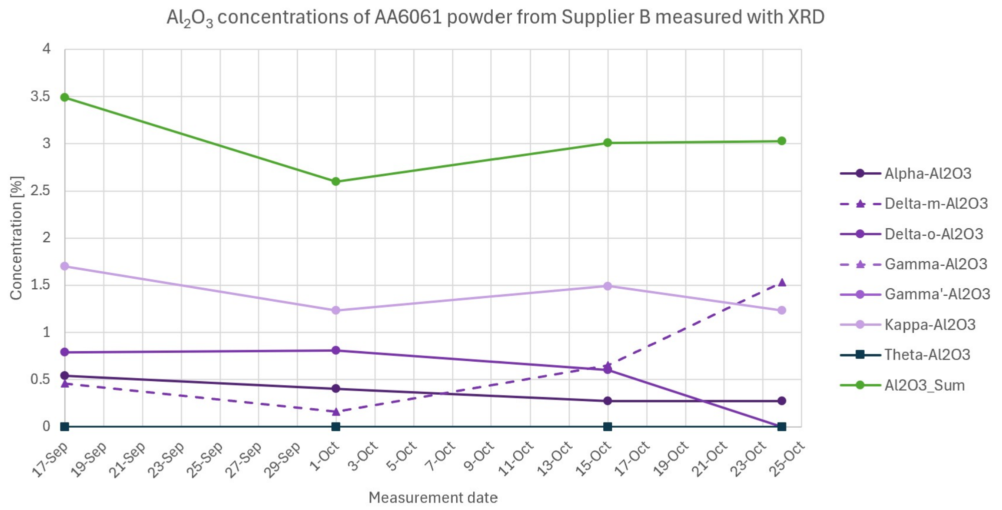

Figure 4.19: Concentration of Al_2O_3 forms present in XRD refinement of AA6061 powder from Supplier B by measurement date, with the sum of all contributions also plotted

Because of the contributions of the $\kappa - Al_2O_3$ towards the sum, and the relatively more consistent concentrations of the other aluminum oxide forms, the pattern of the $\kappa - Al_2O_3$ and the sum was the same in Supplier B's powder. Here, the two $\delta-$ forms seemed more consistent, although their difference from the third to the fourth measurement was not consistent with the trend.

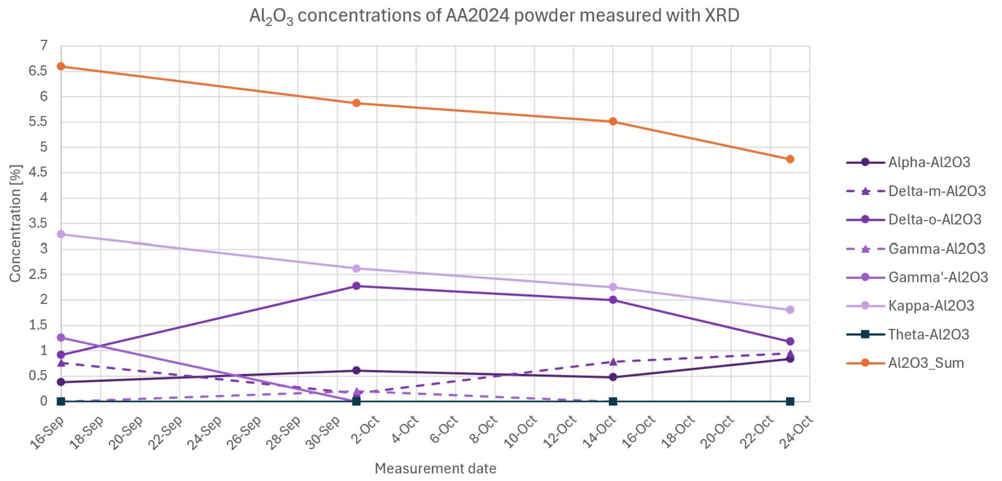

Figure 4.20: Concentration of Al_2O_3 forms present in XRD refinement of the AA2024 powder by measurement date, with the sum of all contributions also plotted

As with the powder from Supplier B, the AA2024 powder had the same shape for both the $\kappa - Al_2O_3$ and summed concentrations. The difference between the $\kappa - Al_2O_3$ and the $\alpha - Al_2O_3$ was greater than for the other powders, with the $\kappa - Al_2O_3$ also having a higher overall value. Because of the overall higher oxygen content from this powder, this was expected. However, considering that the $\alpha - Al_2O_3$ contents were similar to those of the other powders, the net ratio of $\alpha - Al_2O_3$ was lower. The effect this would have on the powder performance is not known, but as $\alpha - Al_2O_3$ is the most stable form of aluminum oxide, it would not be likely to shift to another form.

What was also clear for each of the powders was the contribution of $\kappa - Al_2O_3$ was the greatest, with $\alpha - Al_2O_3$ having fairly consistent, but much lower concentrations. The two forms $\delta - m - Al_2O_3$ and $\delta - o - Al_2O_3$ seemed to have inverse behavior of each other; an increase in one between measurements was seen alongside a decrease in the other or vice versa. Given that these are specifically two different structural arrangements for the same δ phase of the oxide, it makes sense that their behaviors are paired [47].

4.1.3. SEM-EDS Results

The SEM images taken showed the relative size and shape of the particles, though likely some bias resulted from the sampling method (scooping a portion of powder onto the carbon tape and using compressed air to blow off excess). Due to the dispersion of the particles across the carbon tapes, and its irregularity, a full particle size analysis (with each measurement iteration) was not possible. While each of the powders were sieved by the manufacturer prior to being shipped, some particles were larger than the filter size (75 μm). Each powder batch had examples of these large particles. The general indications were that the powders are fairly round, but not perfectly spherical, with a relatively high concentration of satellites attached to many of the particles. An image taken at 100x magnification for each of the powders is presented in Figure 4.21 as an indication of the powder shapes and (ir)regularity. This also demonstrates the difficulty in attaining uniform distribution of the powders over the carbon tapes for examination of the sizes, and several particles appear to rest at angles on top of others.

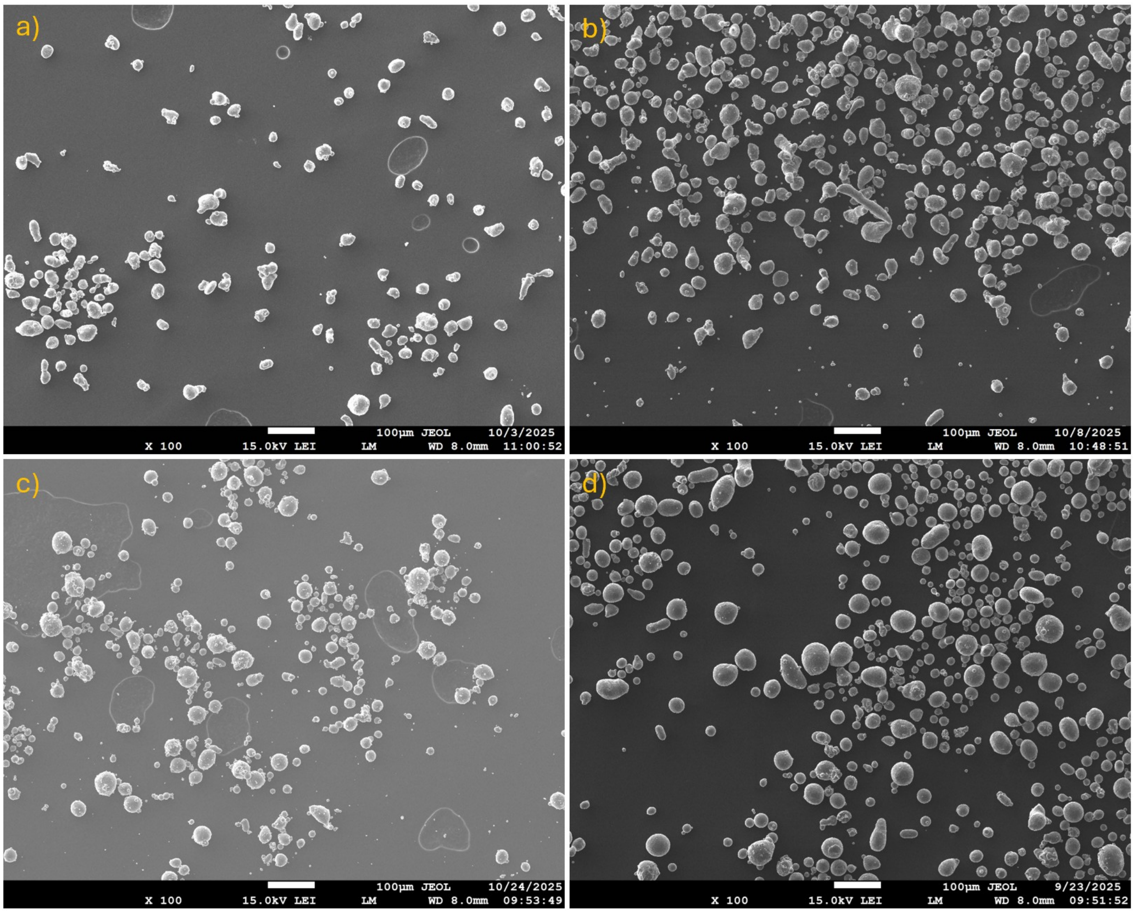

Figure 4.21: SEM images taken at 100x on LMLEI mode of: a) Old batch AA6061 from Supplier A, b) New batch AA6061 from Supplier A, c) AA6061 from Supplier B, and d) the ”un-sprayable” AA2024

The satellites were apparent on each of the powders at every time interval, though some regions had particularly high densities. This was likely due to the powder manufacturing method of gas atomization. This is known to produce flow within the catch chamber that can lift small particles back into the path of the freshly atomized larger particles and encourage merging. Based on appearances, some of the satellites appeared to have partially melted or otherwise bonded into place on the larger particles. Other collections of particles seem to have satellites stuck in irregular surface features of larger particles.

This behavior could be exacerbated or reduced depending on the storage conditions or agitation of the powder, though it was an observation only as it could not be quantified. An example of high satellite concentrations is shown in Figure 4.22, where each of the particles in the lower magnification image have several satellites.

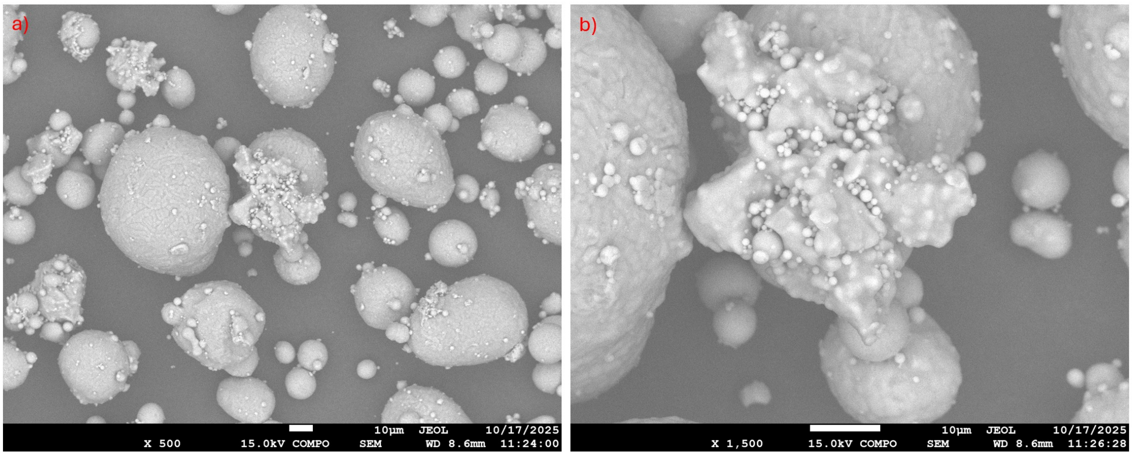

Figure 4.22: Different magnifications of AA6061 powder from Supplier B showing a high density of satellites at a) 500x magnification and b) 1500x magnification in SEM-COMPO mode

Also present in some of the images were very strangely shaped particles, or large clusters of satellites and oddly flowing surface material. By sheer chance, these were caught and imaged on some of the powders. Below is an image (Figure 4.23) with what looks like a cat on the surface of an AA2024 particle imaged on 23 September 2025.

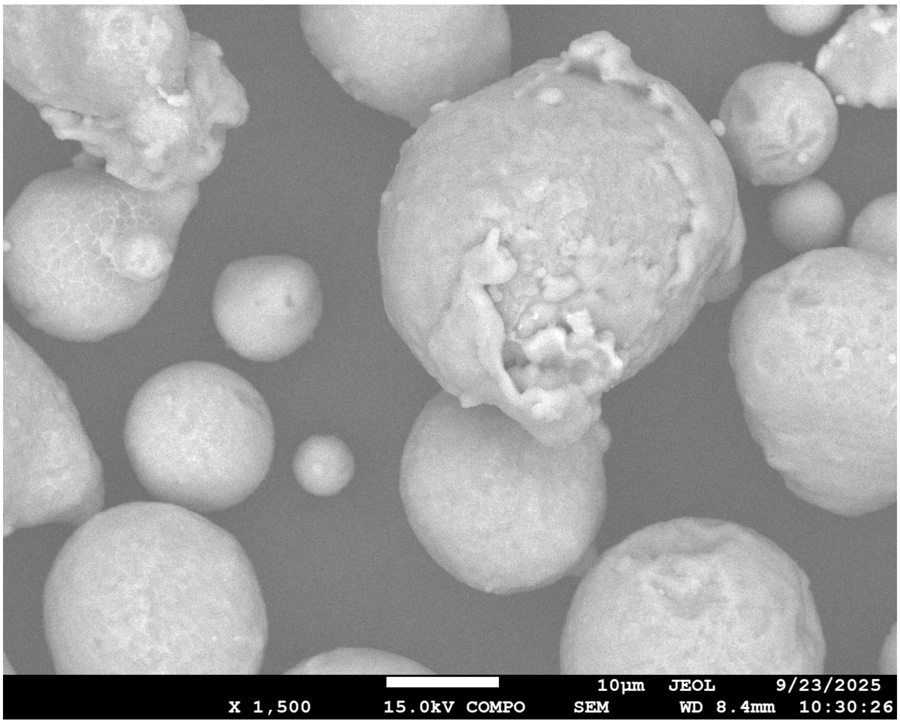

Figure 4.23: SEM image of AA2024 particle with cat-shaped surface formation

Generally, the grains on the individual particles were visible with each imaging mode. While they were not measured, they were typically several microns in size and there was not much irregularity in terms of grain size in any given region of the particle. However, some areas where this did not hold true were because of a completely different surface appearance of the particle. Rather than having the pattern of the grains visible, or some kind of indication towards nano-scale surface profile differences, some particles instead had monolithic smooth sections with few defining features. Examples of these are shown in Figures 4.24 and 4.25.

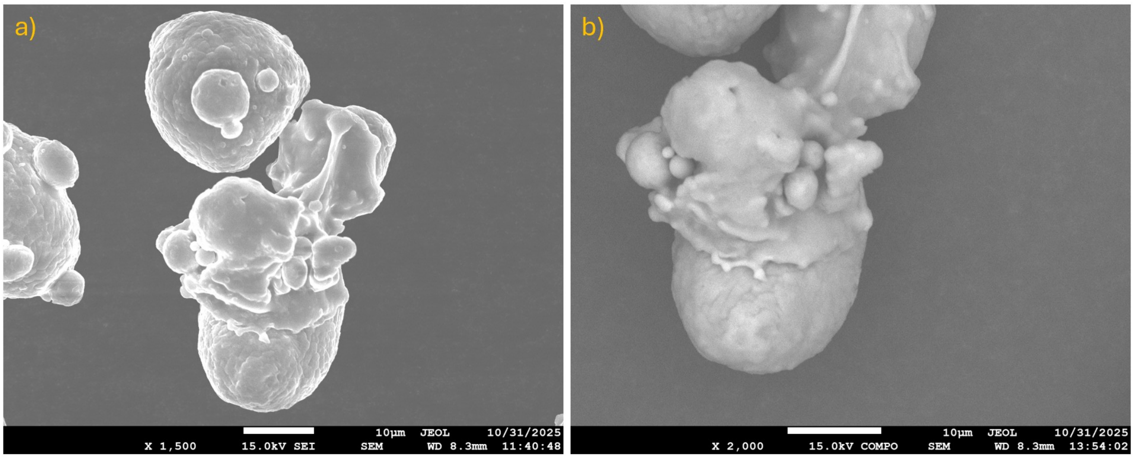

Figure 4.24: a) Particle from Old batch of Supplier A with flow-like smoothened surfaces imaged with SEM LEI at 1500x, and b) The same particle and flow feature, focused on the lower portion and the formation of the smooth surface at the interface with the more normal particle surface imaged with SEM COMPO mode at 2000x

While the surface of the particle in Figure 4.24 is not featureless, there is a clear demarcation between the typical grain-structure and the flowing surface. Towards the bottom of Figure 4.24b, there are portions of the flowing surface that appear to have jetted, as there is what looks like a wave front on top of the more rounded, grain-boundary-exhibiting particle underneath. Given that these particles only experienced full melting during the original gas-atomization production process, these melt-like features were unexpected in the unaltered supplied powder.

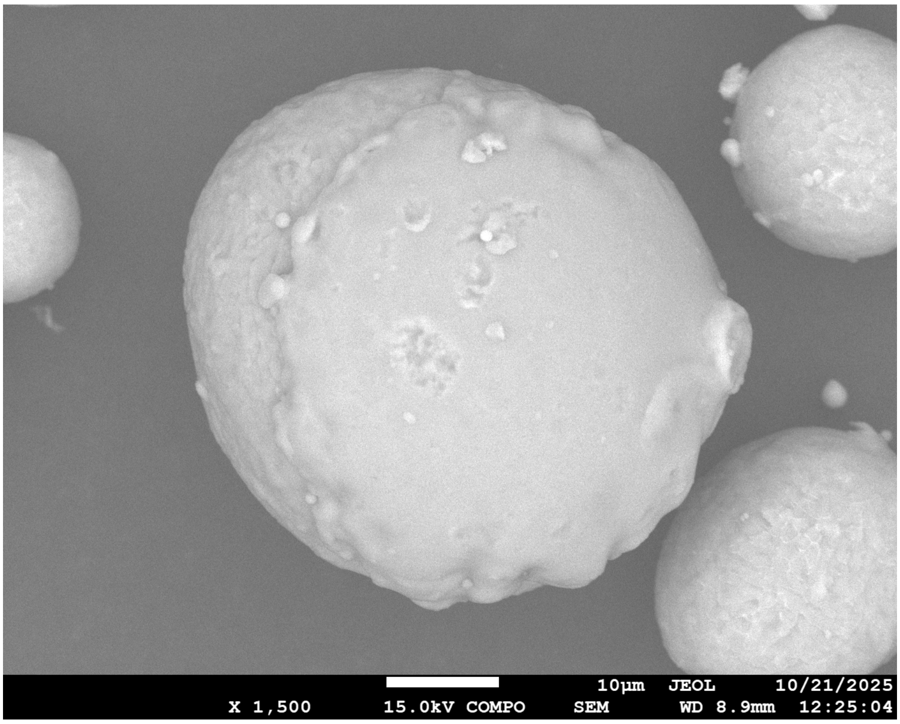

Figure 4.25: Particle from the AA2024 powder with a smooth surface layer on top of and covering the expected grain structure

The particle shown in Figure 4.25 has a more regular shape, and the majority of the imaged surface is covered by the flow-like smooth surface. The grained structure is clear on the left portion of the particle, as well as being visible on the particles surrounding it. Similar to the features in Figure 4.24, the edge of the smooth surface has a wave-like boundary between the two surfaces. These features were presumed to result from the atomization process and irregular cooling rates yielding these different surface structures.

Following the collection of SEM images on a given measurement date, regions of interest were also investigated with EDS to determine the composition across particles and as a comparison point between different powders and measurement dates. Both area maps and point identification were used to quantify the composition and oxygen content of the particles and regions of interest.

Outliers from the mapped oxygen concentration included those from the new batch from Supplier A taken on 20 October and 3 November 2025 as well as from Supplier B on 17 October and 24 October 2025. These were considered outliers because the mapped regions included significant areas of the carbon tapes. An example is shown in Figure 4.26 with a mapped region including several particles from Supplier B and the carbon tape that they were stuck to. As is clear from the overlap between the carbon and oxygen element maps, the C-O bonding, when visible, results in a higher overall oxygen density than is present on the particles themselves.

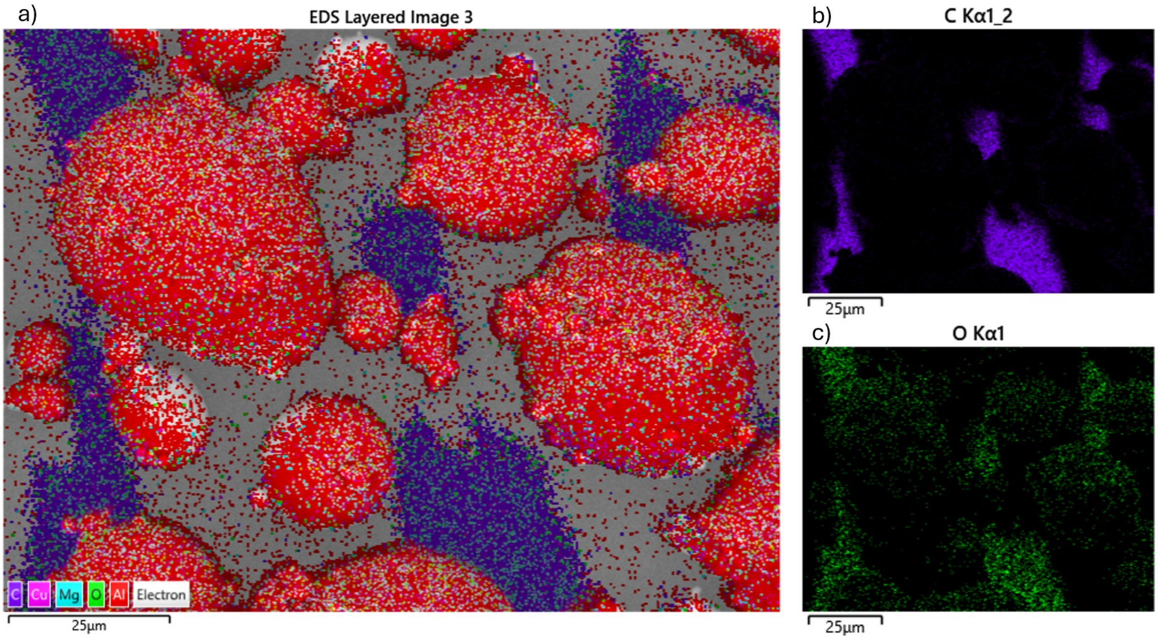

Figure 4.26: a) Mapped composition of particles from Supplier B measured on 17 October 2025 with carbon tape visible on the background, b) Carbon map of the same image, and c) Oxygen map of the same image shows overlap between carbon signals and stronger oxygen signals, as well as oxygen concentrations on the particles themselves, indicating a higher overall oxygen content than is accurate for the powder

From the collected data, the mapped and point-identified oxygen content of the powders over time are plotted in Figure 4.27. This data included several relevant outliers in the mapped concentrations, which were removed based on the above justification.

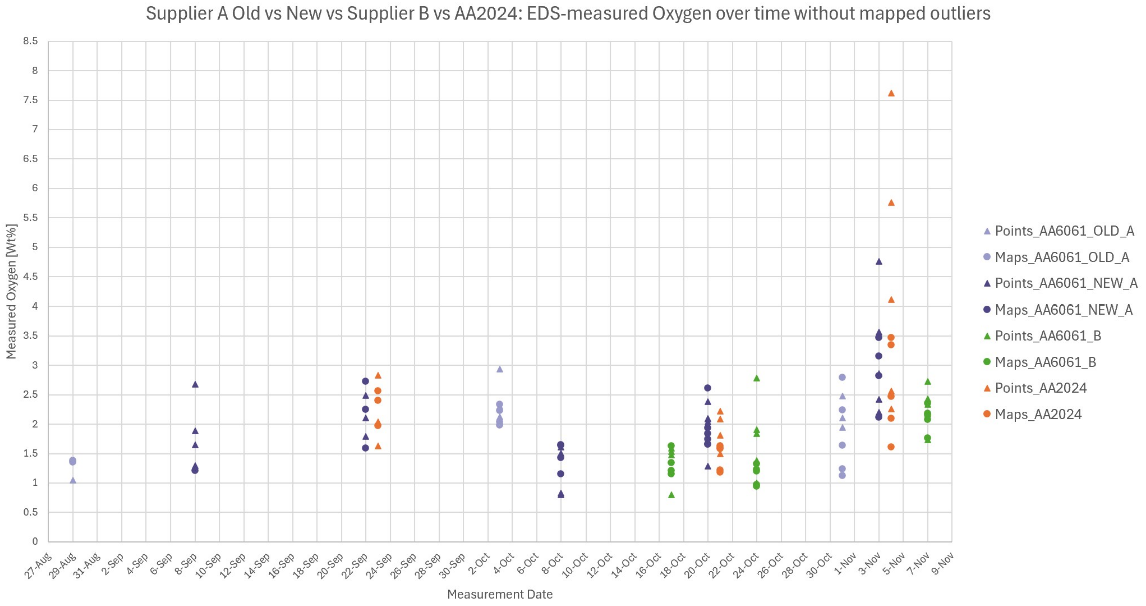

Figure 4.27: EDS-measured oxygen content of the three AA6061 and AA2024 powders by measurement date, without mapped outliers.

On first inspection, the trend in the oxygen content is generally upwards. However, several of the measurement dates featured an apparent drop in oxygen content from the previous measurement. The large scatter in the collected data did not aid the analysis, and some steps were taken to reduce the effect. This started with identifying which points were outliers due to their measurement type. As was clear from the large spread in data points, there was a large amount of scatter in the measurements, even those taking place on the same day.

Following the removal of outliers, the measurement dates were converted into day-counts. These more accurately represented the ”age” of the powder in terms of opening the original powder containers and how their condition evolved over time. The same information as before was thus plotted against the total days since the original powder container was opened and this is shown in Figure 4.28.

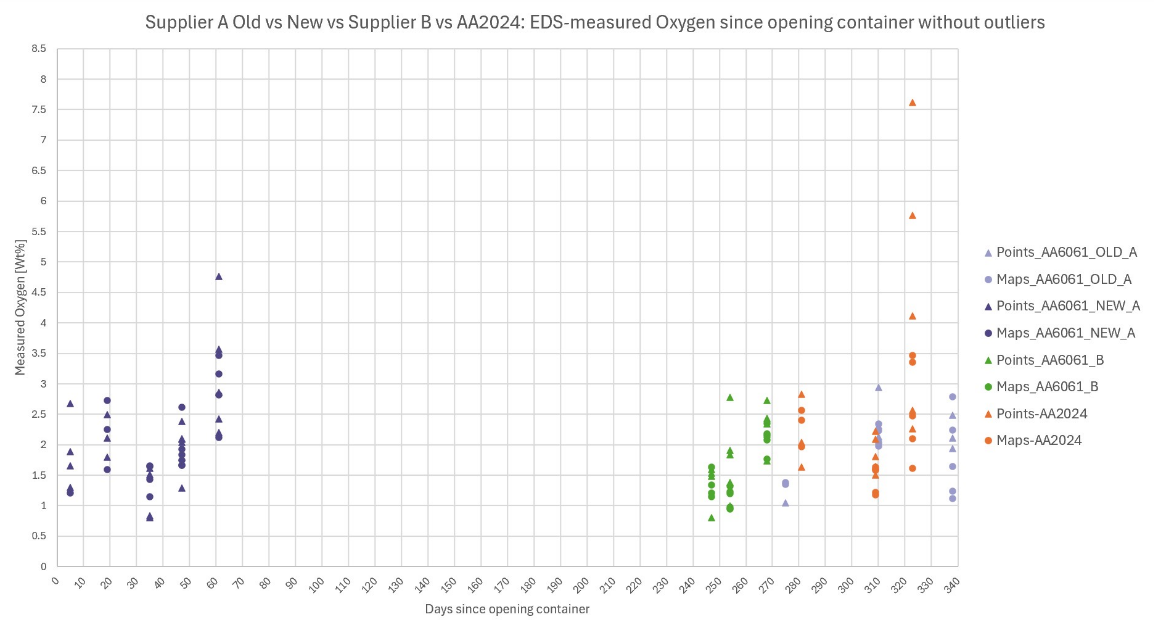

Figure 4.28: EDS-measured oxygen content of the three AA6061 and AA2024 powders versus days since the containers were opened, without mapped outliers.

Only the powder from Supplier B had a consistently upward trend in the oxygen concentration. As was noted before, some measurements seemed to increase and decrease again, though there is considerable scatter in the measurement points, and only a few measurement sets in the time frame. As noted before, the true effective age of the AA2024 powder is much older than the other powders, though because the container was opened at a similar time to the Old batch from Supplier A they appear near each other on this plot. Attempts to fit trend lines resulted in polynomial fits with the best approximation of the measured behavior, but this could not be taken as the real pattern, given the small number of measurements.

The next step in the analysis was to determine how significant any of these patterns truly were, and whether random variation or a true alteration in behavior were to blame for irregularities and large scatter. To accomplish this, the various mapped and point-identified measurements from each day were combined to get average values for the two methods along with standard deviations of the included data points. The resulting plot is shown in Figure 4.29.

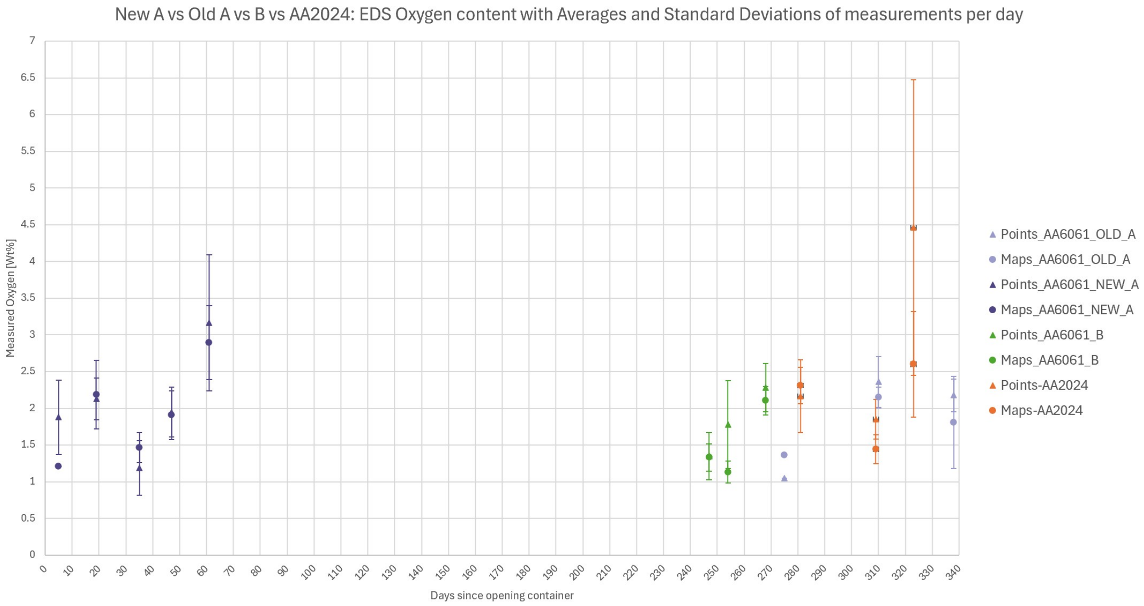

Figure 4.29: Average EDS-measured oxygen content of the three AA6061 and AA2024 powders on the basis of point identification and mapping, without outliers, and including the standard deviations as the error bars

With this adjustment, similar patterns remained visible. For Supplier A's New powder the mapped and point-ID concentrations both followed the same increasing, decreasing, and increasing pattern. Supplier A's Old powder saw an increase and then only a decrease for both mapping and point-ID. It is with Supplier B's powder that a difference is seen between the plots in Figures 4.28 and 4.29. Here, while the point-ID concentration of oxygen followed the same consistently upward trend identified previously, the mapped content did not keep the same pattern. The mapped concentrations reduced after the first measurement point, then increased significantly at the third. Of course, any patterns identified between what are essentially three measurement points are not likely to be as clear and significant as those with more information. It is possible that this analysis attributed meaning and pattern to random variation, even simply between the evaluated particles on a single measurement date.

One last adjustment was made to the total concentration plot. As each point-ID was based on a mapped region from the same measurement date, one could expect that the measured content would be reflected in the other measurements of the same site. Because of the relatively homogeneous distribution of the various alloying elements through the powder, as seen in the mapped concentrations, there was possibility of finding regions of higher or lower concentrations with point-ID than the map indicated. If a point that coincided with a point from a specific element map was selected, there would be a higher concentration of that element detected in the point-ID. This led to the offsets in the mapped and point-ID concentrations, despite examining identical portions of the same particles for a given measurement.

What was interesting was that there was not true consistency whether the point-ID or the mapped concentration yielded a higher oxygen content amongst all the powders and on each measurement day. As this was based on an average across multiple measurements on any given date, this was expected. A similar pattern existed for the mapped and point-ID information plotted with each instance being represented, rather than an average across several (Figure 4.28).

Given that no clear offset remained consistent for any of the powders or measurement dates, all the information was also collected into single points per day. This included all the mapped and point-ID data for that day counting towards a calculated average and the standard deviation. The results of this final adjustment are shown in Figure 4.30.

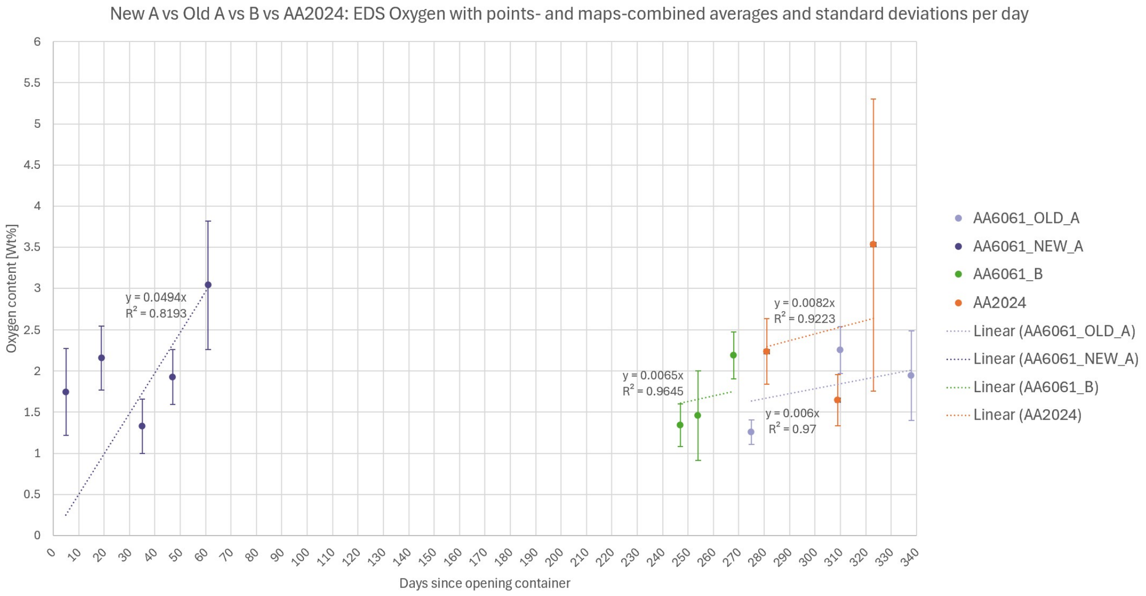

Figure 4.30: Linear trendlines with equations and fits for averaged combined map and point-ID oxygen content measurements with standard deviations as error bars versus the number of days since opening the powder container

The standard deviations were included as the error bars, and the linear regression best-linear-fit was set to intercept at the origin. Though there would likely never be zero oxygen inside the container or on a particle surface, any other intercept allowed for negative oxygen which is physically impossible. Knowing that the oxide growth is not linear, but often logarithmic, these trends do not reflect the real-world behavior of the oxides. They do represent, however, the visual trend in the collected data resulting in higher oxygen contents with the passage of time.

The general upwards trend in the oxygen content over time was expected, but what was especially interesting were the differences between the powders. The Old batch from Supplier A and the batch from Supplier B had fairly similar ages, in terms of when their containers were originally opened compared to the testing schedule. Despite being produced by different manufacturers, the slopes of their best fits are very similar. The slope of the fit for the AA2024 is also very similar to these two powders, however with an upwards offset due likely to the advanced age of this powder overall (recall that it was stored for at least a year prior to being shipped and opened). The high scatter from the point-ID data carried over into the collected data, possibly contributing to a better fitting line that does not represent the actual situation.

The New batch from Supplier A, on the other hand, has a much steeper slope to the linear fit. This powder was opened much closer to the time of testing. While this is effectively ”one” data point for a new powder’s behavior from a freshly opened container, it was interesting to observe how aggressive the oxidation appeared to be in this early stage, based on this collection of data. Again, though the linear trends were applied, they do not match the true oxide growth behavior. A more rapid growth of the oxide in the earlier stages of exposure is expected, and then a gradual reduction in the growth rate as time passes until it reaches more of a steady-state. Whether this point was reached during the research intervals for the freshly opened powder from Supplier A is not known due to lack of further data.

4.2. LASHPOL Results

Of the 51 receivers used, 25 were kept for observation after the experiments. The goal of the testing was to examine the number (and launch conditions) of splats, which are particles with sufficient velocity to adhere to the substrate pieces. Some of the receivers were kept because the imaging during the shock indicated a splatted particle. Other receivers were kept because imaging failed and there was the possibility of a splat.

Based on the images, while some samples did not have save files due to illumination or camera faults, there were a specified number of splats identified for each of the iterations. An overview of the results of each iteration follows in Tables 4.5, 4.6, 4.7, and 4.8 below. Here the following information is presented: the measured size of the launched particle, how many frames it was present in the images, whether the particle was a splat or a rebound, the determined velocity (based on the frame rate, calibrated pixel/mm measurement, and pixel locations), and whether the receiver was kept or discarded after the experiment.

Unfortunately, the laser power was not recorded during the first iteration of experiments. The laser power was recorded for each experiment in the following three iterations.

Table 4.5: Iteration 1 LASHPOL results, using New batch of AA6061 powder from Supplier A

Index	Particle Major Axis $[\mu m]$	Particle Minor Axis $[\mu m]$	Frames	Result	Average Velocity $[m/s]$	Max. Velocity $[m/s]$	Kept
A01	33.47	20.01	0				No
A02	48.71	38.14	7	Rebound	306.594	589.116	Yes
A03	41.72	23.89	5	Rebound	494.097	652.462	Yes
A04	60.68	54.10	0				No
A05	55.70	32.62	5	Splat	620.789	646.127	Yes
A06	42.61	27.74	7	Rebound	341.012	557.443	No
A07	63.01	41.64	6	Unclear	443.997	690.469	Yes
A08	39.64	37.07	6	Rebound	391.477	405.413	No
A09	46.77	35.21	4	Rebound	701.027	728.477	Yes
A10	57.64	32.94	3	Rebounds	745.897	798.157	No
A11	50.64	28.30	4	Rebound	679.912	709.473	No
A12	38.64	18.15	6	Rebound	430.752	456.090	Yes
A13	64.93	54.20	0				Yes
A14	51.84	26.27	5	Rebound	509.934	525.770	No
A15	50.97	22.74	3	Rebound	794.990	810.827	Yes
A16	29.65	25.65	1				No
A17	38.56	24.46	5	Rebounds	419.983	487.763	No
A18	36.56	19.26	3	Rebound	772.819	791.823	No

The first iteration was done without any heating, as the setup required more time and arrangement. However, given the small number of splats (as determined based on the images captured during the launches), the decision was made to add heating for the next iteration. This particle and substrate heating was expected to improve the likelihood of adhesion. As mentioned in the methodology, the particle heating was accomplished with an infrared source and the substrate used a bar heating element and thermocouple for monitoring. Due to the control method and heating element type, the particle heating was more consistent than the substrate heating. For the experiments with heating elements, the particle was heated to 110 °C immediately before the launch, while the substrate temperature varied. Since the particle temperature remained consistent, only the substrate temperature is tabulated for the following experiments.

Table 4.6: Iteration 2 LASHPOL results, using New batch of AA6061 powder from Supplier A. Particle on HA08 was suspected to be missing after the launcher was dropped in transit and was not launched.

Index	Particle Major Axis $[\mu m]$	Particle Minor Axis $[\mu m]$	Frames	Substrate heating [°C]	Laser Power [mJ]	Result	Average Velocity $[m/s]$	Max. Velocity $[m/s]$	Kept
HA01	51.73	41.61	5	84.7	1348.22	Rebound	380.075	386.410	Yes
HA02	32.54	30.11	2	128.6	1624.54	Rebound	728.477	728.477	Yes
HA03	63.63	30.52	0	146.2	1624.54				Yes
HA04	49.00	25.27	2	151.4	1564.69	Rebound	817.243	817.243	No
HA05	39.26	25.99	0	166.6	1598.73				No
HA06	61.61	34.01	2	150.7	1624.54	Rebound	769.729	769.729	No
HA07	74.37	42.76	2	147.4	1624.54	Unclear	788.734	788.734	Yes
HA08	29.66	22.22							No
HA09	45.28	30.20	0	138.2	1624.54				Yes
HA10	27.69	21.93	0	121.3	1624.54				Yes
HA11	50.64	33.50	0	144	1624.54				No
HA12	30.99	27.31	4	139.2	1672.38	Rebound	468.806	475.141	No
HA13	45.61	23.95	2	151.0	1672.38	Splat	902.768	902.768	Yes

The experiment HA11 did not have the same result as the others. Instead of the laser firing when triggered, it required a second trigger to fire and then fired twice instead of once. There were also no images recorded during this launch. Whether this was due to the illumination laser not firing in sequence or the double-trigger, or the existing issues with the illumination laser is not known. This specimen was not considered for further analysis.

Table 4.7: Iteration 3 LASHPOL results, using Old batch of AA6061 powder from Supplier A. Particle on HB04 was suspected to be missing after the launcher was dropped in transit and was not launched. Launcher for HB13 was cleaned and re-used for the fourth iteration without having been tested in the third iteration.

Index	Particle Major Axis $[\mu m]$	Particle Minor Axis $[\mu m]$	Frames	Substrate heating [°C]	Laser Power [mJ]	Result	Average Velocity $[m/s]$	Max. Velocity $[m/s]$	Kept
HB01	45.48	16.91	2	141.0	1672.38	Rebound	836.248	836.248	Yes
HB02	54.96	41.67	2	143.0	1672.38	Rebound	798.237	798.237	Yes
HB03	27.10	22.28	2	151.7	1672.38	Rebound	769.729	769.729	No
HB04	39.57	24.56							No
HB05	45.65	29.91	2	136.8	1672.38	Unclear	726.966	855.254	No
HB06	52.55	20.96	2	144.8	1672.38	Rebound	779.232	779.232	No
HB07	48.70	38.07	0	139.0	1672.38				No
HB08	40.14	36.60	2	150.0	1672.38	Splat & Rebound	633.522	826.746	Yes
HB09	34.04	25.21	2	146.5	1672.38	Rebound	798.237	798.237	No
HB10	67.86	30.83	2	150.8	1672.38	Splat & Rebounds	826.746	864.757	Yes
HB11	32.03	21.93	2	140.1	1672.38	Rebound	760.226	760.226	No
HB12	41.88	18.69	0	140.3	1672.38				No
HB13	53.90	36.00							No

No apparent differences were found between the behavior of the Old batch (HB specimens) and New batch (HA specimens) from Supplier A based on the initial test data. More robust results would require further testing, but time and resources were limited. The decision was made to continue using the New batch of powder for the final iteration.

Table 4.8: Iteration 4 LASHPOL results, using New batch of AA6061 powder from Supplier A. Particle on HAT07 was missing during measurement and specimen was discarded

Index	Particle Major Axis $[\mu m]$	Particle Minor Axis $[\mu m]$	Frames	Substrate heating [$^\circ$C]	Laser Power [mJ]	Result	Average Velocity $[m/s]$	Max. Velocity $[m/s]$	Kept
HAT01	46.31	31.54	0	153	1672.38				Yes
HAT02	38.43	27.05	2	144.0	1672.38	Unclear	807.740	807.740	Yes
HAT03	47.27	25.29	2	143.0	1672.38	Splat	760.226	760.226	Yes
HAT04	27.64	22.92	2	137.0	1672.38	Rebound	788.734	788.734	Yes
HAT05	32.30	26.86	2	140.0	1672.38	Unclear	712.712	712.712	Yes
HAT06	30.71	23.48	2	162.0	1672.38	Rebound	703.209	703.209	No
HAT07									
HAT08	36.63	23.20	0	134.2	1672.38				Yes
HAT09	23.67	16.88	2	125.7	1672.38	Rebounds	755.474	798.237	No
HAT10	78.02	40.82	2	144.5	1672.38	Rebound	665.198	665.198	No

As noted in the methodology, two different thicknesses of substrate sheet were used. The experiments with indexes HAT used the thicker of the two (0.5 mm), in an attempt to achieve more particle splats in the testing. Based on the initial data, this was not necessarily successful, though also fewer specimens were tested due to time constraints.

Depending on the instant at which the substrate heating was turned off of active heating, and where it was in its own control/regulation loop, the temperature of the substrate may have been fractionally higher or lower than the recorded values. Also, the instant at which it was read, relative to when the shot was triggered, varied depending on the operator's signal to me that it was okay to step into the path of the laser and check the readout (see Appendix E for more information). As such, some of the recorded values were (slightly) inaccurate, though they were as close as could be recorded with the given setup and arrangement.

Each launch destroyed the launcher and a particularly fractured example is shown in Figure 4.31.

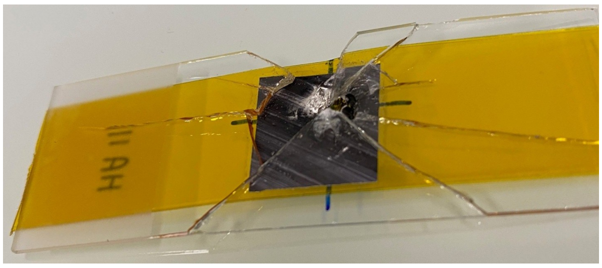

Figure 4.31: Destroyed launcher of HA11, with pieces of glass missing

For some of the specimens, more than one apparent particle was identified in the images from the launch. These additional particles, whether satellites or separated agglomerates, were included in calculations for the average velocity for the launches. For several of the heated experiments, despite only having two frames to track velocity, more particles appearing yielded more data from which to calculate the average velocity for the launch. These specimens were A02, A07, A10, A17, HB05, HB08, HB10, and HAT09. Hence, both the average velocity (across all frames and any particles present) as well as the maximum were reported based on the images. This could have resulted from misalignment of the laser with the exact location of the particle, or the force of the launch could have disturbed attached particles into separate entities. Additionally, the launcher surfaces were not pristine, and some debris or discarded powder particles could have remained and also been launched during the shock.

With each launch, any recorded images were checked to assess if there was a rebound or a splat. For some of the launches, this was unclear in the captured images, which was noted in the results tables for each experiment. Several examples of different launch image sequences are shown in the following pages. While these are presented here in a certain order, this does not replicate the order during experimentation (1.A, 2.HA, 3.HB, 4.HAT). The more violent launches resulted in more debris flying behind and around the particle(s) and more difficulty in determining the outcome of the launch. An example of this is shown in Figure 4.32.

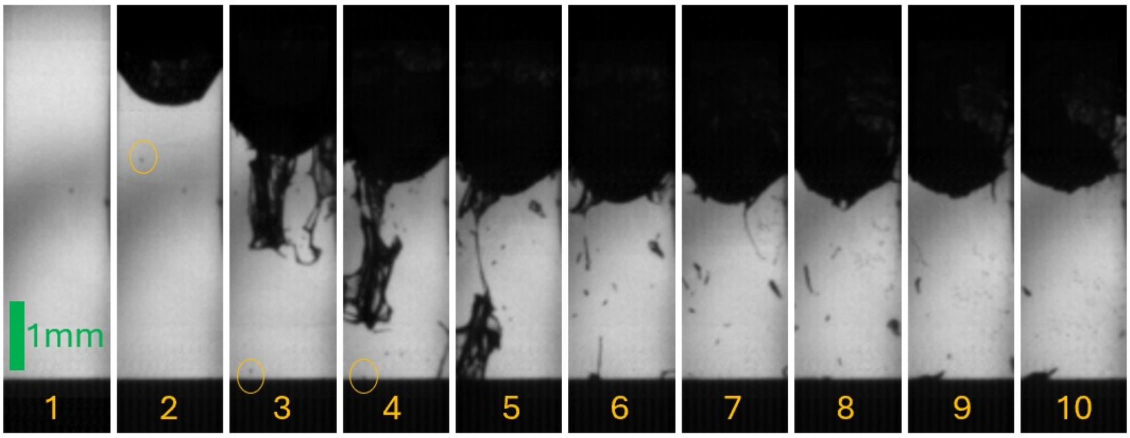

Figure 4.32: Violent launch of particle HA13. Particle tracked through the image frames with light orange ellipses, including suspected splat in image 4, where it remained on the receiver. Total distance represented in the images is 6.08 mm, and the scale of 1 mm is illustrated in green

While the apparent particle remained visible for this specimen despite the debris from the launcher following it, the same was not true of all the ”unclear” images. Some that fell into this category had a different flight path for the particle and went out of frame, like HA07 shown in Figure 4.33.

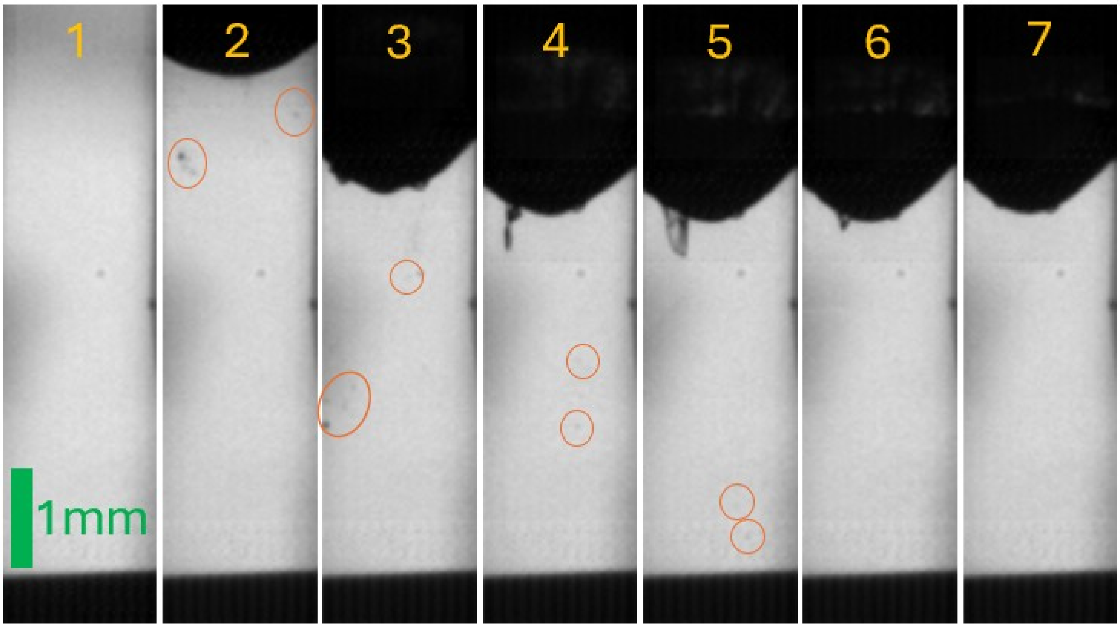

Figure 4.33: Unclear launch of particle HA07. Main particle left the frame after image 3, though some smaller particles seemed to continue the straight trajectory towards the receiver in images 3, 4, and 5. Total distance represented in the images is 6.08 mm, and the scale of 1 mm is illustrated in green

There were multiple particles visible in the images for this specimen, and on further inspection of the receiver under the microscope, multiple rebound sites were found. Exactly which particles imaged in flight caused these rebounds was not clear.

The influence of the guidance carriage, which supported the launcher and provided a channel through which the particles flew, was seen in some of the captured images. Below, in Figure 4.34, the shock-wave remains present and clear up through image 5.

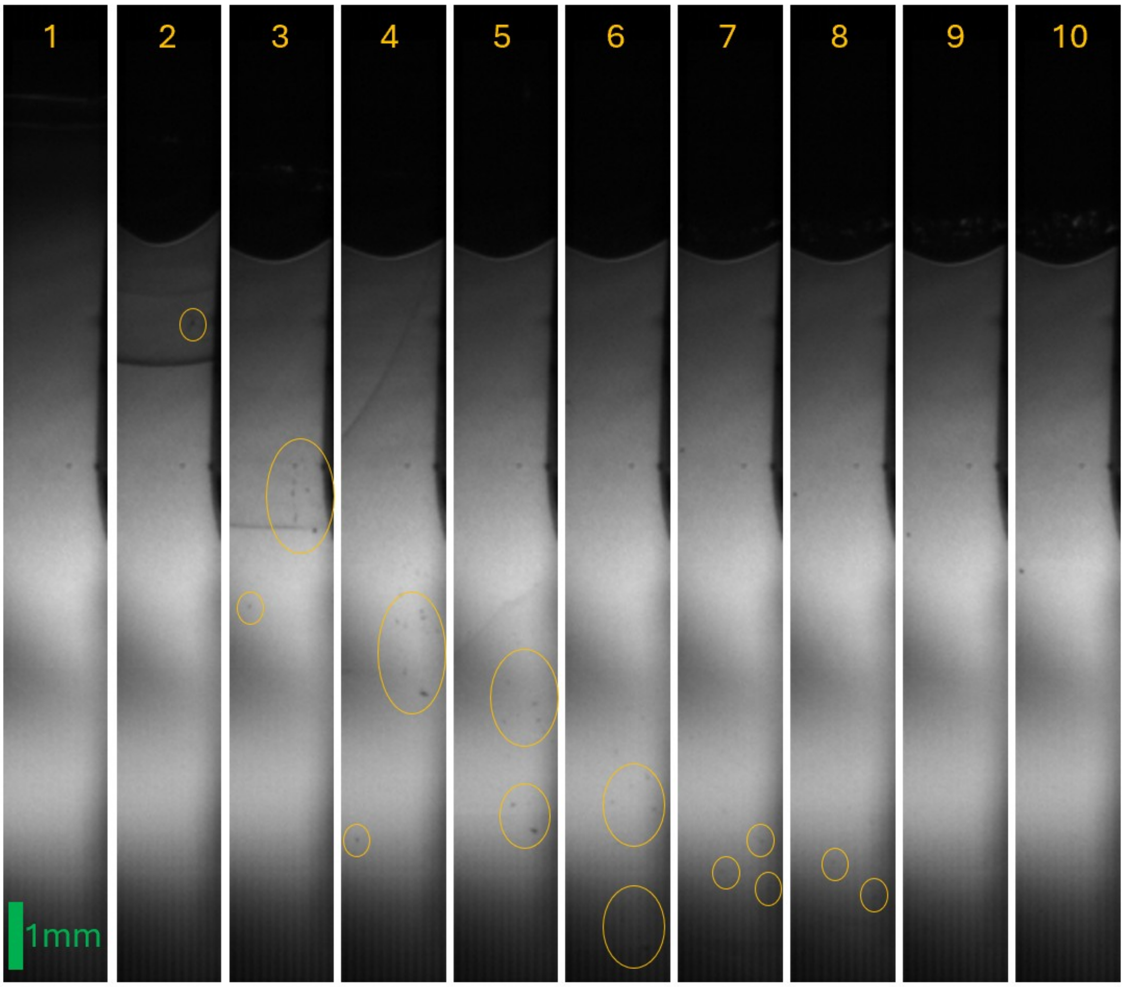

Figure 4.34: Clear launch of particle A03. Shock front visible in the first images. A single particle in image 2 became multiple particles in different regions as early as image 3. Total distance represented in the images is 14.19 mm, and the scale of 1 mm is illustrated in green

This was also an example of a single particle multiplying into several particles. It would not be accurate to conclude that multiple splats or rebounds occurred based solely on the launch images. This is because debris from the launcher itself could have been imaged and could have been interpreted as additional particles, depending on their size and position. The receiver for this specimen was kept to be examined under the microscope because of its behavior. As this experiment was without substrate heating, the distance between the launch position and the receiver was greater, and there were more opportunities to observe particles in flight as a result.

One of the clearest examples of multiple particles obviously launching in a single event is shown in Figure 4.35.

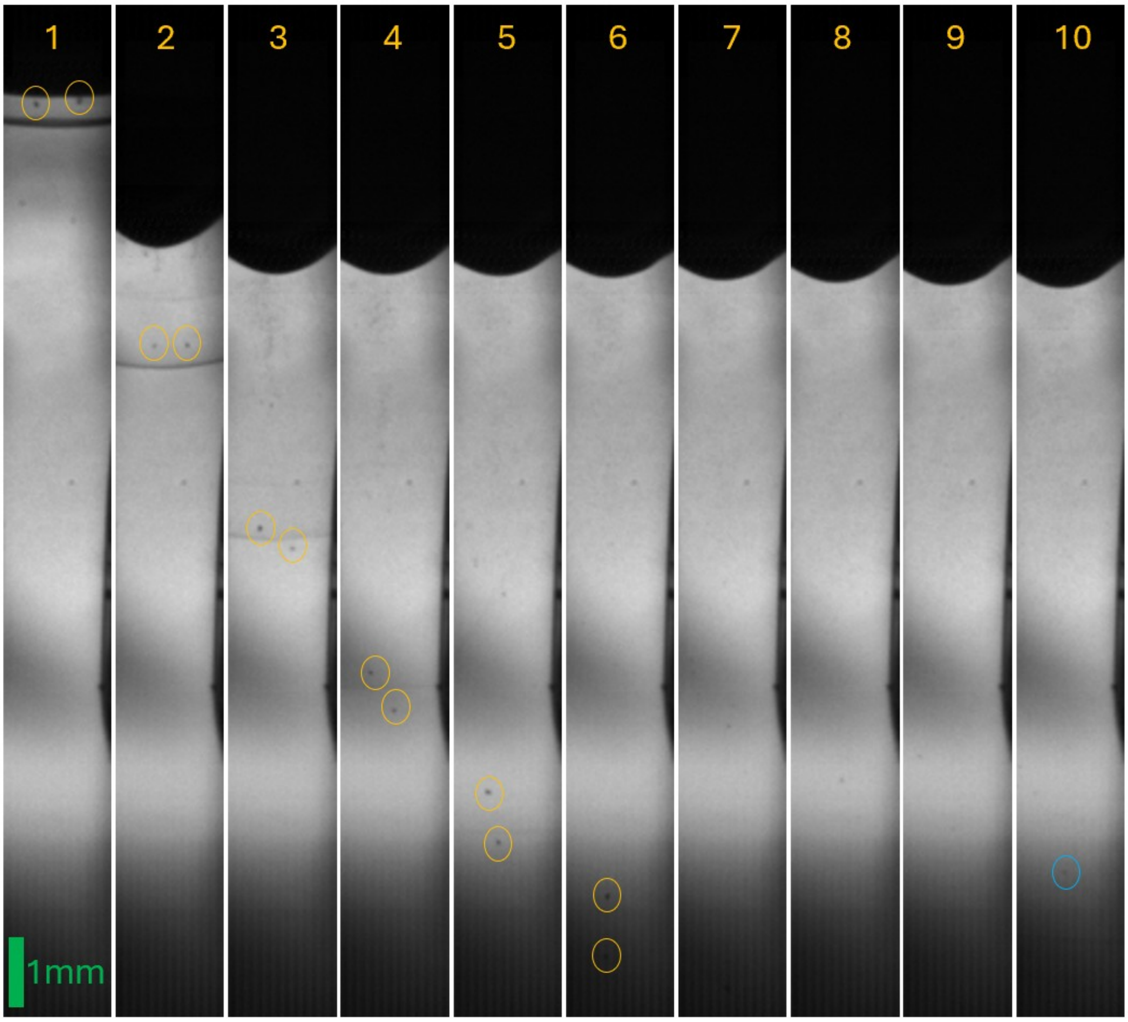

Figure 4.35: Two particles launched with A07. They remain centered in the view, though their condition after impact was not clear. A potential rebound or trailing particle highlighted in image 10 with the blue ellipse. Total distance represented in the images is 14.19 mm, and the scale of 1 mm is illustrated in green

Both of these particles were launched from the same location, and behaved very similarly to each other. Thus, they were both considered to be actual particles, rather than debris from the launcher. Because the illumination of the substrate did not show the edge cleanly, whether either of these particles was a rebound or splat was not clear. The receiver for this specimen was kept for further examination.

Lastly, a single particle that was launched for HAT03 was deemed to have been a splat. However, on a second look at the images, what appeared to be a rebound was present in image 5, along with the beginning of a diffuse debris cloud coming from the launcher. This is shown in Figure 4.36.

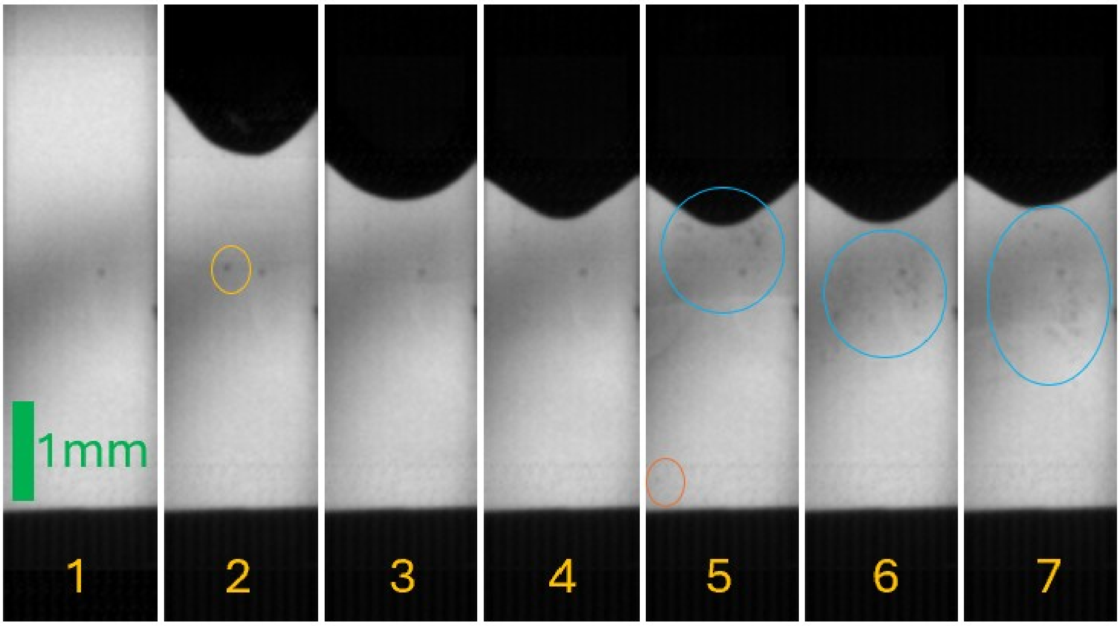

Figure 4.36: Particle launch (light orange) and potential rebound (darker orange) for HAT03. A slow-moving debris cloud followed the launch (blue). Total distance represented in the images is 6.08 mm, and the scale of 1 mm is illustrated in green

This specimen, along with several others, underscored the need to further examine the receivers before the outcome of the launch could be clearly determined. Not every receiver was kept for further examination, but those that were kept helped to identify some of the particle behaviors during launch and impact.

4.2.1. Optical Microscope Analysis of LASHPOL Receivers

All 25 of the kept receivers were examined under the microscope to determine if there was a splat present, regardless of the video evidence from the launch (if images were taken successfully). Once a feature (splat or rebound) was identified under the optical microscope, two edges of the receiver were marked with ink to indicate the location (at the mapped intersection of the two lines). This allowed for repeatable examination of the relevant features. Several receivers had multiple relevant sites. This was interesting, since ostensibly only one particle was supposed to be launched for each experiment. As mentioned in the above section, this could have been due to difficulties in aligning the laser shock with the exact location of the particle on the launcher. Or, the force of the shock could have encouraged an agglomerated particle or one with multiple satellites to break apart in flight. Any debris on the surface of the launcher could have been interpreted as a particle once the launch was imaged, as well. Thus, a verification of the state of the receivers was necessary.

While every kept receiver was examined and imaged, not every image is included here. One of the kept receivers, A02, was found to be completely blank of any particle rebounds or splats. This was not especially strange given the low velocities calculated from the launch images, but it was the only receiver to have absolutely no evidence of the launch.

The following section highlights some of the findings from the optical microscope evaluation of the LASHPOL receivers. The summary of all the findings is presented at the end and compared to the previous results which were based on the launch image analysis. The results from three receivers are presented here:

- A03: multiple particle impact sites after a ”single” launch
- HA03: a single particle splat
- HAT03: both a single particle splat and a rebound site after a ”single” launch

While the cause for multiple particles being launched in a ”single” event was not known, the effect could be seen on some of the receivers. Receiver A03 showed the impact that multiple particles had on the substrate, where four distinct rebound sites were identified and are shown in Figure 4.37.

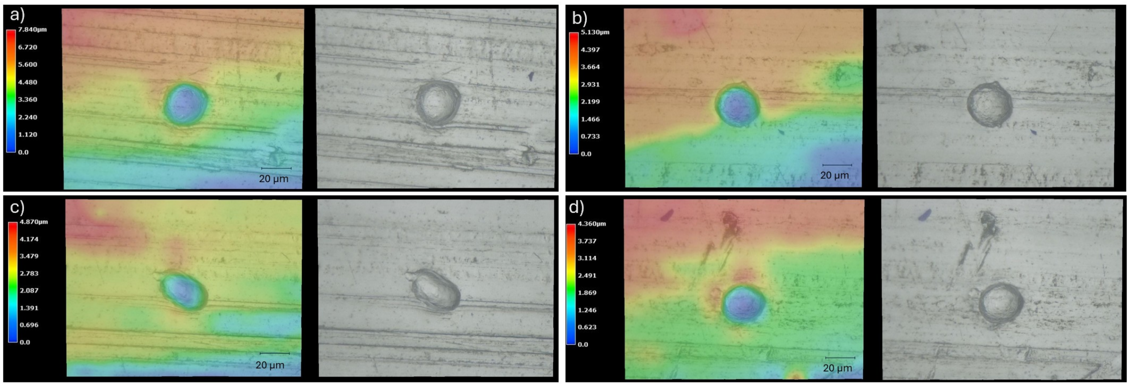

Figure 4.37: Images of the receiver A03 showing: a) Round rebound 1, b) Round rebound 2, c) Elliptical rebound, d) Round rebound 3

The height mapping indicated impressions in the substrate material, and some material deformation around the edges was clear as well. Evidently, the energy was not high enough to promote adhesion for any of the particles.

While there were no images collected, and so no velocities calculated, inspection of the receiver for HA03 revealed a successful particle splat. This is shown in Figure 4.38. The conditions for this launch were apparently sufficient for the particle to adhere to the substrate, and significant deformation of both particle and substrate resulted in a mapped height of 14.5 μm.

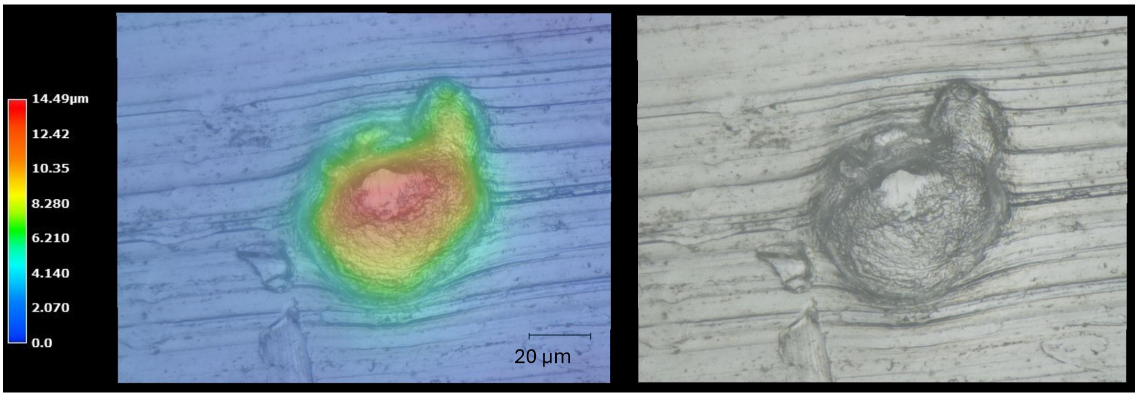

Figure 4.38: Particle splat on receiver HA03

Around the splat the substrate material has been deformed due to the high energy impact, seen by the curvature in the lines immediately around the splat. The shape of the splat was identical to the originally imaged particle before the launch, though the height component had not been measured. Assuming that the thickness (from this top view) of the particle was similar to the width during measurement (30 μm), then about half of the particle was embedded into the substrate. The very edges of the splat also indicated this degree of deformation, as along with the substrate deformation some small rolling wave or cresting wave forms could be seen. This was especially apparent on the left side of the upper portion of the particle (from the small limb on the top-right). The much darker region immediately between the substrate and splat there indicated more material ”build” by the flattening of the particle to fill its impact crater.

The last example of the receivers to be presented in this section of the thesis is HAT03. As mentioned related to the launch images, this specimen was initially recorded as a splat, but a second look identified a potential rebound in a later frame. Following the examination of the receiver, the two points of interest that were found are shown in Figure 4.39.

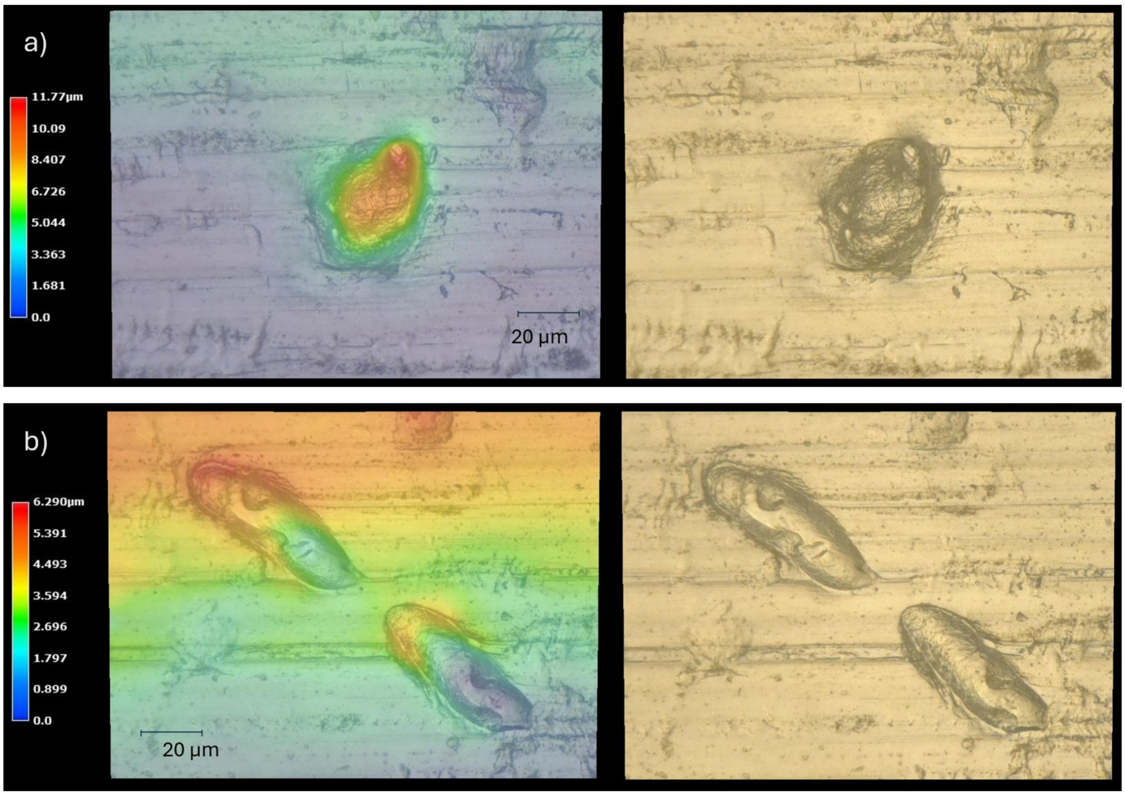

Figure 4.39: Images of the receiver HAT03 showing: a) splatted particle and b) two rebound trails

While the splat exhibited the expected features of deformation in the substrate and flow of the particle material around the edges, the more interesting of the two imaged features were the rebound trails. Features similar to these had been noticed on other receivers, but because of sharper edges through the trails they were identified as machining or cutting flaws on the surface. Based on the height map, and because of the smoother channels leading to material deformation at the top end of each of the channels, it was concluded that something round made these marks on the substrate. This was most likely an extremely oblique-angled entry and exit from the substrate material: a glancing impact that left much longer marks than typical rebounds. It was more likely two particles contributing to this feature, rather than one that bounced out of the first and had sufficient energy and lateral motion to carve the second. This rebound feature could be why there was a sudden rebound from out of frame in image 5 of Figure 4.36.

Based on the microscopic analysis of each receiver that was kept, the number of splats for each of the iterations was adjusted. This was still not a complete picture of the testing result, since half of the receivers were discarded and not examined again. Also, since the data from the images was not always captured, the velocity recordings for some of these experiments are not recorded and so could not be utilized in any analysis or comparison between different launches and splat behaviors. Regardless, the conditions of the kept receivers examined under microscope are shown in Table 4.9 below, compared with their assumed conditions based on the images collected during the launch.

Table 4.9: Results of microscopic evaluation of receivers kept from LASHPOL testing

Index	Assumed condition	Microscope evaluation
A02	Rebound	
A03	Rebound	4 Rebounds
A05	Splat	Splat & Rebound
A07	Unclear	Small splat & Rebound
A09	Rebound	Rebound
A12	Rebound	3 Rebounds
A13	No images	Satellite splat & 2 Rebounds
A15	Rebound	Rebound
HA01	Rebound	Rebound
HA02	Rebound	Small splat & 2 Rebounds
HA03	No images	Splat
HA07	Unclear	3 Rebounds
HA09	No images	Splat
HA10	No images	Rebound
HA13	Splat	Splat & other features
HB01	Rebound	2 Rebounds
HB02	Rebound	Rebound
HB08	Splat & Rebound	Splat
HB10	Splat % Rebounds	Splat
HAT01	No images	3 Rebounds
HAT02	Unclear	Rebound
HAT03	Splat	Splat & Rebound
HAT04	Rebound	2 Rebounds
HAT05	No images	3 Rebounds
HAT08	No images	2 Rebounds

What could be concluded from this collected data was that there was little difference between the behavior of the two batches. Again, the New batch of AA6061 from Supplier A was used in the experiments with the letter A in the index, and the Old batch of powder from the same supplier was used in all experiments with B in the index. Given the small number of tests, this testing would need to be repeated with more specimens to have a definitive result, but the implication is that the launches seem to be insensitive to any batch differences.

4.2.2. SEM-EDS Analysis of LASHPOL Receivers

Several of the receivers were also placed in the SEM and examined in combination with EDS. These were the receivers for A03, A05, HA03, HA13, HB01, and HB08. With the markings from the optical microscope, the approximate locations for the splats or rebounds could be found again in the SEM, without needing to extensively search for them again. The location for the splat on A05 was not able to be found when in the SEM at DASML, though this receiver had already been examined at Mines-PSL in their Zeiss Gemini SEM. An image and description for this splat can be found in Appendix B.

The rest of the analyses of the receivers with the SEM are split in two parts: those with splats and those with rebounds. Some of the receivers with both splats and rebounds are included in both sections, as the different sites were relevant to both analyses.

Analysis of Splats

The receivers with splats that were analyzed in the SEM were A05, HA03, HA13, and HB08. Because the particle could not be found when A05 was placed in the SEM, the analysis presented here will begin with HA03 instead.

Under SEM-COMPO imaging mode, the degree of material deformation during the impact was very clear. As seen in Figure 4.40, the boundary of the substrate around the splat has crested, having been pushed outwards by the impacting particle into what looks like a mountain range.

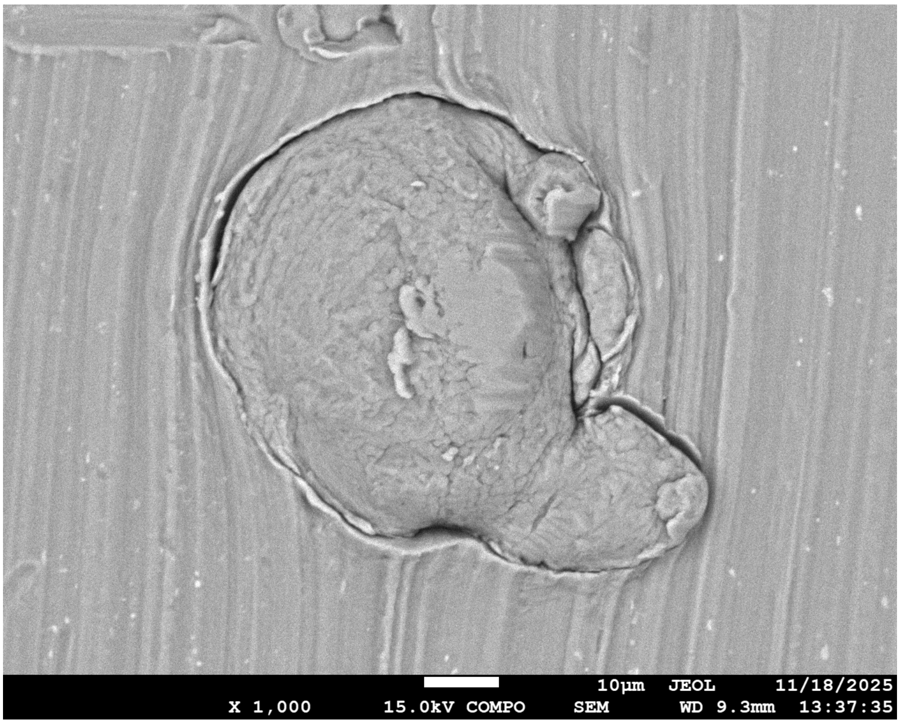

Figure 4.40: SEM-COMPO image of particle splat on receiver HA03 at 1000x

Also around the edges, but of the particle, were smoother sections, where it appeared the particle experienced perhaps jetting or at the least some material flow. This was all in line with a high-velocity impact and strong adherence to the substrate.

This image was then mapped with EDS for the same elements as was done for the powder characterization. Because the area of interest was just this splat, only one map was taken that encompassed the splat and the nearby substrate. However, this receiver was imaged on two separate occasions to provide more refinement to the EDS map. In the end there were two mapped regions and 40 points across the two measurements.

The region of the receiver HA13 that was believed to have a splat was imaged with the SEM, but upon this examination it was determined that whatever was on the surface was not a particle splat. This feature is shown in Figure 4.41.

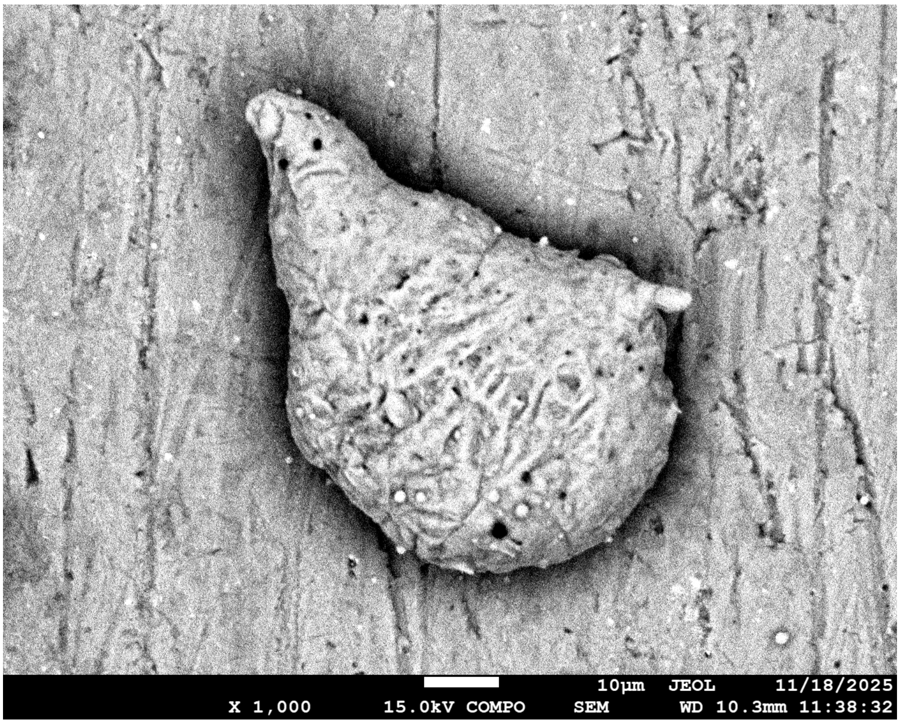

Figure 4.41: SEM-COMPO image of (not) a particle splat on receiver HA13 at 1000x

As can be seen in the image, the ”particle” is set on top of the substrate surface and there is a harsh outline around it. The surface of the ”particle” did not appear similar to any previously imaged in the SEM, with strange fibrous features rather than grains or a smooth surface. There was still a splat of a small particle on this receiver, but this was not imaged in the SEM. The ”particle” was also examined with EDS, but not with the intent of determining the conditions of the boundary. The surface of the substrate on this receiver had been prepared with Scotch-Brite prior to the launch, and a map was taken to observe the effect this had on the substrate. This resulted in a higher baseline oxygen content of the substrate than was seen for other receivers.

The last receiver with a splat that was examined in the SEM was HB08. As with HA03, the substrate deformation was clear from the image, shown in Figure 4.42.

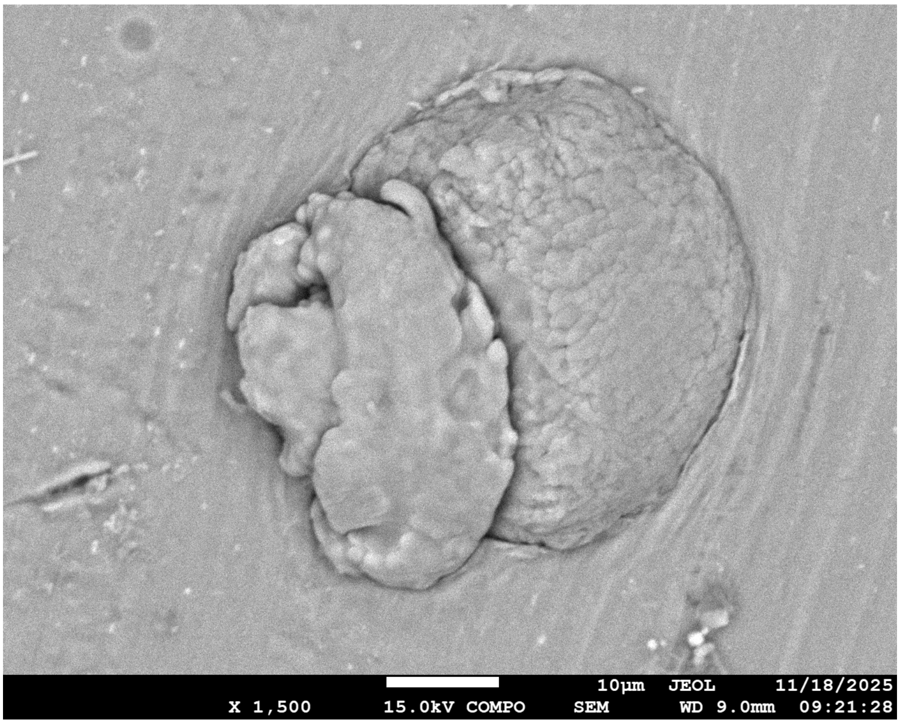

Figure 4.42: SEM-COMPO image of particle splat on receiver HB08 at 1500x

The particle clearly has two different surface appearances. The typical grain structure is visible on the right portion of the particle. The left portion seems to have a surface similar to others identified with a ”flow” quality to it. It smooth on the surface but also irregularly shaped with small nubs and bumps that must have formed during production by atomization. One map and 20 point-ID spectra were taken based on this image.

Analysis of Rebounds

The receivers with rebounds that were analyzed in the SEM were A03 and HB01. The receiver for A03 had four different rebound sites, and three of these were imaged, mapped, and point-identified.

Figure 4.43 shows the SEM-COMPO images of the three imaged rebounds on A03.

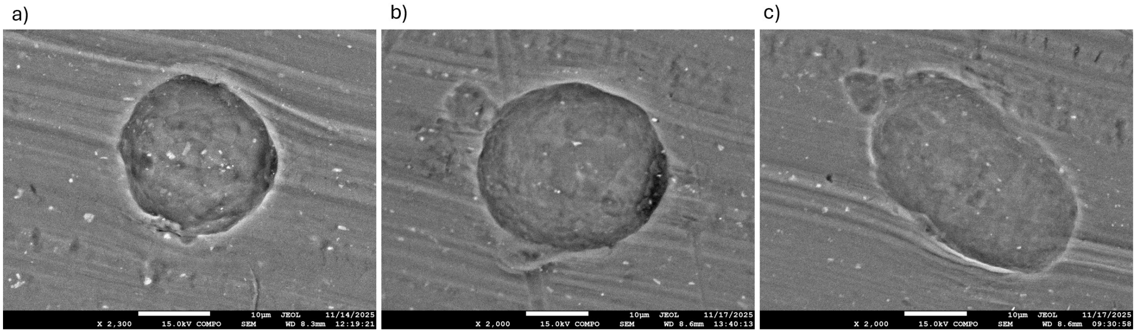

Figure 4.43: SEM-COMPO images of three of the rebounds on receiver A03. a) Round rebound 2, b) Round rebound 3, and c) Elliptical rebound as identified in Figure 4.37

The impressions left by the rebounding particles clearly forced some substrate deformation, though because of their depth and relative size, not to the extent that was seen on the splatted receivers. With

SEM-COMPO mode, brighter colors are associated with heavier elements, because they produce a stronger response for the backscatter electron detector. This information made examining the rebound sites very interesting, since each has a sort of halo around where the particle impacted that is very bright white compared to the rest of the substrate. This is particularly clear in the regions with higher deformation, on the peaks of the created ”mountain ranges” where the white color is densest in appearance.

Each of these rebound sites was mapped. In total across all of the rebounds, 90 point-ID spectra taken from points of interest. Namely, a high concentration of spectra were taken from the bright white looking regions at the edges of the rebounds. Also, based on the mapped concentrations of all the selected elements, anything left behind on the 1xxx substrate was also point analyzed, since there should not be high concentrations of anything other than aluminum. The mapped concentrations overall for each site and of some choice elements are presented in Figures 4.44, 4.45, and 4.46. These images show the alloy component maps that featured very dense regions of concentration that overlapped with features in the SEM-COMPO images.

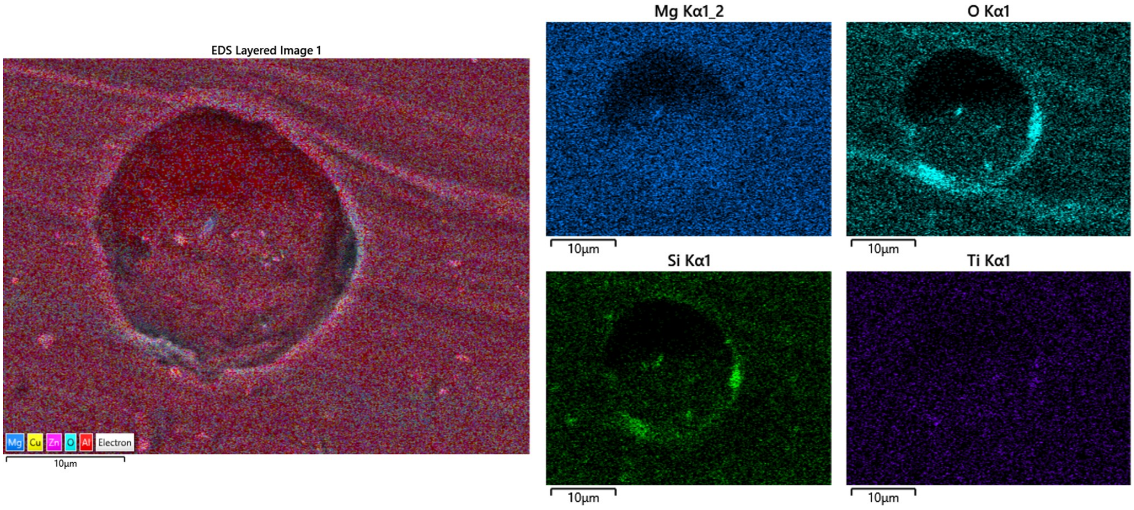

Figure 4.44: Mapped concentrations of elements of the round rebound site 2 on receiver A03

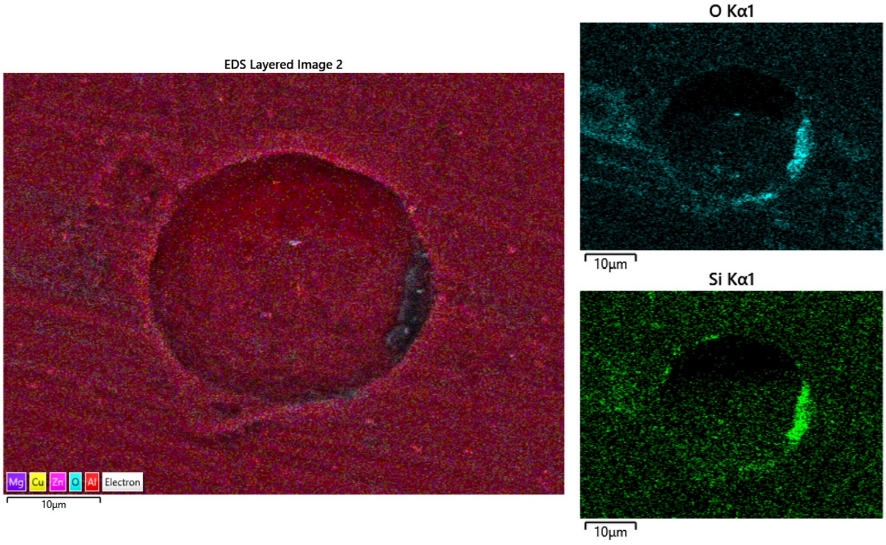

Figure 4.45: Mapped concentrations of elements of the round rebound site 3 on receiver A03

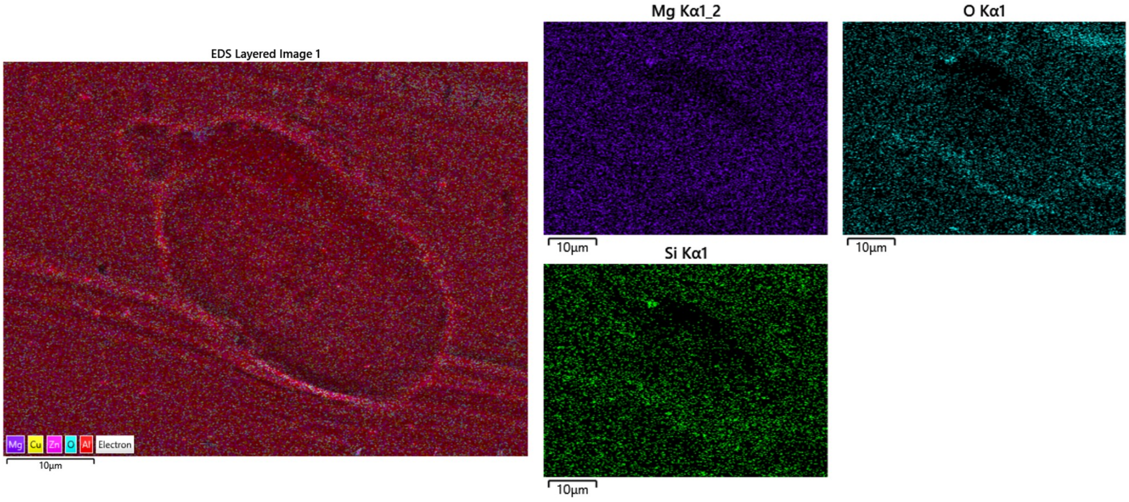

Figure 4.46: Mapped concentrations of elements of the elliptical rebound site on receiver A03

Despite the substrate not including any of the alloying elements, points identifying these elements were present nearly everywhere on the mapped images. This behavior was seen previously for very trace elements, where they were communicated as noise in the signal and appeared on the maps. However, the dense regions of elements always indicate true presence in the material at that location. From the round rebound site 2, shown in Figure 4.44, the point approximately in the middle of the crater was a combination of magnesium, oxygen, and silicon. There were two regions on the edges where titanium was present, but the general observation regarding these edge regions concerned a high concentration of silicon and oxygen. Since the substrate does not have these elements in its composition, these had to come from the launch of a particle at the receiver.

The round rebound site 3, shown in Figure 4.45, shows the same dense collections of oxygen and silicon at the edges of the impact location. Also, the point towards the center of the crater is an oxide of some form that does not overlap with any other element. So, it was likely an aluminum oxide, though whether it was already present on the substrate or being left there by the particle could not be determined.

The elliptical rebound site, shown in Figure 4.46, still has the same general pattern as the other two impact sites, but to a much lesser degree. A small region at the top of the crater had magnesium, oxygen, and silicon much like the middle of the round rebound 2. There is also an enrichment in the oxygen and silicon concentration following the lines towards the bottom half of the image, though whether this was an artifact of the substrate or not was not clear.

The final receiver with rebounds that was examined with the SEM was HB01. While this receiver had two rebounds identified under the optical microscope, only one was imaged and analyzed with the SEM. The SEM-COMPO image of the rebound site is shown in Figure 4.47.

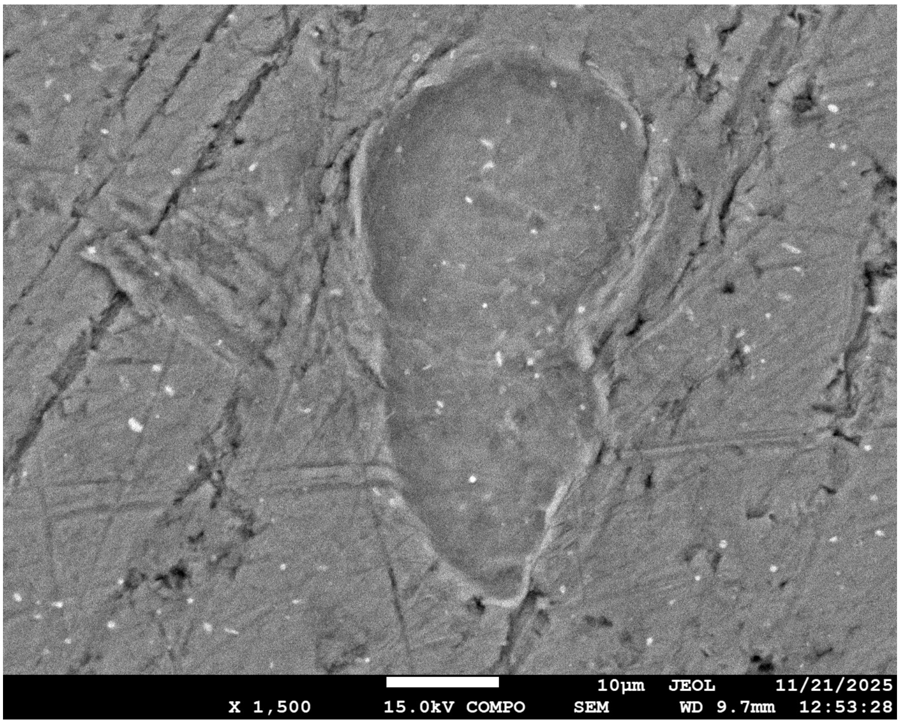

Figure 4.47: SEM-COMPO image of one of the rebound sites on receiver HB01 at 1500x

As with those on receiver A03, this rebound site has a halo of brighter white around the edge of the crater. The impact of the particle seems also to have contributed enough energy to the bottom of the crater to have smoothed out the two linear cuts that go horizontally across the image near the bottom portion of the crater. A single map and 20 point-ID spectra were taken based on this image. As with the receiver HA13, this top surface had been prepared with Scotch-Brite before the launch. It also had a higher overall concentration of oxygen, attributed to the substrate around the rebound site with a lesser concentration at the rebound site.

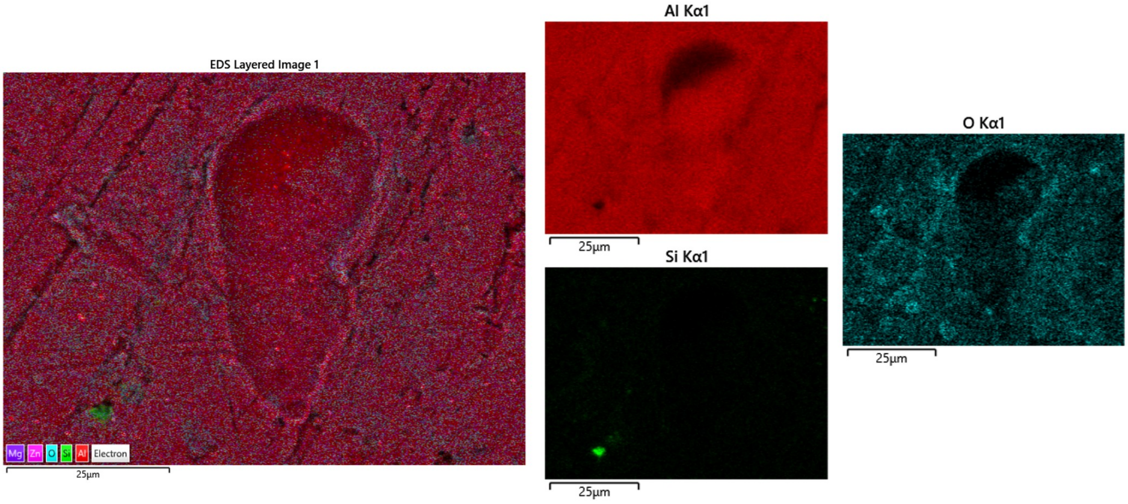

Figure 4.48: Mapped concentrations of elements of the rebound on receiver HB01

Figure 4.48 shows the overall mapped concentration and some highlights from the specific elements. The lack of aluminum combined with a dense enrichment of silicon and some oxygen in the lower left corner implied some sort of debris was present. There was some enrichment of oxygen around the edge of the impact site, but not quite so starkly as for the two round rebounds from A03.

Total Oxygen Content

As with the particle characterization via SEM-EDS, the total oxygen content from the mapped and point-ID spectra were collected and jointly plotted. However, because of the distinct differences between the different sites, and the preference for selecting oxygen-richer regions with the point spectra, the maps and point-ID results per receiver were not combined into single values. The results are shown in Figure 4.49.

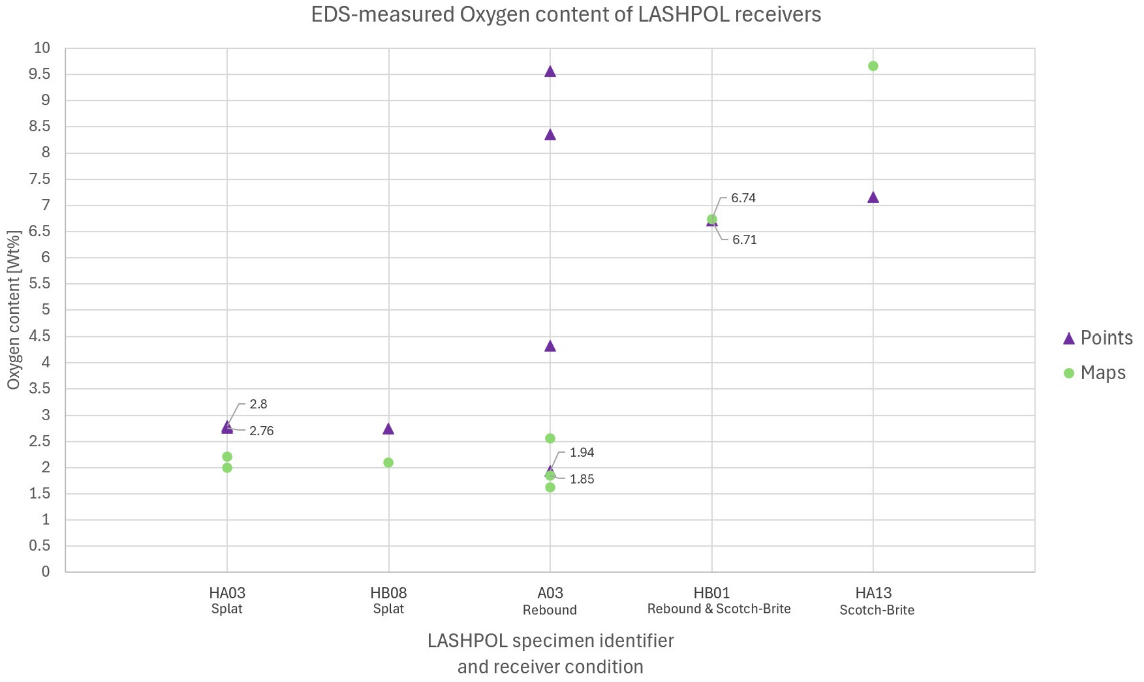

Figure 4.49: Oxygen content measured with EDS on 5 receivers with various conditions

From this, several things were clear. First, the splats had very consistent map and point-ID oxygen concentrations (HA03, HB08). Not only was the vertical offset between the mapped and point-ID concentrations very similar, so were the values themselves between the two receivers. The mapped concentration spans 0.2 wt% amongst the three mapped points, and point concentrations only 0.1 wt%. The influence of the different batches used (New for HA03 and Old for HB08) was not clear due to the similarity in results, though they were only single measurements.

Next, the point-identification from A03 has significant scatter in terms of the oxygen concentration. This resulted partially from measuring the content at three of the rebound sites, rather than from one single site. The measured oxygen variation between the different point-ID points in the plot and the offset from the mapped content results from the deliberate selection of lighter and brighter regions on the rebound sites for point identification. These were not excluded from the plotted data because they do communicate information about the state of the substrates after rebounds. However, because of the deliberate over-selection of lighter regions in the total area, the points identified do not correlate neatly with the associated maps of the measured regions for this specimen. Otherwise, the mapped concentrations for this receiver were similar to those of the receivers with splats, though with a greater scatter (and more measurement points which builds in chances for scatter).

Lastly, both of the receivers with a Scotch-Brite prepared substrate surface had considerably higher oxygen content, both for the maps and point-ID. The lowest value between the two receivers, the point-ID oxygen concentration for HA13, was more than twice the value of the splatted point-ID at 6.71 wt%. Examining the oxygen EDS maps for these two receivers showed that the substrate itself had a higher oxygen content in the background of each image.

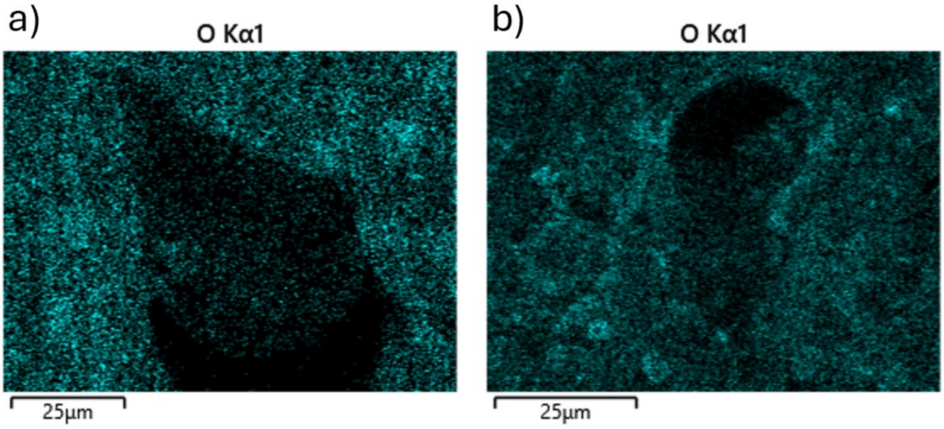

Figure 4.50: Oxygen maps for Scotch-Brite prepares substrates of receivers HA13 and HB01

Compared to the other oxygen maps, the density of oxygen outside the very strange object (on HA13) and the rebound crater (on HB01) is consistently higher. The only factor that connected these two receivers, other than being the same base material, was the preparation with Scotch-Brite before the launch. Whether the higher oxygen content was due to the preparation itself or the length of time between preparation and administering the test was not apparent.

4.3. Spray Testing Results

The last portion of the testing included a cold spray test with each of the AA6061 powders, to observe if any differences were apparent in the coating behavior. A velocity measurement was included in the test before the actual deposition, though due to misalignment of the nozzle with the camera, a skewed velocity distribution was the result. This means that only a portion of the spray plume was observed and measured, and the measurements cannot be taken as substantial proof of any behavior as a result.

As noted in the methodology, two nozzle traverse speeds were used:

- Slow speed of 20 mm/s, representing a material-build condition where a thicker coating can be deposited
- Fast speed of 500 mm/s, approximating single-particle launches and individual splat or rebound behavior on the substrate

As is seen in Figure 4.51, the visual difference between the two traverse speeds is apparent. The slow speed had a more opaque and dense coating due to its thickness, while the fast speed kept more of the substrate appearance with some disruption.

Figure 4.51: AA6061 plate sprayed with each of the AA6061 powders at different traverse speeds: slow is 20 mm/s, fast is 500 mm/s. The numbers 1 and 2 indicate the first and second deposits for each section according to the programmed path

The thicknesses of the coatings were measured, and they are presented in Table 4.10. Based on the particle size expectation, it is likely that the Old Supplier A coating had one to two more particles adhere in the thickness direction, though the measurements were not robust with only one sampling point per path due to the specimen size and geometry.

Table 4.10: Coating thicknesses from the spray test

Path	New A [mm]	Old A [mm]	B [mm]
Slow 1	0.09	0.13	0.04
Slow 2	0.06	0.19	0.06
Fast 1	0.02	0.03	0.01
Fast 2	0.03	0.02	0.02

These measurements indicate that for the slow traverse speed, the Old batch from Supplier A produced the thickest coating. The particle size expectation for the powder from Supplier A is 0.032 mm, which means the difference in thickness between the Old and New batches could be due to one to two more particles adhering with the Old batch versus the New. However, due to the sampling, these measurements are not robust and serve more as an indication. Given the consistency of the results between the different powders and the two speeds, the implication is that the coating behavior should be similar between the three batches of powder.

For the fast traverse speed, there was very little difference between the three powders, and the thickness overall indicated that single particles adhered. This was the intent of the fast traverse speed test, so it reinforces the possibility to use this method to examine individual particle splats from cold spray.

The coating surfaces were also examined under the microscope for height profiling. While stitching did not work on the specific microscope used, an indicative image of each spray path was taken for comparison purposes.

The fast traverse speed spray passes showed a higher density of rebounds, with only occasional splats. Some images of the surface mapping within these coated regions are presented in Figures 4.52, 4.53, and 4.54. The others can be found in Appendix C.

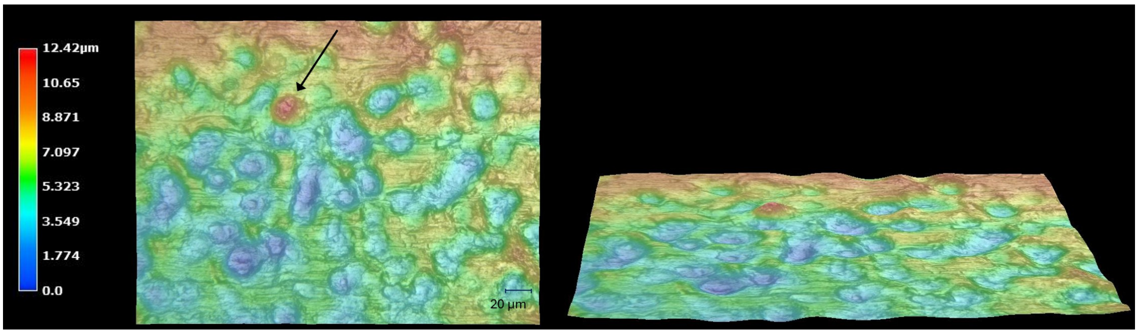

Figure 4.52: Surface mapping of the second spray path with fast traverse speed using the New batch of AA6061 from Supplier A

Of the various different height features visible in Figure 4.52, only one indicated a particle adhering. This was indicated by the red spot in the image, which the arrow is pointing towards. While the approximate diameter of this spot indicates it could be a particle, the height in comparison to the immediate surroundings is on the order of only a few micrometers. While the underlying surface cannot be identified, this spot was assumed to be a particle splat because of the combination of an appropriate diameter and increase in height from the substrate. Each of the blue features indicated rebounds, and even with a fast traverse speed, these tended to stack up on and very close to each other. This resulted in there being more complicated depressions in the surface than from the true single particle impacts of the LASHPOL. So, while the fast traverse speed was tested to be a connection to the single particle experiments, simply too much powder was included in the spray plume to directly compare in several cases.

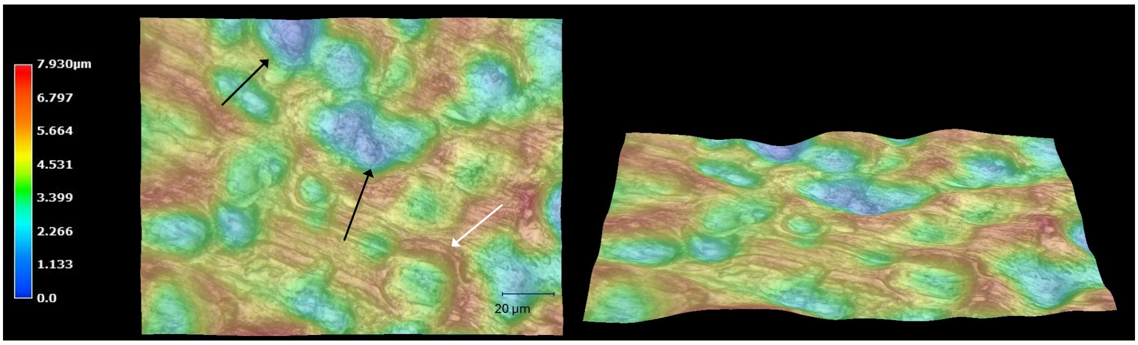

Figure 4.53: Surface mapping of the second spray path with fast traverse speed using the Old batch of AA6061 from Supplier A

With a higher magnification compared to Figure 4.52, Figure 4.53 shows more similar features to the LASHPOL impacts. Whether due to the imaging location or an actual behavior of the powder, the particle impacts appeared more distinct from one another. There were still sections (with the darker blue overlay and black arrows) where clearly several particles impacted and rebounded very close to one another. Despite having no splats visible, this was still an interesting sample to examine. One feature in particular, the rebound immediately to the left of the image scale, is indicated with a white arrow. This showed the amount of material flow present on the substrate even without particle adhesion. Clearly a larger particle rebounded here but did not have sufficient energy to adhere, while still displacing the substrate around the impact. This was also seen in the LASHPOL receivers. This stacking of material flow around several particle rebounds during spraying could affect further particle impacts and likelihood of adhesion due to altering the surface profile or leaving residual material.

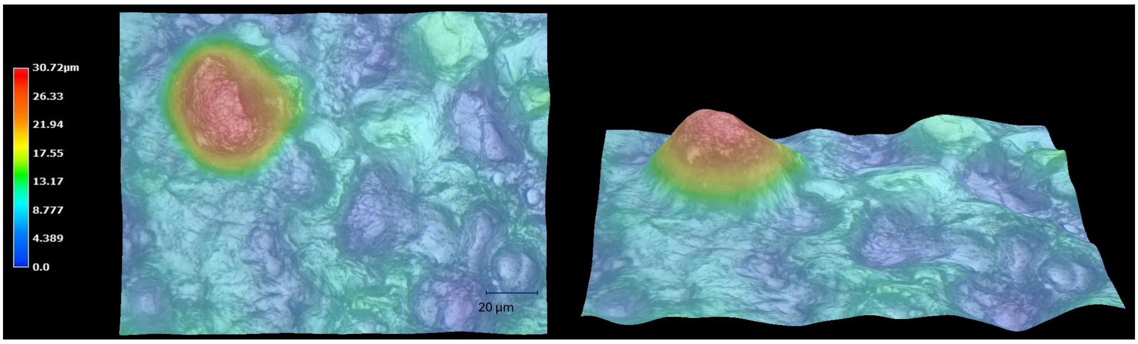

Figure 4.54: Surface mapping of the second spray path with fast traverse speed using the AA6061 from Supplier B

In Figure 4.54, a single particle splat is shown along with rebound craters around it. Whether the adhesion of this particle was influenced by, or occurred before or after the surrounding rebounds, is not known. However, it clearly demonstrates that if conditions are right, even with more rebounds in the surroundings, some particles can still adhere. Given that the total mapped height spanned 30 micrometers, and seeing as the diameter of the splat was approximately 40 micrometers, this particle could be considered somewhere between an average- and large-sized particle in the batch.

Also the slow traverse speed coatings were examined under the microscope. Some similar features to the fast speed coatings were identified mainly from those that had particles adhered to the surface. Such an example in the slow speed coating is shown in Figure 4.55, which has very similar appearance to that of the region on Figure 4.54 above. The area surrounding the highest particle splat were somewhat recessed, though a total height relative to the bare substrate surface could not be measured.

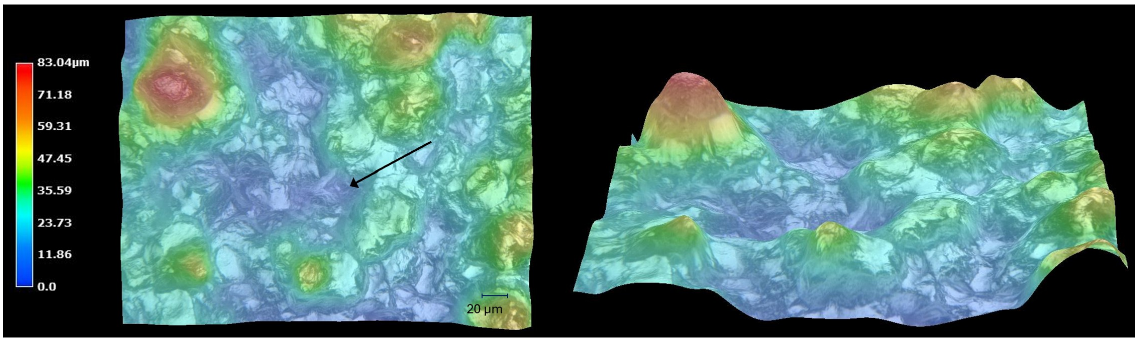

Figure 4.55: Surface mapping of the first spray path with slow traverse speed using the New batch of AA6061 from Supplier A

Given the total measured thicknesses of the coatings, it is likely that the area around the highest particle splat in Figure 4.55 is also comprised of splatted and adhered particles. What was also interesting are some of the dark blue regions, indicating the lowest (relative) height measured. Some of these had approximately round shapes, or could be decomposed into several round shapes immediately next to and on top of one another. The black arrow in Figure 4.55 is pointing at one such region. This meant that further particles were likely to have hit the already deposited surface and failed to adhere, rebounding away instead.

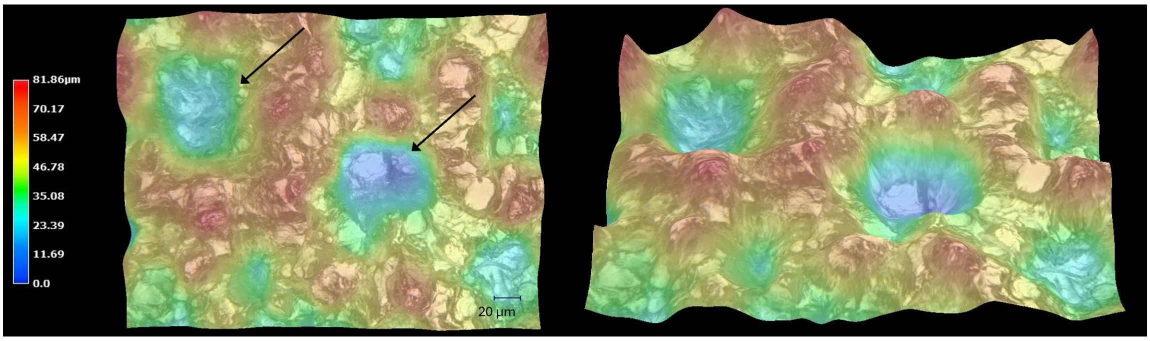

Figure 4.56: Surface mapping of the second spray path with slow traverse speed using the New batch of AA6061 from Supplier A

The previous assumption about the particle behavior was supported based on the surface in Figure 4.56, where deep circular pits were located in the height maps. These are indicated in the figure with arrows. Rather than the powder being deposited in ring formations, the most likely explanation for this behavior was the rebound of particles while the coating was still malleable due to temperature. Further examples of this phenomenon are shown in Figures 4.57 and 4.58.

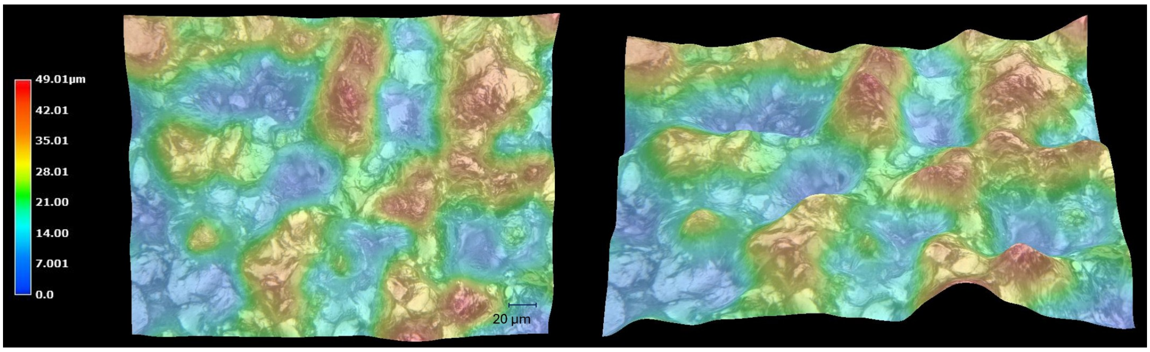

Figure 4.57: Surface mapping of the second spray path with slow traverse speed using the Old batch of AA6061 from Supplier A

Again in Figure 4.57, the larger sections of low height can be decomposed into several circular or semi-circular depressions made by several different particles rebounding. Some portions of the height difference do come from solely particles adhering to previously deposited portions, but the circularity in some of the low regions indicated rebounds rather than a previous layer's deposit.

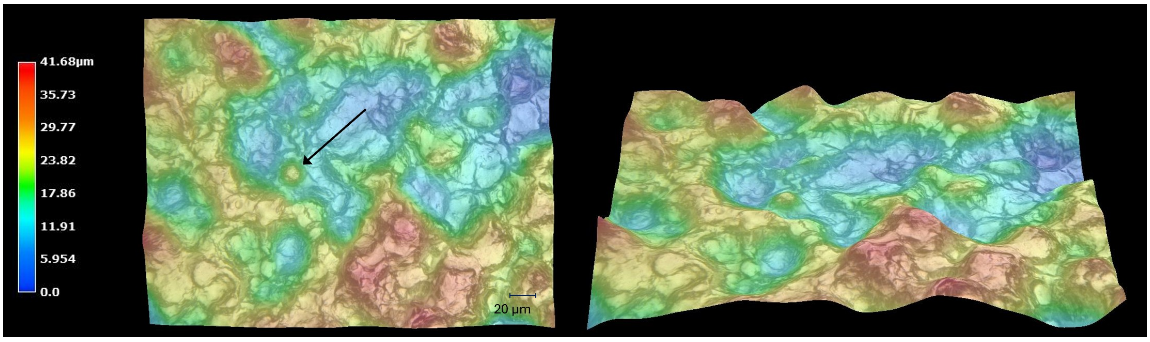

Figure 4.58: Surface mapping of the first spray path with slow traverse speed using the AA6061 from Supplier B

This example from Supplier B's powder coating also showed another aspect of the rebounding particles: the potential for leaving behind an artifact. The black arrow in the figure points out a high point in the surrounding (lower) material, and this was likely a smaller particle or even collection of satellites that may have remained in the impact crater of a previously rebounded particle.

A simple comparison between the images in terms of number of splats is not fair, because there were not enough sampling points and the magnifications differed. Though, with a higher traverse speed, the spray plume may have been disrupted, causing a higher likelihood for oblique rebounds without sufficient energy to splat and adhere to the substrate. This could have influenced some of the rebound patterns in the fast traverse speed coatings. However, the spraying sample and examination of the surfaces still gave an indication of the difficulties in particle adhesion, even with the appropriate temperature and pressure spray settings.

5

Discussion

All the data and information that has been collected and analyzed is discussed here. First, there is a comparison between the various powder characterization methods and what the collective results indicate about the condition of the powder over time. Then, the single-particle behavior seen in the LASHPOL testing is correlated with the fast traverse speed cold spraying and connected to the deposit-building traverse speed cold spraying. Lastly, the cumulative results are discussed to give a first indication of what the research means for cold spray coatings and for users of cold spray machines

5.1. Powder characterization and implications

Starting with the Raman spectra and the primary peak for the AA6061 powders at around 256 cm^{-1}, some differences between batch and suppliers were present in the measurements. Between the two batches from Supplier A, generally higher intensities of the primary peak belonged to the Old batch. This primary peak was taken to be an aluminum oxide, and the height of a Raman peak indicates the concentration. So, this means the Old batch had higher aluminum oxide concentrations on the surfaces than the New batch. And, with the AA6061 powder from Supplier B having the highest peaks of any of the tested powders, this should also have the highest oxide content measured.

Comparing this supposition to the XRD-measured concentration of oxygen with time shows that the Old powder did generally have a higher concentration than the New powder. The powder from Supplier B also had crystalline oxygen concentrations more similar to the Old batch from Supplier A than the New batch. The supposed relationship between the Raman peak height and the oxide content did not appear to carry over to the EDS measurements. With the exception of the last measurement point from the New batch from Supplier A, the EDS-measured oxygen for the three AA6061 powders were quite similar, though their individual trends were different. However, given the number of measurement points and the degree of scatter, this comparison in terms of the total oxide content and its influence on the other characterization methods may not reflect the true behavior of the powders.

On the basis of the primary peak being a result of an aluminum oxide, the variation of the different aluminum oxide phases were examined to explain some of the peak movements. For the Old batch of powder from Supplier A, the locations of the primary Raman peaks varied quite significantly between measurements. This would have resulted from changes in internal stress and strain in the particle. Typically this would indicate a phase transformation within the material, with the different unit cells forcing either shrinking or stretching of their neighbors.

There seemed to be the highest volume of changes in phase concentrations between measurements for the Old powder, based on the XRD measurements. This supports the observed shifting of the Raman spectra to higher and lower wavenumbers.

For the New powder, and the development of shoulders around the primary Raman peak (compared to the Old powder or that from Supplier B), the cause was attributed to phases shifting. However, since the overall peak did not shift significantly, and instead shoulders formed, it is likely that the intensity of the changes was lower for the New powder compared to the Old. This observation was supported by examining the crystalline Al_2O_3 concentrations of the two powders with XRD, where the magnitude of changes between measurements was higher for the Old powder than for the New powder. This could then cause the Raman response observed, where small shoulders formed rather than the peak shifting in its entirety as a result of having smaller fluctuations in the XRD measurements.

The AA2024 was the only powder for which a downwards trend in the primary Raman peak height (albeit not in the same location as for AA6061) was also emulated with the decrease of XRD-measured oxygen content with passing time. Decreasing crystallinity (or an increase in polycrystalline structures) is seen in a Raman peak with broadened widths. If the same aluminum oxide that was being detected and displayed in the primary peak located near 256 cm^{-1} in the AA6061 is also that which contributes to the AA2024 primary peak, then the results become more interesting. A shift to the right relative to the original peak location indicates an internal compressive stress was present. Broadening of the peak means cleanly organized crystals are becoming smaller, more disorganized, or an amorphous structure is emerging. So, the shape of the Raman peak in comparison to the other three powders implies a less ordered, more compressed structure. What exactly could cause that, and whether it would be accurate to make the comparison are not known. Further analysis would require another batch of similar material to make a better comparison.

Also worth examining closer is the total crystalline oxide content of the AA2024 powder. Given the XRD results, this powder had the highest oxide content compared to the AA6061 powders. This could be a result of the alloy composition and a difference in oxide composition leading to a more crystalline total structure. Or, it could be the consequence of the powder having been produced much earlier than the other powders. This was the only powder that was not sprayable with the existing cold spray machine, so it is likely that the oxygen content and oxide development was the source of this degradation.

Curiously, if one excluded the second EDS measurement for the New powder from Supplier A, a similar trend to the XRD-measured oxygen content could be seen. A similar single-measurement exclusion of the first XRD measurement for the Old powder then mimics the EDS pattern for those dates. There was no reason to remove these measurement points from the analysis, so these observations indicate the uncertainty of identifying clear patterns from the collected dataset. Similar behaviors between the XRD and EDS measurements for the AA6061 powder from Supplier B and the AA2024 powder could not be identified. An increase in the number of measurement dates as data points could support or counter these observations in future works.

Overall, the difference between the XRD and EDS measured oxygen contents was not insignificant. Likely due to some combination of amorphous and crystalline phases, the XRD-reported oxygen content tended to be lower than that measured with EDS. This held for each of the powders with the exception of the AA2024, which had a higher XRD-reported oxygen content than the EDS had. However, as with all of the EDS results including the point-identification, a high degree of scatter was present and given the small number of testing intervals these results could be inaccurate.

As noted in the results, the consistency in the Raman spectra for the powder from Supplier B was pleasantly surprising, given the other seemingly random fluctuations. There were still unexplained decreases in the intensity with time. However, the location, width, and other features of each spectrum were nearly identical between measurements. Based on the earlier reasoning about the phase transformations and Raman peak shifts, there were more fluctuations between XRD measurements for this powder than anticipated. So, the correlation between these methods for the tested powders is less certain. However, as with each of the other powders, the number of measurements for each characterization method was not identical, and additional measurements could clarify the correlation.

Based on the collected EDS measurements, the AA6061 powder from Supplier B also had the most consistent pattern in the overall oxygen content. In contrast to the other powders, there was a consistently upwards trend in the EDS-measured oxygen with time. This could be associated to the observation that this powder had the highest intensities in the primary Raman peak, which was identified as aluminum oxide. While the overall content was not the absolute highest, the consistent upwards trend in the EDS data showed a similar predictability as with the Raman data for the powder from this supplier. These observations combined to indicate this supplier's capability in producing consistent powder, though a comparison to another batch would be valuable in future.

While the underlying causes may not have been perfectly clear from the measurements, the observed fluctuation and increase in oxygen content of the powder over time would have an influence on cold spray. As noted in the literature review, thicker oxide coatings require more energy to fracture and permit jetting of the particle material during impact, and the increase in oxygen found in this research indicates the oxides are progressing with time. As seen with the AA2024 powder, which for this cold spray system was not sprayable, some of the behaviors and trends in the characterization data were seen to be similar to the sprayable powders. However, the clearest difference in the crystalline oxygen content between this powder and the AA6061 powders illustrates a possible explanation for the lack of sprayability, given the difficulties in breaking apart oxides during cold spray deposition.

5.2. Particle behavior in coatings

The LASHPOL experiments provided many examples of particles with the correct conditions to adhere that instead rebounded off the substrate. With the number of rebounds that occurred, despite the majority of particles having velocities within the expected critical velocity range (around 700-900 m/s) for aluminum powders [15, 21, 26], it is likely something else was contributing to the lack of splats. Even with the heated experiments, more rebounds were observed than was anticipated. This was regardless of the heating which should have improved adhesion and more closely mimicked the thermal conditions of the particles during cold spraying.

On examination of the receivers under the microscope, multiple rebound or splat locations were identified on some specimens. This meant that either multiple particles were present in the center of the launcher, or that the launch forced an agglomerated particle or a particle with several satellites to break during the launch. If it was the first scenario, then perhaps an alteration in the process of preparing the launchers with a higher magnification could allow, at the least, identification of specimens with this issue. If it was the second, it could be that the near-launch conditions, and because of the sudden impulse on the particle, force more irregular particles to behave strangely.

Typically LASHPOL and similar experiments are performed with near perfectly spherical powders. The powders used in this research were not perfectly spherical. This could have affected not only the near-launch behavior, but also the flight and the possibility for the particle to tumble rather than fly straight towards the receiver. In spraying conditions, with high pressure gas and other particles around, the flight behaviors tend to vary depending on the location within the spray plume. The specific behaviors seen in these LASHPOL results may be more indicative of particles flying near the more turbulent edges, with free air surrounding them.

The appearance of the rebound locations was consistent between the single particle testing and the fast traverse speed spray test. The craters formed by rebounding particles, and the buildup of material around the craters in somewhat of mountain ranges at the edges, were seen for both types of specimen. The number of rebounds versus the number of splats in comparison between the LASHPOL and spray test could not be determined. Stitching of the microscope images of the spray test sections could not be done, though in each imaged region a high volume of rebounds were visible compared to the at most single splats of the fast traverse speed deposited ”coating”.

Interestingly, the appearance of the fast speed coating was, while less opaque, similar to the actual deposit-building slow traverse speed sections across the three tested powders. Looking at the microscope images, this almost brushed visual effect on the surface was likely due to the many rebound sites catching the light, rather than splatted and adhered particles building into a consistent thin coating.

The EDS analysis of the rebounds from LASHPOL indicated that something may have remained on the substrate after the particle bounced off, and this tended to have a high proportion of oxygen present. Typically these were located on the edges of the impact or very near the center of the crater. These residuals could affect subsequent particle impacts and their chance of adhering in a true spraying scenario, due to the higher proportion of oxygen and other elements as contaminants at the required bond layer. This could carry over to coating deposition in three potential scenarios. The first is in the initial stages, where a bonding layer of powder is deposited on the substrate. If interrupted by previous particle rebounds, the overall coating could have a poor adhesive bond to the substrate and a coating could fail prematurely. The second scenario is related to the intermediate stages of deposition, where powder is deposited on previous powder layers. Interruption of the bonding here could impact the cohesive strength of the coating, and the coating could partially chip or scale off during loading. The third scenario is related to the final depositing layer. The top layer of the coating is the last material-build layer, and if the conditions are not met to permit bonding with the established coating, the final pass will instead function like shot-peening. The incoming particles in the stream would rebound off the surface, inducing higher compressive stresses in the coating as opposed to finishing the layer building. The effect that each of these scenarios would have on a deposit is not quantified, but should be investigated to understand failure modes of cold spray coatings.

The deposition efficiency is usually expressed as a ratio or percentage, and represents the mass or volume of powder deposited versus how much was sprayed at the substrate. If rebounds happen with greater frequency due to the condition of the powder, or are unaltered from the expectation but instead leave behind contaminants affecting subsequent particles, this has the net effect of fewer particles being applied to the coating and lower efficiency of the process. While not necessarily a negative aspect of the process (though potentially an expensive one if powder isn't utilized) this could result in thinner coatings than designed for. For users, this could mean that more powder than was planned needs to be fed into the machine for a given coating dimension, though this would need be determined for each system and its capability.

As was seen in the slow traverse speed spray tests, the top layer of the coating that was examined had several craters that seemed to have formed because of rebounding particles striking the surface at the end of spraying. Whether these particles would be relevant to the desired thickness or not, they also induce compressive stress in the coating. This is especially the case in the top layers, where subsequent particles may repeatedly impact the surface rather than contributing material to it.

If the powder condition that was measured with the characterization methods was influencing the rebounds and thus the cold spray deposit efficiency, the stress distribution and the composition through a coating would likely be more complex. However, as this could not be assessed during this research, it is recommended to examine the effect on different coatings to determine the cost that comes with the powder degrading over time.

5.3. Implications for Cold Spray

There is some influence of time on the impact behavior of the particles. There were differences in some of the measured conditions related to the powder suppliers. Likely phase transformations and continued growth of oxide layers on the powders was identified more clearly for the two batches of AA6061 powder from Supplier A. There was more consistency in the results for the AA6061 powder from Supplier B, though the likely degradation of the powder by the further development of oxides on the particles was still observed. A possible explanation for the cold spray system being unable to spray the AA2024 powder was the high crystalline oxide content measured with XRD. A comparison to another batch of the same alloy should be performed to confirm this was the limiting factor for sprayability.

The LASHPOL data suggests that after a rebound, along with a crater forming on the substrate, some residue from the particle can remain on the substrate surface. This can in turn inhibit further bonding of any subsequent particles that reach the surface during actual spraying. This is also seen, though not chemically, with the large impact craters on the coated specimen. The deep wells in the surface are large and circular indicating particles impacted and, instead of adhering to those already deposited, rebounded off the surface. With the slower traverse speed of a true spraying for deposition condition, the likelihood of further particles interacting with these features is higher than for the faster traverse speeds. With the collected LASHPOL data, no significant difference was found between the two different batches of AA6061 powder from Supplier A. With the spray test information, no significant difference was found in the deposition of the three AA6061 powders.

The resulting rebounds of multiple particles in the same regions would induce more of a shot peening effect and compressive stress in the coating. Also, any residue left from the rebounding particles would affect future attempts to spray a coating, whether as another layer during the same session or a future repair of the repair. This should have the net effect of reducing the deposit efficiency (less particles adhering for the same volume sprayed) and also altering the mechanical behavior of the coating due to a decrease in thickness and increase in internal compressive stress.

A longer duration study of the powder conditions alongside cold spray coating quality and performance should be carried out. The initial patterns identified in this research are constrained by a relatively small collected dataset, and further study would determine if these patterns are maintained over a longer period.

6

Conclusion

After all the research and analysis of collected data, some conclusions were reached in answer of the research questions. First, in answer to the main question: How does time elapsed between delivery and use of powder affect the quality of cold spray deposits?

The answer to this is that elapsed time affects the quality of a deposit by way of oxidation of the powder. There are potentially other micro-structural changes internal to the oxide or the particles which could affect adhesion to the substrate during spraying. The powder with the longest time elapsed between the probable production and the analysis here was the AA2024 powder, which could not be cold sprayed with the existing setup. The high crystalline oxide content measured with XRD could be the cause for this, though there were no other AA2024 powders to compare to. None of the AA6061 powders had such a high crystalline oxide content, and each was able to be sprayed throughout the research.

The two sub-questions supporting the primary query were: What is or are the cause(s) for this behavior? And, how does this affect the mechanical performance of the coating?

The causes for oxidation are exposure to oxidative environments or humidity. All of the powder samples used in this research were kept in similar containers and room temperature environments. Oxidation alone may not account for all the degradation of the powder, and possibly oxide phases becoming more or less apparent played a role. The crystalline oxide contents for the AA6061 powders remained relatively consistent and were less present than those of the AA2024 powder. However, the EDS results illustrated generally increasing trends in the overall oxygen content for each of the powders, though fluctuations and scatter between measurements made identifying a clearer conclusion difficult.

From the single particle experiments, which used the two different batches from Supplier A, there was no significant difference observed in the adhesion tendency of the particles. For these tests, the influence of different elapsed time between delivery and use of the powders was not reflected in the adhesion tendency of single particles. Also from these experiments, the possibility of oxide remnants from rebounding particles remaining on the substrate surface was observed. For a total cold spray coating, this single-particle impact behavior as a result of oxidation could result in more particles striking the surface. This could also be seen in the spray test, where the fast traverse speed produced many more impact craters than particles adhering to the substrate. The particles that fail to adhere and cause a shot-peening effect would contribute to internal compressive stress in a coating, instead of contributing to material build-up of the coating.

7

Recommendations for the Future

A more thorough understanding of the mechanisms and dynamics of the particle oxidation during storage is needed. This would involve a longer duration of testing for more sample powders in storage conditions representative of cold spray users' powder storage. This way, the trends and observations from this work can be expanded to include more information about storage or shelf life of powders, as well as tracing the evolution of the oxides over a longer period. Further, to assist with identifying what is happening on the particle surfaces, additional test methods and machinery should be used. These could include using a transmission electron microscope, Auger electron spectroscopy, or X-ray photoelectron spectroscopy, which can more easily detect lighter elements and also determine internal states of the oxides, which was not possible with SEM-EDS.

Given some of the uncertainties related to the collected Raman spectra, a further investigation into the contributions to the primary peaks for AA6061 and AA2024 should be done. This would allow the differences between the collected data to be evaluated more accurately and better inform the powder users how degradation can be assessed non-destructively. This research can also be expanded to include other alloys, though should include more than one representative batch for each alloy powder due on the difficulties in tracing the Raman behavior of the single batch of AA2024 powder in this work.

There were also uncertainties related to the LASHPOL testing, especially in the specimens where multiple particles were visible in the launch images. The cause for this, whether being a particle with satellites breaking off, or an agglomeration of several particles splitting during the launch, was not clearly identified. How to control the exact appearance and number of particles launched, especially using particles that are not perfectly spherical like in these batches, would be an important adjustment to future research.

Further, LASHPOL and similar single particle launch studies typically use perfectly spherical powders, since numerical simulations can be performed alongside experimental verification [17, 24]. In this work, the powders were not spherical, so the correlation to previously established findings in terms of critical velocity and deformation at impact could be slightly altered. Industrial users of cold spray systems that do not utilize spherical powders should be aware of how the particle shape can alter the coating mechanics.

Though only present on three receivers and only measured on two of these, the effect of using Scotch-Brite to prepare the substrate should be examined further. From the EDS analysis of the LASHPOL receivers, the prepared substrates seemed to have higher overall oxygen content compared to those not prepared with Scotch-Brite. Since there were only two receivers analyzed with this condition, this could have been a random occurrence. This phenomenon could be investigated further by testing small substrate samples prepared in different manners.

Through the single particle experiments, the possibility of rebounding particles leaving behind fractured oxides was found. Though there were only four rebound regions analyzed, and on only two of the receivers, this finding should be examined further. An examination of the many rebound sites of the fast traverse speed spray tests would also help to determine if fractured oxides remain when particles fail to adhere to a substrate.

Further, to exactly determine the effect this has on the coatings, several test specimens should be mechanically tested. This testing should be completed both for the interface region between the coating and the substrate, as well as the coating alone and its internal quality. An example of a test method and description that is related to (and was investigated for) the evaluation of the interface between the coating and substrate is included in Appendix D.

For the industry and actual users of cold spray systems, an important aspect to understand is what is going on with the powder over time and how to mitigate or correct for it. Storage conditions were not assessed in this research, though determining what containers or environments cause a faster degradation in the powder condition and thus diminish coating performance would be valuable. This could then be avoided to maintain higher levels of coating performance. Some work has been done to recover powder that has been over-exposed to oxidative environments [15, 21, 25] using de-gassing or desiccation of the powders. How this would affect a deposited coating could also be studied.

Further, the exact effect that increased tamping of the surface would have on a coating (caused by the degradation of the powder and the failure to adhere) should be investigated. This would allow users to understand, anticipate, and possibly compensate for the expected material degradation. This could be assessed by producing coatings using powders of different ages and evaluating the dimensions and properties like hardness and porosity of the coatings.

Lastly, a coating produced with degraded powder could include a higher proportion of oxides or fractured oxides between deposit layers. These inclusions could be damage initiation or nucleation sites that would likely reduce the lifetime of a cold sprayed part. The effect of embedded oxides in a loaded coating could be studied to understand if damage initiates earlier at these sites or if there was a post-treatment that could mitigate the effects on a sprayed part.

References

[1] V. Champagne Jr, O. Ozdemir, and A. Nardi, *Practical Cold Spray*. Springer, 2021.

[2] S. E. Julien, A. Nourian-Avval, W. Liang, T. Schwartz, O. C. Ozdemir, and S. Muftu, “Bulk fracture anisotropy in cold-sprayed al 6061 deposits,” *Engineering Fracture Mechanics*, vol. 263, 2022.

[3] R. Huang and H. Fukanuma, “Study of the influence of particle velocity on adhesive strength of cold spray deposits,” *Journal of Thermal Spray Technology*, vol. 21, pp. 541–549, 2012.

[4] O. D. Neikov, *Handboook of Non-ferrous Metal Powders (Second Edition) Chapter 4: Atomization and Granulation*. 2019, pp. 125–185.

[5] A. T. Ernst *et al.*, “Surface states of gas-atomized al 6061 powders – effects of heat treatment,” *Applied Surface Science*, vol. 534, 2020.

[6] P. Ren *et al.*, “Metal powder atomization preparation, modification, and reuse for additive manufacturing: A review,” *Progress in Materials Science*, vol. 152, 2025.

[7] H. Durand and F. Delloro, “A method for characterizing the quasi-static mechanical behavior of powders for the cold spray process,” *Materialia*, vol. 39, 2025.

[8] A. G. Gavras, D. A. Lados, V. K. Champagne, R. J. Warren, and D. Singh, “Small fatigue crack growth mechanisms and interfacial stability in cold-spray 6061 aluminum alloys and coatings,” *Metallurgical annd Materials Transactions A*, vol. 49, pp. 6509–6520, 2018.

[9] A. Navabi *et al.*, “Deformation and cracking phenomena in cold sprayed 6061 al alloy powders with nanoscale aluminum oxide films,” *Materials Science and Engineering: A*, vol. 841, 2022.

[10] M. Winnicki *et al.*, “Numerical and experimental analysis of copper particles velocity in low-pressure cold spraying process,” *Surface Coatings and Technology*, vol. 268, pp. 230–240, 2015.

[11] M. Martin and E. Fromm, “Low-temperature oxidation of metal surfaces,” *Journal of Alloys and Compounds*, vol. 258, no. 1-2, pp. 7–16, 1997.

[12] V. Yakubov *et al.*, “Recycled aluminium feedstock in metal additive manufacturing: A state of the art review,” *Heliyon*, vol. 10, no. 5, 2024.

[13] US Army DEVCOM Research Laboratory, Specifications & Standards Office, “MIL-DTL-32495A Detail Specification: Powders for Cold Spray Deposition,” vol. 2, 2021.

[14] US Department of Defence, “MIL-STD-3021 Materials Deposition, cold Spray,” vol. 1, no. 2, 2015.

[15] H. Na, K. Tsaknopoulos, T. Lei, B. C. Sousa, D. L. Cote, and C. A. Schuh, “Single particle impact explorations on the role of powder heat treatments in cold spray: Effects of strength and oxide structure,” *Journal of Materials Research and Technology*, vol. 36, pp. 7026–7034, 2025.

[16] D. Poirier, J.-G. Legoux, P. Vo, B. Blais, J. D. Giallonardo, and P. G. Keech, “Powder development and qualification for high-performance cold spray copper coatings on steel substrates,” *Journal of Thermal Spray Technology*, vol. 28, pp. 444–459, 2019.

[17] K. Kang, S. Yoon, Y. Ji, and C. Lee, “Oxidation dependency of critical velocity for aluminum feedstock deposition in kinetic spraying process,” *Materials Science and Engineering: A*, vol. 486, no. 1-2, pp. 300–307, 2008.

[18] ASTM International. “ASTM B822 Standard Test Method for Particle Size Distribution of Metal Powders and Related Compounds by Light Scattering.” (2020), [Online]. Available: `https://www.astm.org`.

[19] ASTM International. “ASTM B215 Standard Practices for Sampling Metal Powders.” (2025), [Online]. Available: `https://www.astm.org`.

[20] M. Mehrabi, J. Gardy, F. A. Talebi, A. Farshchi, A. Hassanpour, and A. E. Bayly, “An investigation of the effect of powder flowability on the powder spreading in additive manufacturing,” *Powder Technology*, vol. 413, 2023.

[21] J. Lienhard *et al.*, “Surface oxide and hydroxide effects on aluminum microparticle impact bonding,” *Acta Materialia*, vol. 197, pp. 28–39, 2020.

[22] I. Dowding, M. Hassani, Y. Sun, D. Veysset, K. A. Nelson, and C. A. Schuh, “Particle size effects in metallic microparticle impact-bonding,” *Acta Materialia*, vol. 194, pp. 40–48, 2020.

[23] X. Chen, A. A. Tiamiyu, C. A. Schuh, and J. M. LeBeau, “Additional hindrances to metallurgical bonding from impurities during microparticle impact,” *Surface and Coatings Technology*, vol. 433, 2022.

[24] F. Delloro *et al.*, “Characterization of mechanical behaviour of aluminum powders under fast dynamic conditions,” *EPJ Web of Conferences*, vol. 250, 2021.

[25] K. Ko, J. Choi, H. Lee, and B. Lee, “Influence of oxide chemistry of feedstock on cold sprayed cu coatings,” *Powder Technology*, vol. 218, pp. 119–123, 2012.

[26] C. Zhang *et al.*, “Critical velocity and deposition efficiency in cold spray: A reduced-order model and experimental validation,” *Journal of Manufacturing Processes*, vol. 134, pp. 547–557, 2025.

[27] H. Assadi *et al.*, “On parameter selection in cold spraying,” *Journal of Thermal Spray Technology*, vol. 20, pp. 1161–1176, 2011.

[28] M. Razavipour, S. Rahmati, A. Zuniga, D. Criado, and B. Jodoin, “Bonding mechanisms in cold spray: Influence of surface oxidation during powder storage,” *Journal of Thermal Spray technology*, vol. 30, pp. 304–323, 2021.

[29] Q. Tang, Y. Ichikawa, and M. Hassani, “Surface oxide layer strengthening and fracture during flattening of powder particles,” *Scripta Materialia*, vol. 244, 2024.

[30] K. Wefers and C. Misra, *Oxides and hydroxides of aluminum*. Alcoa Laboratories Pittsburgh, PA, 1987, vol. 19.

[31] K. Shimizu, K. Kobayashi, T. G.E., and G. Wood, “The apparent induction period for γ-al2o3 development in thermal oxide films on aluminium,” *Oxidation of Metals*, vol. 36, pp. 1–13, 1991.

[32] HORIBA Jobin Yvon. “Raman Spectroscopy for Analysis and Monitoring.” (), [Online]. Available: `https://static.horiba.com/fileadmin/Horiba/Technology/Measurement_Techniques/Molecular_Spectroscopy/Raman_Spectroscopy/Raman_Academy/Raman_Tutorial/Raman_bands.pdf?utm_source=uhw&utm_medium=301&utm_campaign=uhw-redirect`.

[33] D. Tuschel, “Stress, strain, and raman spectroscopy,” *Spectroscopy*, vol. 34, no. 9, 2019.

[34] N. Doebelin and R. Kleeberg, “Profex: A graphical user interface for the rietveld refinement program bgmn,” *Journal of Applied Crystallography*, vol. 48, no. 5, pp. 1573–1580, 2015.

[35] A. Jain *et al.*, “Commentary: The materials project: A materials genome approach to accelerating materials innovation,” *APL Materials*, vol. 1, no. 1, 2013.

[36] JEOL, *Scanning electron microscope a to z: Basic knowledge for using the sem*.

[37] D. Wieboldt, “Understanding raman spectrometer parameters,” *Spectroscopy*, 2010.

[38] K. Zhu *et al.*, “Residual stress and microstructure of the cnt/6061 composite after shot peening,” *Materials & Design*, vol. 107, pp. 333–340, 2016.

[39] Y. Chen, B. Q. Lu, and H. A. Zhang, “Hardening and precipitation of a commercial 6061 al alloy during natural and artificial ageing,” *IOP Conference Series: Material Science and Engineering*, vol. 770, 2020.

[40] S. A. Mahmoud, M. E. Elsisi, and A. F. Mansour, “Synthesis and electrochemical performance of α-al2o3 and m-al2o4 spinel nanocomposites in hybrid quantum dot-sensitized solar cells,” *Scientific Reports*, vol. 12, 2022.

[41] F. Adar, “Raman spectra of metal oxides,” *Spectroscopy*, vol. 29, no. 10, 2014.

[42] S. Boullosa-Eiras, E. Vanhaecke, T. Zhao, D. Chen, and A. Holmen, “Raman spectroscopy and x-ray diffraction study of the phase transformation of zro2–al2o3 and ceo2–al2o3 nanocomposites,” *Catalysis Today*, vol. 166, no. 1, pp. 10–17, 2011.

[43] P. Thomas, V. Ramakrishnan, and V. Vaidyan, “Oxidation studies of aluminum thin films by raman spectroscopy,” *Thin Solid Films*, vol. 170, no. 1, pp. 35–40, 1989.

[44] N. M. Stuart and K. Sohlberg, “The microstructure of γ-alumina,” *Energies*, vol. 14, 2021.

[45] M. Xie, C. Xiang, X. Zeng, X. Zhang, L. Zhang, and J. Xiong, “Optimization of the raman spectroscopic method for crystal orientation and residual stress of aluminum oxide,” *Journal of Materials Research and Technology*, vol. 33, pp. 8265–8276, 2024.

[46] Renishaw, *Invia research-grade confocal raman microscopes*. [Online]. Available: `renishaw.com/raman`.

[47] L. Kovarik, M. Bowden, D. Shi, J. Szanyi, and C. H. Peden, “Structural intergrowth in δ-al2o3,” *Journal of Physical Chemistry C*, vol. 123, no. 14, pp. 9454–9460, 2019.

[48] ASTM International. “ASTM C633 Standard Test Method for Adhesion or Cohesion Strength of Thermal Spray Coatings.” (2021), [Online]. Available: `https://www.astm.org`.

[49] B. White, W. A. Story, L. Brewer, and J. Jordon, “Fracture mechanics methods for evaluating the adhesion of cold spray deposits,” *Engineering Fracture Mechanics*, vol. 205, pp. 57–69, 2019.

[50] P. Charalambides, J. Lund, A. Evans, and R. McMeeking, “A test specimen for determining the fracture resistance of bimaterial interfaces,” *Journal of Applied Mechanics*, vol. 56, pp. 77–82, 1989.

[51] P. Charalambides, H. Cao, J. Lund, and A. Evans, “Development of a test method for measuring the mixed mode fracture resistance of bimaterial interfaces,” *Mechanics of Materials*, vol. 8, no. 4, pp. 269–283, 1990.

[52] T. Bond, B. Sousa, N. Rahbar, D. Cote, K. Tsaknopoulos, and W. Soboyejo, “Fatigue and delamination of 6061 aluminum cold spray on a similar wrought substrate,” *Materials Science and Engineering: A*, vol. 913, 2024.

A

Additional LASHPOL Launch Images

The LASHPOL launch images were examined to determine the velocity of the particles and whether they successfully adhered to the substrate. However, this was not the only thing visible in some of the experiments. The example presented here was not immediately relevant to the research, but was still an interesting outcome of the testing.

A curious result came from the launch images of specimen A16. There were multiple particles visible in the first frame which then seemed to disappear. This is shown in the launch images presented in Figure A.1.

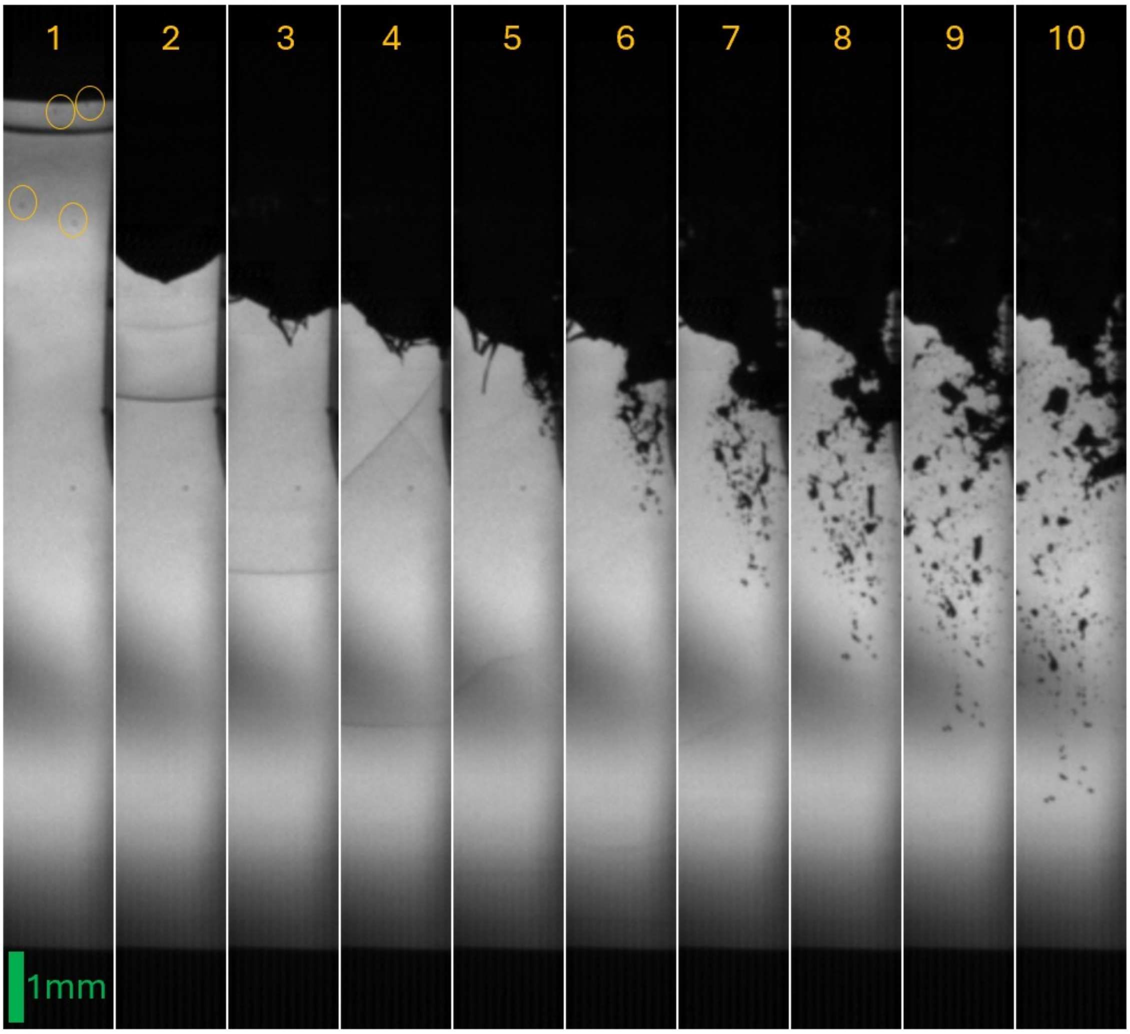

Figure A.1: Four apparent particles in the laser-shocked region of the launcher for A16 in image 1. Image 2 shows no visible particles. Shockwave shapes visible through image 7. Total distance represented in the images is 14.19 mm, and the scale of 1 mm is illustrated in green

Because the (most likely) particles did not remain visible in any frames past the first, it was possible that they were off center from the laser shock and had enough lateral velocity to leave the camera view. However, also the fact that there were four ”particles” visible in the first image was concerning, since care was taken to place single particles and clean the launcher surface around them to make velocity calculations easier. What this launch nicely showed, however, was an example of the shock wave being constrained by the guidance carriage and how the shape progressed along the flight path.

The receiver for this experiment was not kept for further analysis, so a definitive result following this launch was not determined.

B

Additional LASHPOL SEM Images

Several of the receivers were examined in the SEM at Mines Paris-PSL to determine if a splat was present. On only one of the examined receivers, A05, was there indication of a particle splat.

The appearance of the splat found on receiver A05 was very strange. There is not any significant deformation of the substrate, nor much evidence of jetted material from the particle. The SEM image of the splat on receiver A05 is shown in Figure B.1.

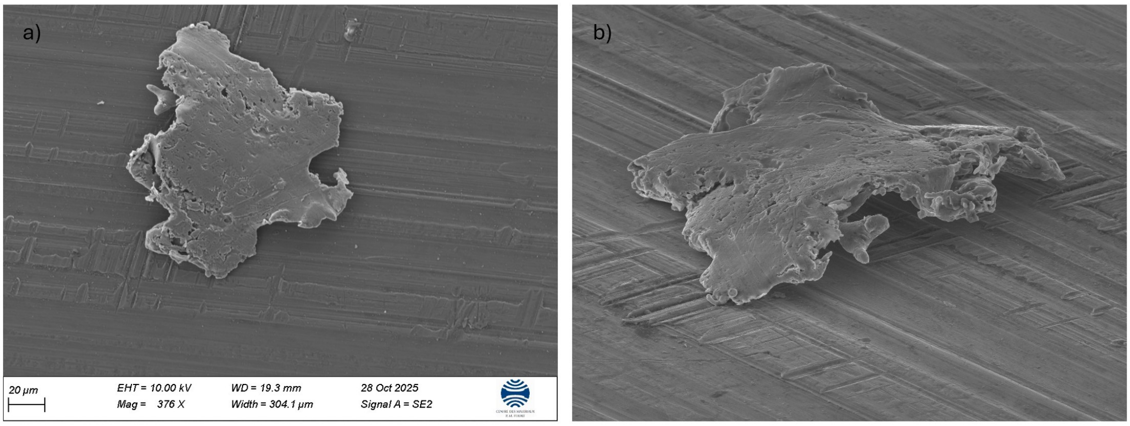

Figure B.1: SEM images of particle splat on A05 from a) top view and b) side view angled 62.5 °. Taken on a Zeiss Gemini SEM at Mines-PSL Innovation Campus

The flattening on the top of the particle could not be readily explained, even by those familiar with LASHPOL experimentation who were present for this observation. The splat was identified as aluminum by EDS, so it was not a piece of debris from the launcher.

This receiver was examined again at DASML, and while the apparent splat was found in the optical microscope, the location could not be found when the receiver was examined in the Jeol SEM.

C

Additional Spray Test Surface Mapping Images

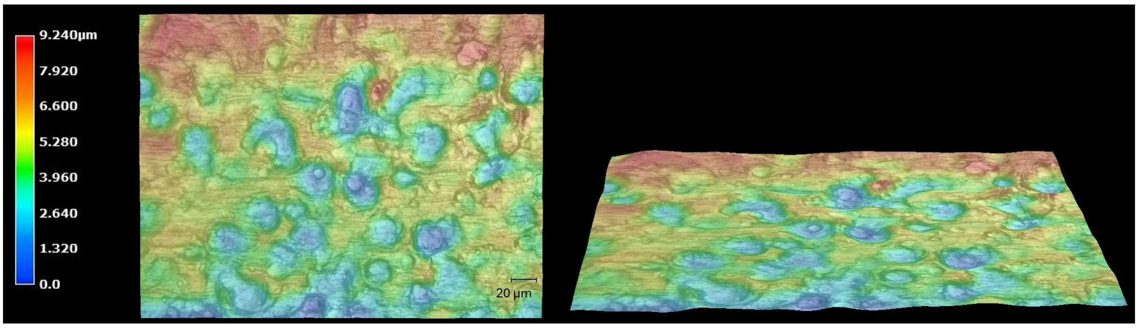

Figure C.1: Surface mapping of the first spray path with fast traverse speed using the New batch of Al6061 from Supplier A

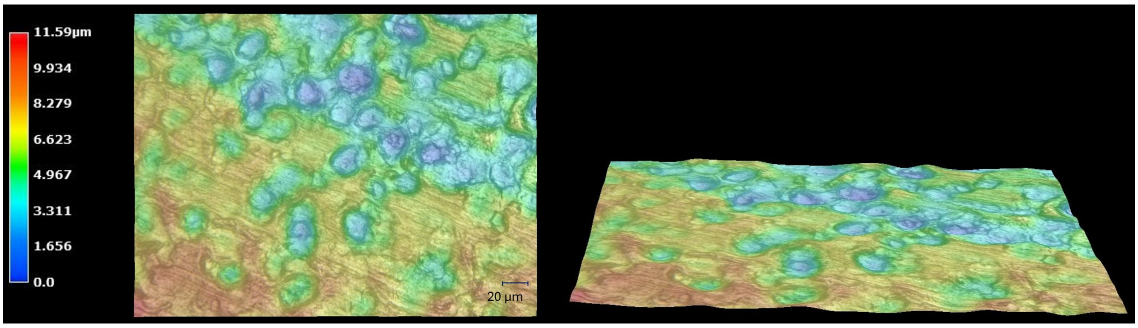

Figure C.2: Surface mapping of the first spray path with fast traverse speed using the Old batch of Al6061 from Supplier A

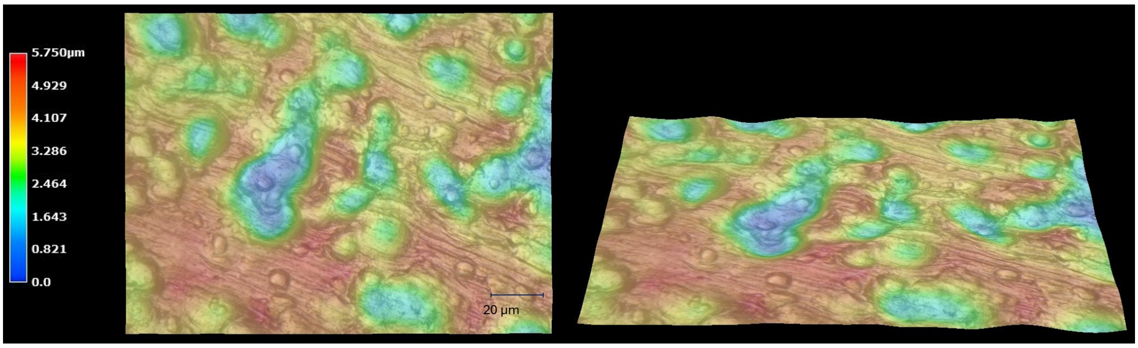

Figure C.3: Surface mapping of the first spray path with fast traverse speed using the Al6061 from Supplier B

D

Charalambides' bi-material interface

The following is a section originally intended for the literature review section, but due to limitations in the spraying capability during the thesis, had to be removed from the scope of the research. It is included here for reference and extension of the research for the future.

Many studies use the deposition efficiency as a marker of the spray quality [17, 25, 26]. While this is indicative of the amount of powder deposited on the substrate, it cannot indicate the integrity of the coating or the interfacial connection with the substrate. Oxidation between particles that remains unbroken can form kissing bonds, where the connection between the two parts is not secure but appears to be [12]. This was observed in friction stir additive manufacturing, not cold spray deposition.

A typical assessment of the deposit quality is an adhesion test following the procedure of ASTM C633 [48], where an epoxy adhesive is used to affix a pull bar on the top surface of the deposit. Though designed for thermal spray coatings, many agree that cold spray coatings can be assessed similarly [1, 14]. The substrate and the pull bar are connected to a test bench and subjected to tension to attempt to pull the coating away from the substrate. Failures can occur at the coating-substrate interface (adhesive), within the coating (cohesive), or in the epoxy [48]. This method is limited by the strength of the adhesive, and indicates whether the deposit has a cohesive or interfacial strength greater or less than the adhesive. The coatings that experience failure in the epoxy may have strengths at varying levels above this level, which is not able to be assessed in this way. For example one specimen may actually have a strength only 1% better than the adhesive, but would be seen performing as well as one that could have strength of 50% better than the adhesive.

Because the deposit forms a coating over the substrate, and solid bonding is formed when the impacting particles significantly deform as well as penetrate into the surface of the substrate, the resulting interface should be distinct but tortuous in profile. Even when spraying the same alloy powder as the substrate material, the interface separates the resulting part in two. As mentioned previously, the properties of the powder can vary from that of the bulk material even with the same composition, primarily because of the gas atomization process. Also, altering the spray settings has a considerable effect due to the potential for larger particle deformations. Thus, the interface between the coating and substrate can be considered a bi-material interface, even with the two materials being inherently similar [49].

This coating can be tested in bending to artificially open up and separate the coating from the substrate. Then, the interfacial strength can be quantified and compared for various conditions of powder or different spray settings. A test method and specimen was designed to evaluate the interface between a substrate and a coating by Charalambides et al [50] [51].

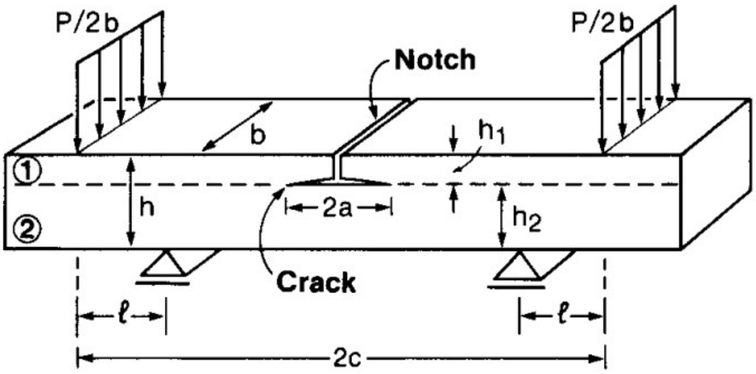

Figure D.1: Bi-material notched four point bending specimen, rom Charalambides et al [50]

This has been used to evaluate the interfacial strength for cold sprayed coatings in four point bending [49] [52].

The strain release rate in steady state for such a situation and specimen is expressed as:

$$G_{ss} = \frac{M^2(1-\nu_2^2)}{2E_2}\Big(\frac{1}{I_2} - \frac{\lambda}{I_c}\Big) \tag{D.1}$$

With the moment per unit width of the specimen $M = \frac{Pl}{2b}$ where P is the total load and l is the spacing between inner and outer load lines caused by the support and loading rollers as shown in Figure D.1. The difference in the two materials is expressed by the factor:

$$\lambda = \frac{E_2(1-\nu_1^2)}{E_1(1-\nu_2^2)} \tag{D.2}$$

Where the modulus of elasticity E and Poisson ratio ν of both the substrate and the coating have an effect.

As for the dimensions, while the width and length of both material sections are the same, the thickness could be different. The contribution of the thicknesses and potential material behavior differences of the substrate (material 2) and the coating (material 1) is included in the second moment of areas per unit width of the substrate beam:

$$I_2 = \frac{h_2^3}{12} \tag{D.3}$$

and that of the composite beam including both materials:

$$I_c = \frac{h_1^3}{12} + \frac{\lambda h_2^3}{12} + \frac{\lambda h_1 h_2 (h_1 + h_2)^2}{4(h_1 + \lambda h_2)} \tag{D.4}$$

With four point bending, the interface is experiencing a combination of mode 1 and mode 2 loadings, and the proportion depends mainly on the thickness or Young's modulus of the two components [49] [50]. With spraying 6061 powder on 6061 substrates, both coating and substrate are expected to have very similar values of elastic modulus [8], and in fact they have been taken as identical by some researchers [49]. In combination with the Poisson ratio assumed to be 0.3 for both components, the quantity λ becomes 1.

E

Laser safety

Operation of the LASHPOL setup was not my role, but I was in the room for every test (and reading the temperature of the substrate during heated experiments), and so I wore the safety glasses to prevent eye damage during the experiments. Enjoy this unflattering photo of me wearing them on day 1 of the experiments, taken by Patrizio.

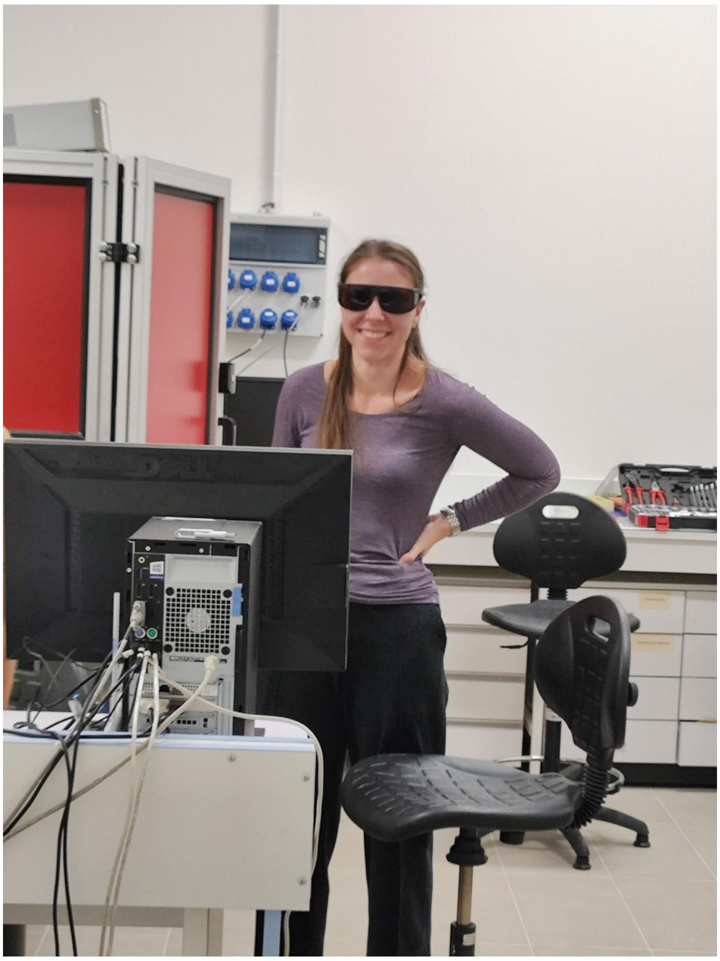

Figure E.1: A.M. Brandt wearing the protective eyewear for LASHPOL operation. Photo credit P. Lomonaco